



City Research Online

City, University of London Institutional Repository

Citation: Ryan, E. (2006). The characterisation of five classifications of breast tissue using x-ray scattering properties. (Unpublished Doctoral thesis, City, University of London)

This is the accepted version of the paper.

This version of the publication may differ from the final published version.

Permanent repository link: <https://openaccess.city.ac.uk/id/eprint/30811/>

Link to published version:

Copyright: City Research Online aims to make research outputs of City, University of London available to a wider audience. Copyright and Moral Rights remain with the author(s) and/or copyright holders. URLs from City Research Online may be freely distributed and linked to.

Reuse: Copies of full items can be used for personal research or study, educational, or not-for-profit purposes without prior permission or charge. Provided that the authors, title and full bibliographic details are credited, a hyperlink and/or URL is given for the original metadata page and the content is not changed in any way.

**The characterisation of five classifications
of breast tissue using x-ray scattering
properties**

Elaine Ryan

**Submitted in fulfilment of the requirements for the award of the
Degree of Doctor of Philosophy**

**Department of Radiography
Institute of Health Sciences
City University**

May 2006

| | |
|-------------------------------|-------------|
| List of Figures | iv |
| List of Tables | vii |
| Acknowledgements | viii |
| Abstract | 1 |

| | |
|-----------------------------------|----------|
| Chapter 1 Background | 2 |
|-----------------------------------|----------|

| | |
|--|----|
| 1.1 Introduction | 2 |
| 1.2 The Breast | 5 |
| 1.2.1 The anatomy of the breast | 5 |
| 1.2.2 Breast cancer pathology | 6 |
| 1.2.3 Current diagnosis techniques | 8 |
| 1.2.4 Current treatment for breast disease | 13 |
| 1.3 X-ray interactions with tissue..... | 14 |
| 1.3.1 Introduction..... | 14 |
| 1.3.2 Attenuation..... | 15 |
| 1.3.3 Photoelectric absorption..... | 16 |
| 1.3.4 Compton Scatter..... | 20 |
| 1.3.5 Coherent scattering..... | 26 |
| 1.4 Literature review | 28 |

| | |
|---|-----------|
| Chapter 2 Experiment preparation | 37 |
|---|-----------|

| | |
|--|----|
| 2.1 Introduction | 37 |
| 2.2 Laboratory experimental set-up | 38 |
| 2.2.1 Equipment | 38 |
| 2.2.2 Collimator alignment | 40 |
| 2.2.3 Detector energy resolution | 42 |
| 2.2.4 Single Channel Analyser (SCA) energy calibration | 43 |
| 2.2.5 Multi Channel Analyser (MCA) energy calibration..... | 44 |
| 2.2.6 Visual basic program..... | 44 |
| 2.3 Synchrotron experimental set-up | 45 |
| 2.3.1 Daresbury synchrotron | 45 |
| 2.3.2 ESRF Synchrotron | 45 |
| 2.4 Sample preparation..... | 48 |
| 2.4.1 Tissue storage and preparation..... | 48 |
| 2.4.2 Sample holders | 48 |
| 2.5 Summary | 51 |

| | |
|--|----------------|
| Chapter 3 Electron density measurement..... | 52 |
| 3.1 Introduction..... | 52 |
| 3.2 Theory..... | 53 |
| 3.3 Method..... | 59 |
| 3.3.1 Laboratory measurements..... | 59 |
| 3.3.2 Synchrotron measurements..... | 64 |
| 3.4 System calibration..... | 68 |
| 3.5 Summary..... | 72 |
| Chapter 4 Electron density measurement results and analysis | 73 |
| 4.1 Introduction..... | 73 |
| 4.2 Laboratory measurements..... | 73 |
| 4.2.1 Final results..... | 73 |
| 4.2.2 Errors..... | 78 |
| 4.2.3 Statistical Analysis..... | 80 |
| 4.2.4 Comparison to ICRU Report 46 data..... | 82 |
| 4.2.5 Discussion..... | 83 |
| 4.3 Synchrotron measurements..... | 85 |
| 4.3.1 Final results..... | 85 |
| 4.3.2 Errors..... | 88 |
| 4.3.3 Statistical Analysis..... | 88 |
| 4.4 Comparison of measurement systems..... | 89 |
| 4.5 Summary..... | 91 |
| Chapter 5 Scatter Profile Measurement..... | 92 |
| 5.1 Introduction..... | 92 |
| 5.2 Theory..... | 93 |
| 5.3 Experimental and data correction methods..... | 96 |
| 5.3.1 Introduction..... | 96 |
| 5.3.2 Angular Dispersive X-Ray Diffraction (ADXRD) measurements..... | 97 |
| 5.3.3 Energy Dispersive X-Ray Diffraction (EDXRD) Measurements..... | 104 |
| 5.3.4 Normalisation and Compton background subtraction..... | 106 |
| 5.4 Summary..... | 113 |
| Chapter 6 Scatter profile measurement results and analysis..... | 114 |
| 6.1 Introduction..... | 114 |
| 6.2 Scatter profile measurement results..... | 115 |
| 6.3. Analysis..... | 119 |
| 6.3.1 Introduction..... | 119 |
| 6.3.2 Deconvolution of spectra..... | 120 |
| 6.3.3 Statistical analysis..... | 121 |
| 6.3.4 Analysis of ESRF results..... | 123 |
| 6.4 Discussion..... | 124 |
| 6.5 Summary..... | 126 |

| | |
|--|------------|
| Chapter 7 Multivariate data analysis combining electron density and scatter profile results | 127 |
| 7.1 Introduction | 127 |
| 7.2 Background | 128 |
| 7.2.1 Principal component analysis (PCA) | 128 |
| 7.2.2 Soft Independent Modelling of Class Analogies (SIMCA) | 130 |
| 7.3 Method | 131 |
| 7.4 Results and analysis | 133 |
| 7.4.1 Principal component analysis | 133 |
| 7.4.2 Validation | 136 |
| 7.4.3 Soft Modelling | 137 |
| 7.5 Summary | 148 |
| Chapter 8 Conclusions and further work | 149 |
| 8.1 Introduction | 149 |
| 8.2 Electron density measurements | 149 |
| 8.3 Scatter profile measurements | 151 |
| 8.4 Multivariate analysis | 151 |
| 8.5 Further work | 152 |
| 8.6 Summary | 155 |
| Appendix 1 Visual Basic program | 156 |
| Appendix 2 Sample composition tables | 158 |
| Appendix 3 Publications | 163 |
| References..... | 164 |

List of Figures

Chapter 1

| | |
|--|----|
| Figure 1.1 The anatomy of the breast..... | 5 |
| Figure 1.2a An illustration of the features of benign tissue growth..... | 7 |
| Figure 1.2b An illustration of the features of malignant tissue growth | 7 |
| Figure 1.3 A simplified patient management flow diagram for breast disease diagnosis | 9 |
| Figure 1.4 Typical cell appearances in histological examination slides | 12 |
| Figure 1.5 A diagram illustrating the dependence of interaction cross sections on energy and atomic number Z | 13 |
| Figure 1.6 Linear attenuation of a photon beam | 15 |
| Figure 1.7 Characteristic x-ray emission via the photoelectric effect..... | 17 |
| Figure 1.8 Photoelectric interaction cross section versus incident photon energy for lead | 19 |
| Figure 1.9. The energetics of Compton scattering | 20 |
| Figure 1.10 The Compton scattering cross section for various incident energies | 22 |
| Figure 1.11 A graph showing the ratio of the bound-electron Compton scattering cross section to the free electron Compton scattering cross section. | 24 |
| Figure 1.12 Diffraction Enhanced Imaging typical experimental set-up..... | 35 |

Chapter 2

| | |
|---|----|
| Figure 2.1 The equipment set-up used at City University Radiation Laboratory | 38 |
| Figure 2.2a The axes of rotation of the experimental system. The detector is at zero degrees..... | 39 |
| Figure 2.2b The system with the detector at thirty degrees | 39 |
| Figure 2.3 The electronics used in the laboratory experiments | 40 |
| Figure 2.4 An output map of the x-ray tube..... | 41 |
| Figure 2.5 The FWHM of the 59.54 keV peak of Am-241 for both detectors used in the laboratory | 42 |
| Figure 2.6 Energy calibration graph..... | 43 |
| Figure 2.7Americium-241 spectrum used to calibrate the Multi Channel Analyser... | 43 |
| Figure 2.8 The flux of the BM28 as a function of monochromatic beam energy..... | 46 |
| Figure 2.9 The electronics chain used at the ESRF | 47 |
| Figure 2.10 Slide sample holder used at the Daresbury SRS synchrotron..... | 49 |
| Figure 2.11 Sample holder for the second set of experiments | 50 |

Chapter 3

| | |
|--|----|
| Figure 3.1 A graph plotting $S(Z)$ values | 55 |
| Figure 3.2 Cylindrical geometry of the sample holder | 57 |
| Figure 3.3 Experimental set-up for scatter measurements | 60 |
| Figure 3.4 Single Channel Analyser windowed area..... | 58 |
| Figure 3.5 The transmission measurement set-up..... | 62 |
| Figure 3.6 The windowed areas chosen for the transmission measurements | 63 |
| Figure 3.7 A synchrotron scatter spectrum | 65 |

| | |
|--|----|
| Figure 3.8 A graph of the number of counts incident on the sample against time after refill | 66 |
| Figure 3.9a Incoherent scattering coefficient against number of counts in the scatter peak for laboratory measurements | 69 |
| Figure 3.9b Incoherent scattering coefficient against number of counts in the scatter peak for ESRF measurements | 69 |
| Figure 3.10a Electron density against Incoherent scattering coefficient for laboratory measurements | 70 |
| Figure 3.10b Electron density against Incoherent scattering coefficient for ESRF measurements | 70 |

Chapter 4

| | |
|--|-----|
| Figure 4.1 A box and whisker plot for the laboratory electron density data..... | 70 |
| Figure 4.2 Histogram of adipose electron density results | 76 |
| Figure 4.3 Histogram of malignant tissue electron density results | 76 |
| Figure 4.4 Histogram of benign electron density results | 77 |
| Figure 4.5 Histogram of FCC electron density results..... | 77 |
| Figure 4.6 Histogram of normal tissue electron density results..... | 77 |
| Figure 4.7 A graph comparing the values for the experimental data and the published values from ICRU Report 46 (1992)..... | 83 |
| Figure 4.8 A box and whisker plot for the ESRF electron density data..... | 865 |
| Figure 4.9 Histogram of adipose tissue electron density results..... | 86 |
| Figure 4.10 Histogram of malignant tissue electron density results | 86 |
| Figure 4.11 Histogram of benign tissue electron density results | 87 |
| Figure 4.12 Histogram of FCC tissue electron density results..... | 87 |
| Figure 4.13 Histogram of normal tissue electron density results..... | 87 |
| Figure 4.14 Box plot comparing the Laboratory and synchrotron measurements..... | 90 |
| Figure 4.15 Histogram of the synchrotron measurements as a percentage difference from the laboratory measurements for individual samples | 91 |

Chapter 5

| | |
|---|------|
| Figure 5.1 The experimental set-up used at Daresbury SRS | 97 |
| Figure 5.2 A scatter profile of mylar film | 98 |
| Figure 5.3 Illustration of the attenuation correction..... | 99 |
| Figure 5.4 The scattering volume within the tissue | 101 |
| Figure 5.5 The scattering volume at small angles..... | 101 |
| Figure 5.6 The experimental set-up used at ESRF..... | 103 |
| Figure 5.7 The experimental set-up for the Energy Dispersive measurements | 104 |
| Figure 5.8 The relative output of the x-ray tube measured at 70kV _p | 106 |
| Figure 5.9 The percentage composition of adipose tissues as a function of electron density | 108 |
| Figure 5.10 The percentage composition of glandular tissues as a function of electron density | 1085 |
| Figure 5.11 Illustration of the peak fitting model used..... | 110 |
| Figure 5.12 A graph of normalised scatter profiles..... | 112 |

Chapter 6

| | |
|--|-----|
| Figure 6.1 Scatter profiles from Daresbury SRS | 115 |
| Figure 6.2 The scatter profiles obtained in the laboratory during the first run of experiments | 115 |
| Figure 6.3 Scatter profile obtained in the laboratory during the second run of experiments | 116 |
| Figure 6.4 Scatter profiles obtained at the ESRF | 116 |
| Figure 6.5 A comparison of adipose tissue spectra | 117 |
| Figure 6.6 A comparison of benign tissue spectra | 118 |
| Figure 6.7 A comparison of malignant tissue spectra | 118 |
| Figure 6.8 The average deconvolved peaks of the scatter profiles | 120 |
| Figure 6.9 The deconvolved peaks from the ESRF spectra | 123 |
| Figure 6.10 A comparison of the results to previous studies for adipose tissue | 125 |
| Figure 6.11 A comparison of the results to previous studies for fibrous tissue | 125 |

Chapter 7

| | |
|---|------|
| Figure 7.1 The first two Principal Components of a set of data | 129 |
| Figure 7.2 An illustration of a set of axes in a SIMCA model with two PCAs as classes | 131 |
| Figure 7.3a The scores plot obtained after performing a PCA | 134 |
| Figure 7.3b The loadings obtained after performing a PCA | 134 |
| Figure 7.4 The influence plot for the adipose samples | 1345 |
| Figure 7.5 The explained variance plot for the adipose samples | 1346 |
| Figure 7.6a A Coomans plot to show the normal tissue compared with the FCC tissue for the worst model. | 137 |
| Figure 7.6b A Coomans plot to show the normal tissue compared with the FCC tissue for the best model. | 138 |
| Figure 7.7a A plot with a significance level of 5% | 139 |
| Figure 7.7b A plot with a significance level of 25% | 139 |
| Figure 7.8a A S_i/S_0 vs H_i for the worst model | 140 |
| Figure 7.8b A S_i/S_0 vs H_i for the best model | 141 |
| Figure 7.9a A model distance plot for the worst model | 141 |
| Figure 7.9b A model distance plot for the best model | 142 |
| Figure 7.10a A discrimination power plot for the worst model | 142 |
| Figure 7.10b A discrimination power plot for the best model | 143 |
| Figure 7.11a A modelling power plot for the worst model | 144 |
| Figure 7.11b A modelling power plot for the best model | 144 |
| Figure 7.12 The results for each classification model when analysed using a test set of samples | 148 |

Chapter 8

| | |
|--|-----|
| Figure 8.1 The new measurement system at City University | 129 |
|--|-----|

Appendices

| | |
|--|-----|
| Figure A.1 The terminal for control of the electronics | 156 |
| Figure A.2 A flow chart of the measurement program | 157 |

List of Tables

Chapter 3

| | |
|---|----|
| Table 3.1 The experimental parameters used for the electron density measurements. | 53 |
| Table 3.2 M/ρ values for the calibration solutions..... | 56 |

Chapter 4

| | |
|--|----|
| Table 4.1 The statistical parameters for the electron density results obtained in the laboratory | 75 |
| Table 4.2 Dunn's multiple comparison for the laboratory electron density results | 81 |
| Table 4.3 The elemental compositions (percentage by mass) of adult tissues..... | 82 |
| Table 4.4 The statistical results for the ESRF measurements of electron density | 86 |

Chapter 6

| | |
|---|-----|
| Table 6.1 Parameters of the 5 peaks in the fitting model..... | 121 |
| Table 6.2 Peak analysis results..... | 122 |
| Table 6.3 The results from the ESRF spectra peak fitting analysis | 124 |

Chapter 7

| | |
|---|-----|
| Table 7.1 Evaluation of each model..... | 146 |
|---|-----|

Acknowledgements

I would like to thank the following for all their assistance and support during this project

My supervisor Mic Farquharson, who has made my time at City University a very enjoyable experience. I greatly appreciate all the advice, support, enthusiasm, ideas and inspiration.

My friends in the laboratory, Allan Allday, Marios Yiannakas, Samuel Opoku, Eric Ofori, Richard Sanders, Christie Theodoraku and especially Tina Geraki.

All of the staff of the radiography department, especially Jennifer Edie for her support, Dave Flinton for his help with the statistical analysis and Gay Canning for her kindness.

Matthew Gaved and Chris Poulton of Tissuomics for their invaluable support and for their effort invested in the project as a whole.

The staff at the European Synchrotron Radiation Facility and at the Daresbury Synchrotron Radiation Source.

Russell Irwin for his help with endless computing problems and also for all the optimism and inspiration.

All my friends and family, especially my mum, dad and brother, for the patience, encouragement and belief.

I grant powers of discretion to the University Librarian to allow this thesis to be copied in whole or in part without further reference to me. This permission covers only single copies made for study purposes, subject to normal conditions of acknowledgement.

Abstract

This project utilised two radiation scatter interactions in order to characterise breast tissue. These two interactions were Compton scatter, used to measure the electron density of the tissues, and coherent scatter, with the analysis of coherent scatter diffraction patterns. Measurements of these parameters were made both in a laboratory and at a synchrotron source. The tissue samples investigated comprise of five different tissue classifications: adipose, malignancy, fibroadenoma, normal fibrous tissue and fibrocystic change (FCC).

This first part of this study describes a technique for measuring the electron density of breast tissue using Compton scattered photons. In the laboratory, the $K_{\alpha 2}$ line from a tungsten target industrial x-ray tube (57.97 keV) was used and the scattered x-rays collected at an angle of 30° . At this angle the Compton and coherent photon peaks can be resolved using an energy dispersive detector and a peak fitting software program. Measurements made at the European Synchrotron Radiation Facility were performed at 13keV with the detector at 112° . The system was calibrated using solutions of known electron density. The results obtained have shown that there is a difference between adipose and malignant tissue, to a value of 7.3%, and between adipose and FCC, to a value of 10.7%. These figures are found to be significant by statistical analysis. The differences between adipose and fibroadenoma tissues (0.5%) and between malignancy and FCC (3.2%) are not significant.

The second part of this study measures the coherent scatter profiles of each tissue type, using an energy dispersive method in the laboratory and an angular dispersive method at two synchrotrons. A novel normalisation technique was developed, which uses the electron density values for each sample that were measured during the first part of this study. The results of these measurements were analysed using a method of fitting peaks to the scatter profiles. The peaks obtained for each tissue type were compared using a Kruskal-Wallis analysis of variance test. Adipose and FCC tissues were easily differentiated from the other tissues. No substantial differences were found between the normal fibrous, malignant and fibroadenoma tissues, which are all fibrous tissue types.

Finally a technique of multivariate analysis was used to combine the scatter profile spectra and the electron density values into a tissue classification model. The number of parameters used in the model was refined, by grading the success of each subsequent model. The best model that was formulated was able to classify seven out of ten test samples correctly. This technique was efficient at detecting differences in the coherent scatter spectra that were not evident when the individual peaks were compared separately.

A description of the new measurement system that has been installed at City University in order to continue this work has been included, with reference to how this study aided the final experimental design.

Chapter 1 Background

1.1 Introduction

This project examines the possibility of improving current histopathological techniques used within breast cancer management by utilising the fundamental interactions between x-rays and tissue. ‘Normal’ fibrous tissue, fibrocystic change, benign, malignant and adipose *ex-vivo* breast tissue samples were interrogated using Compton and coherent scattering. The properties under examination were the electron density, which is proportional to the number of Compton scattered photons and is dependent on the tissue composition, and the coherent scatter diffraction pattern of the tissue, which is dependent on the tissue structure. If finding an accurate and reliable difference between the properties of these five broad tissue types is proven to be successful the aim is to extend this study to include more refined tissue classifications.

X-rays offer a means of probing the tissue structure and content through various reaction mechanisms that take place when photons interact with matter. There is evidence that sufficient differences between benign and malignant tissues exist to make distinguishing them using x-ray analysis a viable task. It has been shown that these two tissue types show a difference in secondary protein structure and blood vessel concentration (Ellis 1999). The concentration and arrangement of calcifications have also been the subject of clinical research, which indicates that these two parameters change with breast pathology (Galkin *et al.* 1977). The cellularity and cell-to-cell cohesion of these two tissue types are known to differ significantly; benign cell populations consist of a uniform cell type, whereas malignant lesions contain a mixture of cell types usually epithelial, myoepithelial and fragments of stroma cells (Trott 1996). There are also nuclear characteristics, like nucleus size and membrane composition, which are known to be different, as these are some of the patterns that a histopathologist will look at when examining tissue samples (Zakhour and Wells 1999).

The proposed application of these measurements is to develop a bench-top technology that will allow fast and reliable *ex-vivo* tissue sample interrogation. The availability of virtually instantaneous information on tissue classification may assist surgeons when

defining the margins of tumours during surgery, by identifying whether excised tissue contains malignancy. This may be particularly helpful when removing large or infiltrating growths, where decisions on the extent of microscopic spread or requirement for more radical surgery have to be made during the operation. Currently if tissue classification is needed during surgery a frozen section is undertaken. This is a time consuming and unreliable procedure requiring facilities that are not always readily available. The ability to be able to access fast and reliable information about tissue during operations may increase the amount of breast conservation procedures that are performed, especially in areas where access to adequate support facilities is limited and mastectomies are the standard procedure for breast cancer cure.

This technology may also enable clinicians to verify that they have successfully obtained target tissue when undertaking biopsies, before sending samples for histological analysis. This could reduce the number of samples that are needed for diagnosis, as well as cut down the number of patients who are recalled for repeat biopsies because an incorrect area of tissue was sampled.

The overall aim of this study was to determine whether tissue can be discriminated using x-ray scattering properties. In order to achieve this, the following objectives had to be met:

- Design and build a measurement system, with the capability of measuring the Compton and coherent scattered radiation.
- Optimise the measurement system to produce accurate results with small experimental errors.
- Devise a suitable method of calibration for electron density quantification.
- Prepare the biological samples for measurement.
- Analyse data using methods that will identify any differences in the tissue sample types.
- Find an appropriate statistical analysis technique to validate the findings of the study.

Chapter 1 Introduction

Chapter 1 will cover the background of the study, including the mechanisms of breast cancer and the current techniques used to examine biopsy samples. This chapter also describes the fundamental interactions between x-rays and matter. These interaction processes form the basis of the experimental work performed. Relevant work performed by other groups is outlined. Chapter 2 explains the experimental set-up and equipment used during all of the practical work. Chapter 3 presents the method used for determining the electron density of tissues, both in the laboratory and at a synchrotron. Chapter 4 is the results from the electron density measurements. These results are then compared to the values published by the International Commission on Radiation Units (ICRU 1992). Chapter 5 outlines the methods used to examine the scattering profiles of breast tissue samples. The experiments were carried out using two methodologies, both of which are described. Chapter 6 presents the results obtained using the two different methods. These are then compared. Chapter 7 presents a method of examining the results using a multivariate modelling technique. Finally Chapter 8 ties together the conclusions from the experimental results. This chapter also looks to the future and outlines the work which will be carried out as a continuation of the study.

1.2 The Breast

1.2.1 The anatomy of the breast

The breast is made up of adipose and fibrous glandular tissue. The adipose tissue surrounds and supports the parenchyma, which is composed of the glandular tissue components, the lymphatic network, blood vessels and connective stroma. Each breast has 10 to 20 lobes, each containing hundreds of lobules where milk is produced during lactation. The lobules are joined to the nipple by the milk ducts, which are lined with epithelial cells.

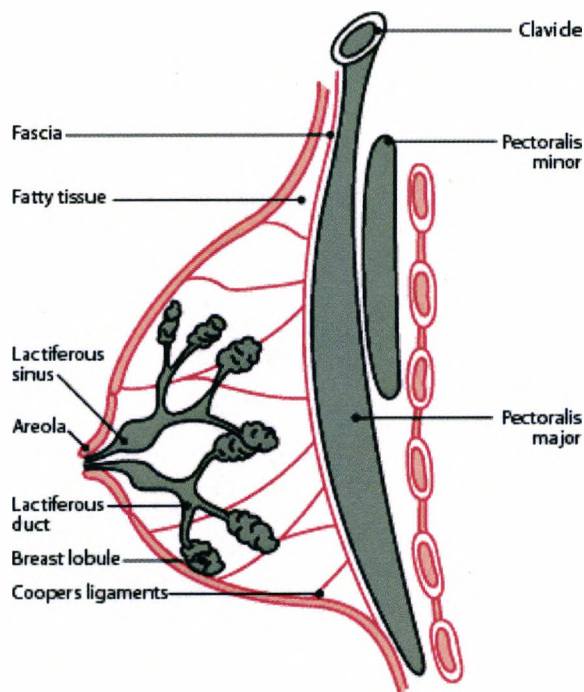


Figure 1.1 The anatomy of the breast

(AstraZenica Oncology 2006)

Each breast is enveloped between two layers of fibrous tissue. A thick layer lies underneath the adipose tissue on top of the chest wall and a thin layer lies underneath the skin outside the adipose tissue. Ligaments of fibrous tissue, called Cooper's ligaments, hold these two layers together and support the breast. These consist of stroma, a dense collagenous tissue. Figure 1.1 shows an illustration of the anatomy of the breast.

There is a network of lymph glands around the breasts which carry drainage fluid from the breast to the lymphatic system. Breakaway cancer cells can be carried by this system to other parts of the body, which may then lead to the growth of secondary tumours. The breast ductal structures are fully formed by the time a woman is 17 years old but throughout life the breasts are constantly changing, mainly due to the menstrual cycle. Hormonal fluctuations over time cause normal physiological changes to occur within the breast. Oestrogen and progesterone are the main hormones that influence the breasts. Over or under production of these hormones is responsible for most abnormal changes. Oestrogen is thought to be one cause of epithelial proliferation and ductal enlargement.

During and after the menopause supportive tissue turns to fat. The 25-39 year old age group has an average breast composition of 38% fat, whereas the 75-79 year age group has 76% fat (Stomper *et al.* 1996) with over 45s having twice as much fat content in the breast as those under 45. Smaller ducts may also disappear. Hormone replacement therapy may reverse this, causing an increase in glandular tissue, and hence an increase in the density of the breast.

1.2.2 Breast cancer pathology

A tumour forms when a cell develops a faulty growth control gene. This causes the cell to divide uncontrollably and to form an intrusive mass. There are a number of factors that can cause this proliferation to begin, some of these being diet, exposure to external carcinogens such as radiation or cigarette smoke, and genetic factors. These causes have all been found from epidemiological studies, however it not known exactly why an individual patient will develop a cancerous cell growth.

Within the breast different types of lesion occur, depending on the location and behaviour of the tumour. Tumours are divided into two important categories, benign and malignant. A benign tumour grows slowly and is completely contained within the host tissue. A benign tumour can appear and sometimes disappear without causing any significant risk or discomfort to the patient. The only risk it may present is if it lies near to a critical structure, which may be compressed by the benign growth. A malignant tumour extends into the surrounding tissue, eventually destroying these tissue cells. A malignancy may also form secondary tumours (metastases) in other

parts of the body. It causes such damage to the surrounding tissues that without treatment it will almost certainly result in the death of the patient. Therefore the need to quickly and accurately differentiate between these two tissue types is clear. The phrase 'benign breast disease' has no clear clinical or pathological definition and is used in an ambiguous manner. Figures 1.2a and b illustrate the general differences between benign and malignant lesions.

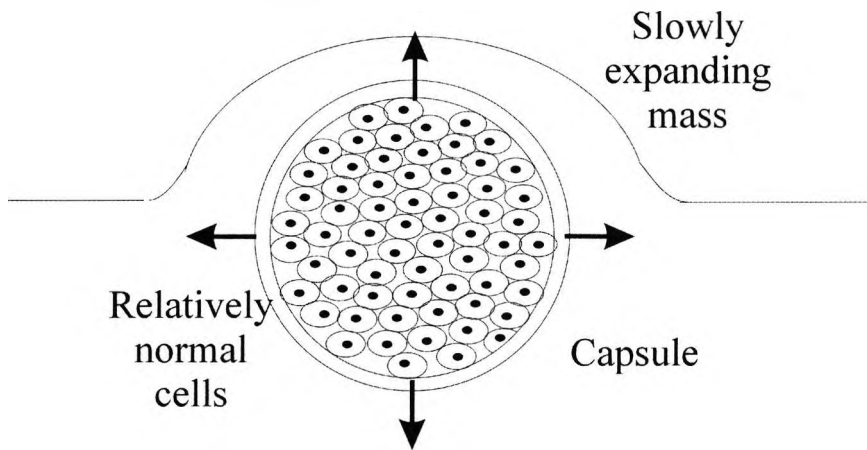


Figure 1.2a An illustration of the features of benign tissue growth

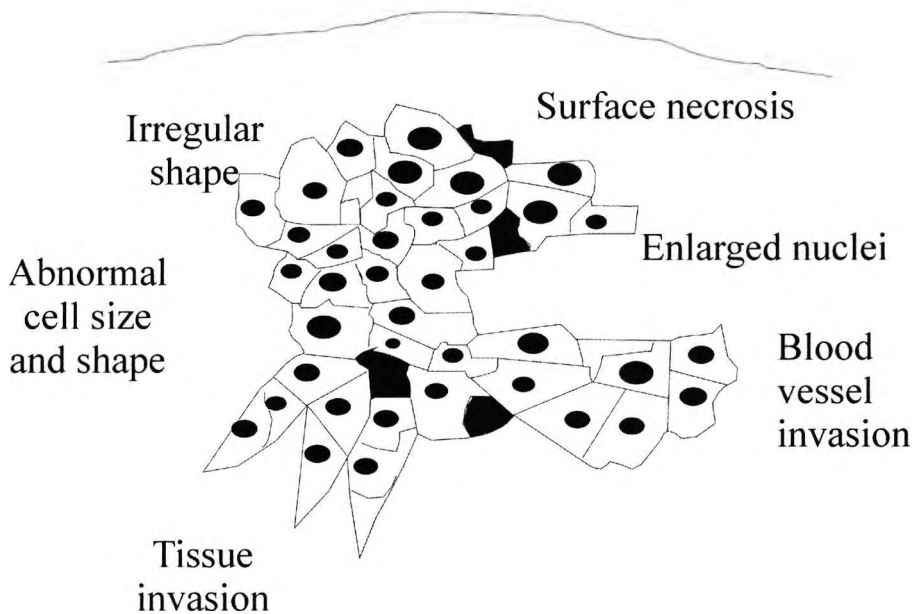


Figure 1.2b An illustration of the features of malignant tissue growth

The most common cancers arise from epithelial cells within glandular tissue. These are carcinomas, with the most widespread of these conditions arising in the cells lining the milk ducts called ductal carcinomas. Lobular carcinomas arise from cells in the lobes of the breast gland tissue. A carcinoma can be classed as invasive, where it

has spread into surrounding tissue, or in-situ, where it is still contained entirely within the host tissue.

Breast cancer is currently described using a multi-step disease model, with a sequence of disease states (Lakhani 2003). Epithelial hyperplasia is thought to transform into atypical hyperplasia, which in turn becomes carcinoma in-situ and finally invasive carcinoma. Screening has led to an increase in the number of early or pre-invasive (in situ) tumours that are detected.

Benign growths are far more proliferate than malignancies and there are many different types. Those that grow within glandular tissue are called adenomas and those in fibrous tissue are called fibromas. A fibroadenoma is the most common benign growth and arises from both of these types of tissue (Baum *et al.* 1994). It is a proliferation of glandular and/or stromal cells, with varying amounts of fibrous and epithelial elements. This lesion is not a pre-cancerous condition and so is considered a non-malignant abnormality. It is seen as a well-defined lump. Fibrocystic change (FCC) is considered to be a normal part of the change and development of breast tissue throughout a woman's life, due to hormonal cycles. It is a non-disease condition and can be left without treatment. However the symptoms may include a hard painful lump which needs to be distinguished from other more serious conditions.

1.2.3 Current diagnostic techniques

1.2.3.1. Introduction

Breast disease is usually noticed first by the patient who will present a lump or change in breast appearance, or through the national breast-screening programme for women over 50. 80% of lumps removed are benign. Current diagnostic techniques for breast cancer are a combination of clinical examination, mammography, ultrasonography, fine needle aspiration cytology (FNAC) and core needle biopsy (CNB). Sometimes diagnosis may not be achieved until the entire mass is removed (open biopsy) and examined histologically. Which combination of the above techniques is used in a

particular patient's management is based on many factors. Figure 1.3 shows a simplified sequence of a typical patient management flow diagram.

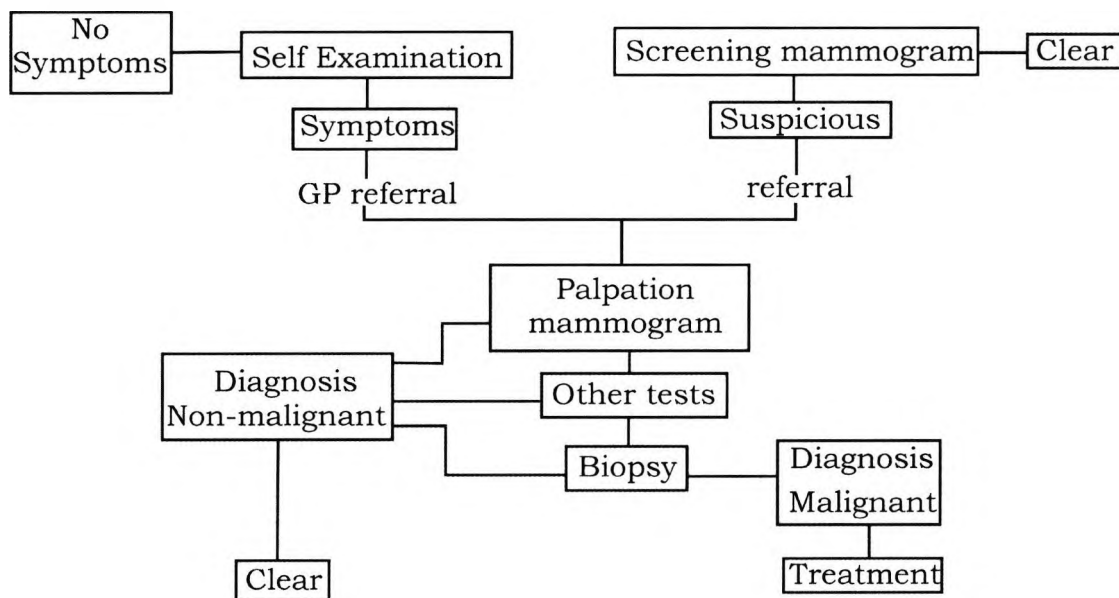


Figure 1.3 A simplified patient management flow diagram for breast disease diagnosis

Each of the tests used in routine breast cancer diagnosis are outlined in the following sections.

1.2.3.2 Breast Self Examination (BSE)

A very important part of the diagnostic process is self examination, especially for women who are under 50 and not part of the National Health Service Breast Screening Programme (NHSBSP). Most breast cancers are found by the patient herself through BSE and a study has shown that the mean diameter of lumps of those presented by women performing BSE is 2.5cm compared to 3.2cm in those not performing BSE on a regular basis (Foster and Costanza 1984).

1.2.3.3 Mammography

Mammography is used for routine screening of women over 50 in the UK as well as investigating suspicious lumps in women of all ages. This technique has a mean sensitivity of 87% for women over 50 falling to 68% for women under 50 (Fentiman

1990). Mammography has remained the primary method of breast cancer detection for the last 15 years. During this time period nearly 15.5 million women have been screened using conventional mammography in the UK and the mortality rate from breast cancer has fallen by more than 20%. Despite the success of this technique it has shortfalls. 3,300 women per year need to be recalled for a repeat test having had a mammography result that was ambiguous.

As well as screening, mammography is used for all patients that have presented with a lump or any other suspicious symptoms such as a rash or nipple discharge. The mammographic image is used as a part of a wider set of diagnostic tests to determine the treatment pathway of the patient. It is routinely used along with palpation and a needle biopsy as the standard diagnostic process. This is because mammography has limited diagnostic ability, which is evidenced from the fact that nearly 30% of women in the 40-49 age group and 25% of the 50+ age group examined in 2002 were given a false positive result, i.e. they have been referred for further tests which prove to be negative (Department of Health 2003). Mammography can be problematic in detecting lesions in dense fibrous breasts or lumps below 10mm in diameter, because essentially it forms an image of differences in attenuation.

1.2.3.4 Ultrasound

Ultrasound (US) is used both to aid diagnosis and to guide biopsy needles to the correct location. US is particularly effective in younger women at distinguishing cysts and benign lesions from malignancy. When used alongside mammography it has been shown to increase the sensitivity of diagnosis from 83% with mammography alone to 91% (Zonderland *et al.* 1991). With US a benign lesion can be differentiated if it has a well defined encapsulated margin and a regular shape. US is usually used as a complementary test once a lesion has been detected with mammography as it is not sensitive enough to be used as a screening tool on its own. It can also be used to see whether the lymph nodes are enlarged, a sign which may lead to a biopsy for nodal involvement and possible metastatic disease. Ultrasound is undertaken by a variety of operators (radiographers, surgeons and radiologists) and is very operator dependent.

1.2.3.5 Other tests

Other tests which can be used as a complement to mammography and US are MRI, scintimammography, PET, Computer Aided Diagnosis and Optical techniques.

1.2.3.6 Needle biopsy

Fine needle aspiration cytology (FNAC) is the most widely used technique for making a pre-operative diagnosis. This is a technique where a syringe is used to remove a sample of cells from the lesion which are smeared on a slide and examined. It is the least traumatic method of cell extraction as a fine (approximately 23 gauge) needle is used. This is performed at a clinic or hospital department and if a histopathologist is not present the sample must be sent away to a laboratory for diagnosis as a high degree of specialised expertise is needed to interpret the results. There are several methods of fixing and staining the sample. The cytological grading is based on examining the cell dissociation, size, nuclear morphology, nuclear margin and chromatin pattern (Robinson *et al.* 1994). A FNAC has a sensitivity of 90% and so may still result in a false diagnosis. A needle biopsy is always needed to confirm the diagnosis of any focal abnormality. If a FNAC is deemed to be inadequate then a core biopsy is performed. This is more invasive than FNAC; a wider gauge needle (approximately 14) is used to extract a larger amount of tissue. This test is easier to interpret due to the larger amount of tissue sampled and so results in a more accurate diagnosis. Excisional biopsy is the method of completely removing the suspicious lump through surgical procedure in order to examine the lump mass. This is the gold standard technique as it is the most accurate and complete results can be obtained in this manner. This is also the most invasive method, which would be impractical, expensive and unnecessary to use as a routine procedure for all suspicious lumps. Typical cell patterns seen on histological slides are shown in figure 1.4. The microscopic appearance of the tissue has several markers that the histopathologist uses to differentiate tissue types.

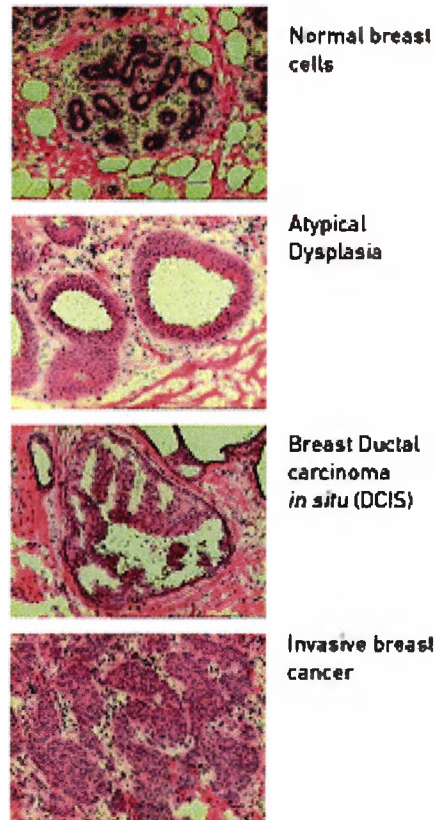


Figure 1.4 Typical cell appearances in histological examination slides

(Arcturus Bioscience 2006)

There are certain types of disease that are more difficult to diagnose than others and there are pre-malignant states of benign disease that, although diagnosed as benign will be managed as though malignant. Additional to this there are factors such as age of the patient and stage of disease that is presented that affect how easily a tumour can be diagnosed. False positive diagnoses have been found to be due to several reasons, such as incorrect tissue sampling, human error, sample contamination from substances such as ultrasound gel or mucus, and poor fixing and staining techniques. The process is also open to interpretive problems. The unequivocal distinction between benign and malignant samples is not always possible. Some conditions including carcinoma in situ, epithelial hyperplasia and fibroadenoma have higher misinterpretation rates (Zakhour and Wells 1999) and may need additional cytological testing or an open biopsy.

1.2.4 Current treatment for breast disease

There are many factors which determine the treatment choices for patients with breast cancer. In most cases surgery is the initial method of treatment, to be followed by radiotherapy, chemotherapy or hormone therapy. The stage and grade of the tumour will be a factor in determining which of these alternatives is chosen. There is an ever increasing trend for lumpectomies to be performed wherever possible, rather than full mastectomies, due to the increased quality of life for the patient post-surgery. A lumpectomy is when the tumour and a margin of tissue only are removed. However, this approach presents an increased risk that microscopic spread of the disease may be missed, which will result in recurrence of the disease.

Currently the only way of checking that the correct margin has been removed is through a frozen section. This is a procedure where a lump of freshly excised tissue is sent to the histopathologist for immediate examination. However this procedure has a number of factors which make it impractical and sometimes impossible for routine use. Very few facilities have an immediately available pathology laboratory and so samples may need to be transported to a separate site for examination, which is time consuming. This not only increases the amount of time the patient needs to be anaesthetised for but is using expensive surgeon and operating theatre time. An American study performed a frozen section analysis on the margins of 160 patients, who would normally have had their margins assessed post-operatively. This study found that 21 of those patients had positive margins requiring re-excision and 7 showed persistently positive margins which resulted in a full mastectomy (Weber *et al.* 1997). These patients would normally have had to return for repeat procedures. The value of having immediate access to information about the excised tissue without needing to rely on a, sometimes remote, histopathology service has the potential to greatly increase the use of conservative breast surgery techniques.

1.3 X-ray interactions with tissue

1.3.1 Introduction

The following section will outline the important interactions involved when x-rays are incident on biological matter. Figure 1.5 illustrates the areas of dominance for each type of interaction. For low energy (<100keV) and low Z, which is the region involved in soft tissue interactions (highlighted by the red box), Compton scattering and the photoelectric effect are the most important. Coherent scattering also occurs, although it is not a dominant interaction it is evident, and it gives rise to the diffraction patterns that are measured during this study. Each of these interactions is detailed in the following section.

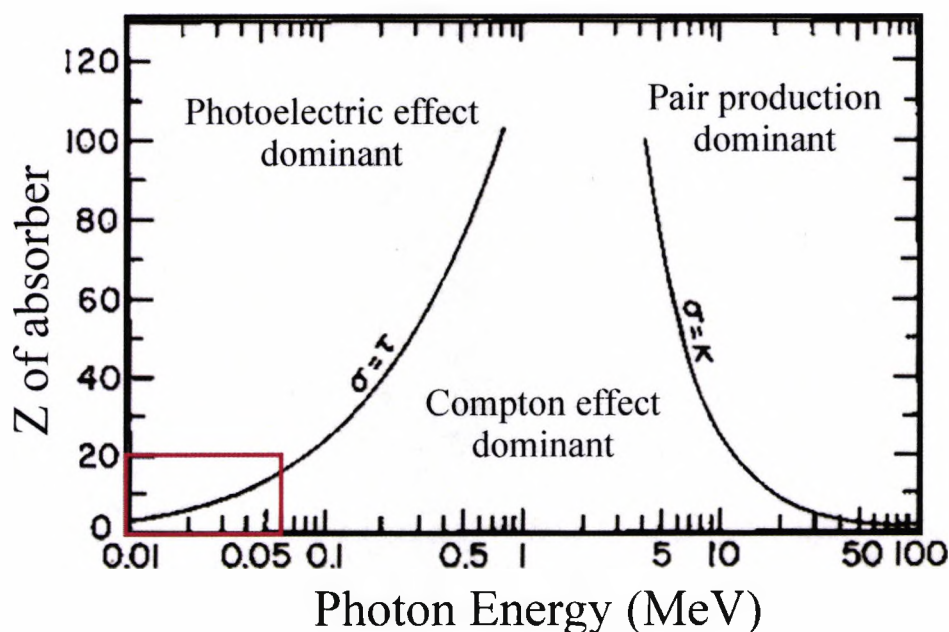


Figure 1.5 A diagram illustrating the dependence of interaction cross sections on energy and atomic number Z

(Evans 1955).

1.3.2 Attenuation

Figure 1.6 below illustrates x-rays passing through a thickness dx of a material with a linear attenuation coefficient μ . where I_0 is the number of counts incident on the material and I is the number of transmitted counts.

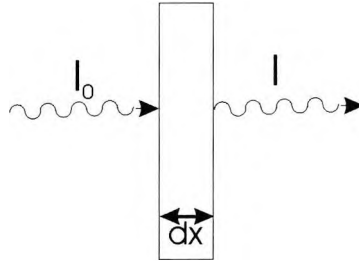


Figure 1.6 Linear attenuation of a photon beam

The fractional reduction in photon intensity is given by

$$\frac{dI}{I_0} = -\mu dx \quad [1.1]$$

This is integrated to give Beer's Law for exponential attenuation:

$$I = I_0 e^{-\mu x} \quad [1.2]$$

The total linear attenuation coefficient, μ , for a particular medium is a measure of the reduction in total radiation intensity per unit thickness for a beam of photons passing through the material.

The probability that each individual interaction will occur is given by the interaction cross sections, where σ_{tot} is the total reaction cross section

$$\sigma_{tot} = \tau + \sigma_{inc} + \sigma_{coh} \quad [1.3]$$

τ , σ_{inc} and σ_{coh} are the cross sections for the photoelectric effect, incoherent scattering and coherent scattering respectively. Each of these cross sections will be considered in more detail in the following sections. The linear attenuation coefficient is related to the cross section using the following equation:

$$\mu = \sigma_{tot} N \quad [1.4]$$

N is the number of atoms per unit volume, expressed as

$$N = \frac{N_A}{A} \rho \quad [1.5]$$

where N_A is Avogadro's number, A is the atomic weight and ρ is the density.

1.3.3 Photoelectric absorption

The photoelectric effect (PE) is the dominant interaction at low energies. The probability of PE increases strongly with Z.

1.3.3.1 The energetics of photoelectric interactions

During the photoelectric effect the incident photon interacts with an electron and gives up all of its energy. In this interaction the incident photon is completely absorbed. This is possible if the electron involved is an inner shell electron bound to the nucleus, which takes up the recoil. The kinetic energy given to the atom is considered to be zero, and so the energy of the photoelectron (E_e) is given by

$$E_e = h\nu - E_b \quad [1.6]$$

which is the energy of the incident photon ($h\nu$) minus the binding energy of the electron (E_b). Therefore this interaction cannot take place unless the incident photon energy is greater than the binding energy of the electron. For a photon of suitable energy it is four to five times more likely that a K-shell, rather than an L-shell, electron will interact.

After ionisation the atom is unstable and an electron from a less tightly bound shell falls into the vacancy. This process leaves the atom with excess energy which is released by the following three competing processes or a combination of them.

1. Characteristic x-ray emission

The excess energy is released as a photon. This photon is of energy equal to the difference in energy levels of the electron transition. The emitted photon is characterised according to which two electronic sub shells the electron travelled between during the de-excitation of the atom. The K_{α} lines are produced when an electron transfers from the L shell to the K shell. K_{β} lines are produced by a transition between the M and K shells.

A spectrum showing the characteristic lines of a silver target are shown below in figure 1.7. The K_{α} line can be seen at 22.1 keV and the K_{β} lines can be resolved into $K_{\beta 1}$ at 24.9 keV and $K_{\beta 2}$ at 25.5 keV. The fluorescent yield, ω , is the percentage of de-excitation interactions that result in the emission of a fluorescent photon.

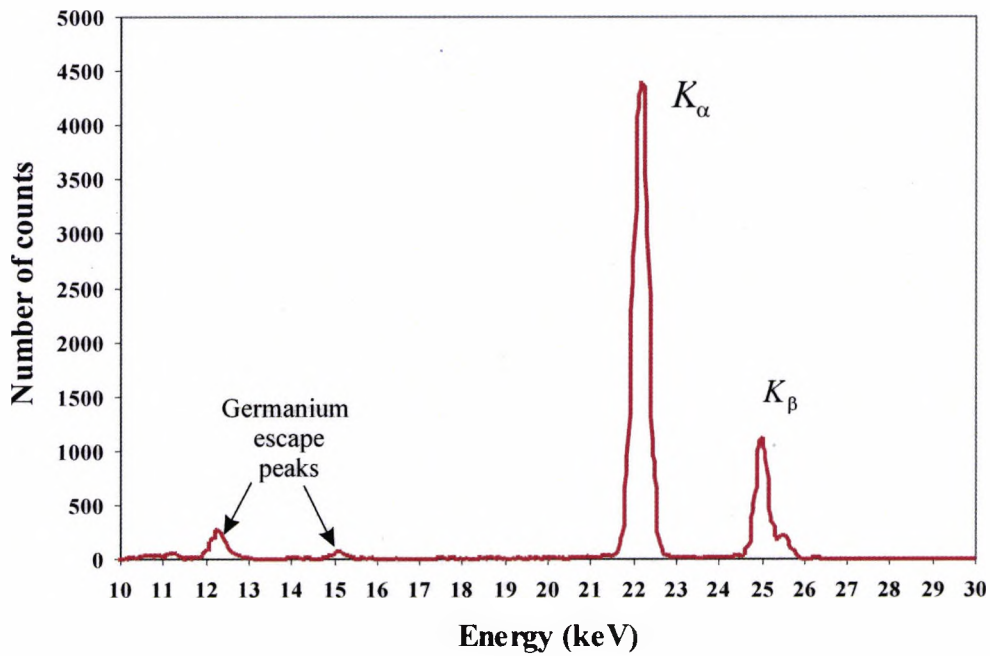


Figure 1.7 Characteristic x-ray emission via the photoelectric effect

The germanium escape peaks seen on the spectra are formed when the characteristic x-rays from the silver target cause the photoelectric effect to occur in the germanium of the detector.

X-ray Fluorescence Spectrometry (XRFS) is a technique that works on the principle that the characteristic x-rays given out by a material are indicative of the composite atoms contained within the material and the quantities present. By measuring the number of x-rays released by the material at an element's characteristic energy the number of atoms present of that element can be calculated.

2. Auger electron emission

The energy is transferred to an outer shell electron, which is ejected from the atom. The kinetic energy of this electron is equal to the difference between the initial electron transition energy and the ionisation energy of the shell that emitted the Auger electron.

3. Coster-Kronig transition

This is an electronic transition within the same sub shell, for example from L2 to L1. As a result a new vacancy is created which is filled by Auger electron emission. This transition does not result in the atom being fully de-excited and so is always followed by a subsequent transition.

1.3.3.2 Interaction cross section for the photoelectric effect

The interaction cross section per atom for the photoelectric effect, τ , is given by

$$\tau \cong k \frac{Z^4}{(h\nu)^3} \quad (cm^2 / atom) \quad [1.7]$$

for energies below 100 keV, where Z is the atomic number, $h\nu$ is the quantum energy of the photon and k is a constant.

As stated in equation 1.6 the photoelectron ejected from the atom has an energy equal to the incident photon energy minus the binding energy of the electron. K-shell electrons are the most important in the photoelectric interaction process, which can be

seen in the high yield for K_α compared to K_β emissions. If the energy of the incident photon is below the binding energy of the electron, this electron cannot be ejected. A plot of the cross section versus photon energy for lead (figure 1.8) shows a sharp rise in interaction probability when the incident photon energy reaches the binding energy of an electron and this electron interaction can occur. This is known as the absorption edge.

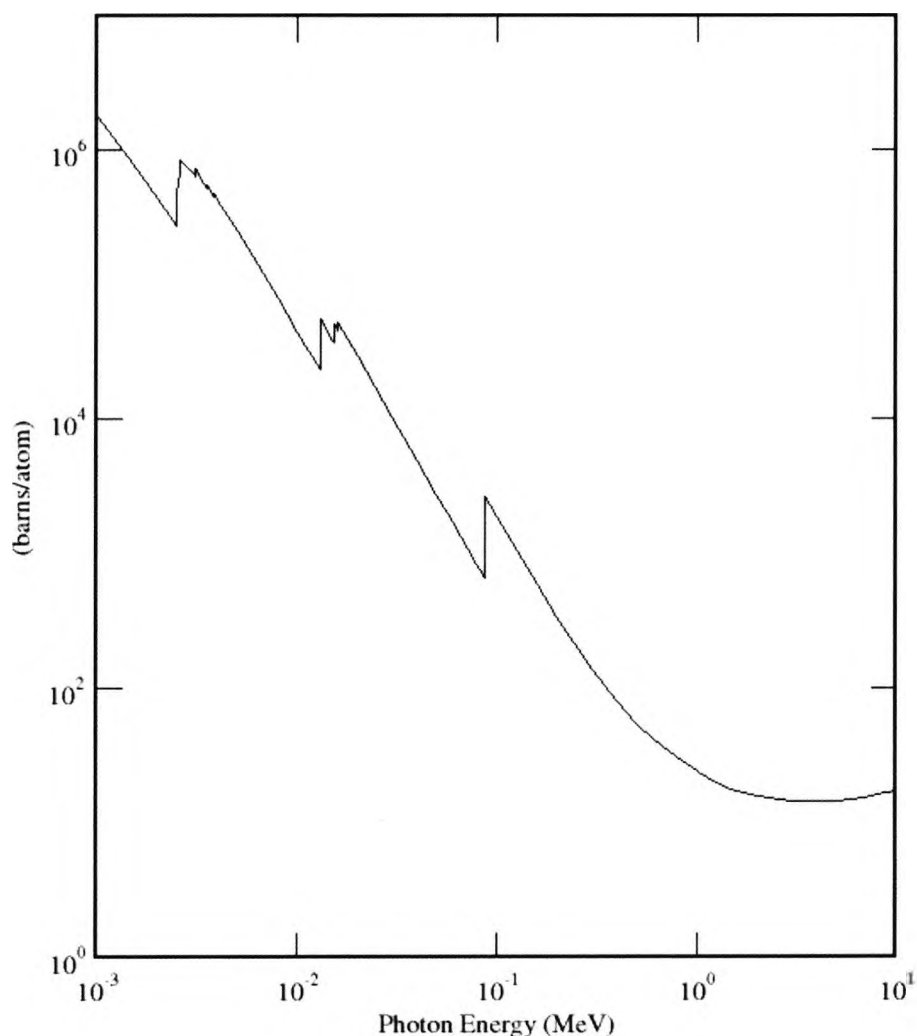


*Figure 1.8 Photoelectric interaction cross section versus incident photon energy for lead
Reproduced from the XCOM database (Berger and Hubbell 1998)*

Due to the complicated involvement of the binding energy of the atom the cross section for the photoelectric effect does not have a simple equation so an approximation, given in equation 1.7, is used for the energy range that is applicable to this study.

1.3.4 Compton Scatter

1.3.4.1 The energetics of Compton scatter

Compton scattering is an interaction that occurs between a photon and an orbital electron. The electron is ejected from the atom and the photon changes direction having given up part of its energy. Figure 1.9 illustrates the Compton interaction, where E_0 is the energy of the incident photon, E_1 is the energy of the scattered photon, E_{e^-} is the rest mass energy of the electron and E_{e^-}' is the total energy of the ejected electron with kinetic energy T . θ is the scattering angle of the photon and ϕ is the scattering angle of the electron.

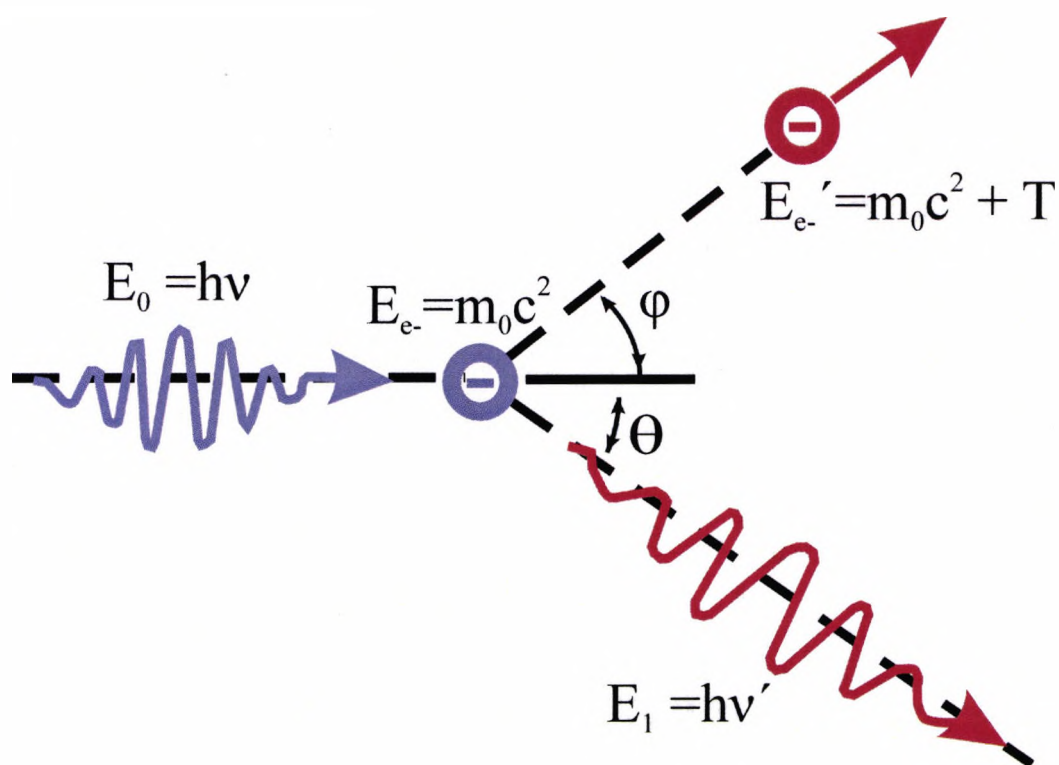


Figure 1.9. The energetics of Compton scattering

The electron taking part in the interaction is assumed to be stationary, i.e. the initial energy (E_0) and momentum of the electron are both equal to zero. The amount of energy transferred to the electron determines the angle of the recoil of the electron and the angle of the resultant photon.

The angle and energy of a Compton scattered particle can be accurately calculated using the principle of conservation of energy and momentum. From the above diagram it can be seen that the incident photon has energy $E_0 = h\nu$ and the scattered photon has energy $E_1 = h\nu'$. Resolving the energy and momentum into parallel and perpendicular components gives the important Compton equation

$$E_1 = \frac{E_0}{1 + \left(\frac{E_0}{m_0 c^2}\right)(1 - \cos \theta)} \quad [1.8]$$

1.3.4.2 Compton cross section

The probability of a photon being incoherently scattered through an angle θ by an unbound electron at rest is described by the Klein-Nishina (KN) differential scattering cross section per unit solid angle, $d\sigma_{KN}/d\Omega$. This approximation is valid for unpolarised x-rays of energies below 100 keV and is given by:

$$\frac{d\sigma_{KN}}{d\Omega}(\theta) \cong \frac{1}{2} r_0^2 \left(\frac{k}{k_0}\right)^2 \left(\frac{k}{k_0} + \frac{k_0}{k} - \sin^2 \theta\right) \quad (cm^2 sr^{-1} electron^{-1}) \quad [1.9]$$

in which k_0 is the ratio of the incident photon energy to the electron rest mass energy and k is the ratio of the scattered photon energy to the electron rest mass energy.

These are given by

$$k_0 = \frac{h\nu}{m_e c^2} \quad [1.10]$$

$$k = \frac{h\nu'}{m_e c^2} \quad [1.11]$$

and r_0 is the classical electron radius

$$r_0 = \frac{e^2}{4\pi\epsilon_0 m_0 c^2} \quad (m) \quad [1.12]$$

This cross section is dependent on the momentum transfer \bar{x} , which is defined as:

$$\bar{x} = \frac{1}{\lambda} \sin\left(\frac{\theta}{2}\right) \quad [1.13]$$

where λ is the wavelength of the incident photon and θ is the angle through which the photon is scattered. The KN cross section is the differential cross section per unit solid angle. To find the total cross section this must be integrated over all solid angles.

Figure 1.10 is a polar plot of the Compton scattering cross section for various incident photon energies, where

$$\alpha = \frac{h\nu}{m_0c^2} \quad [1.14]$$

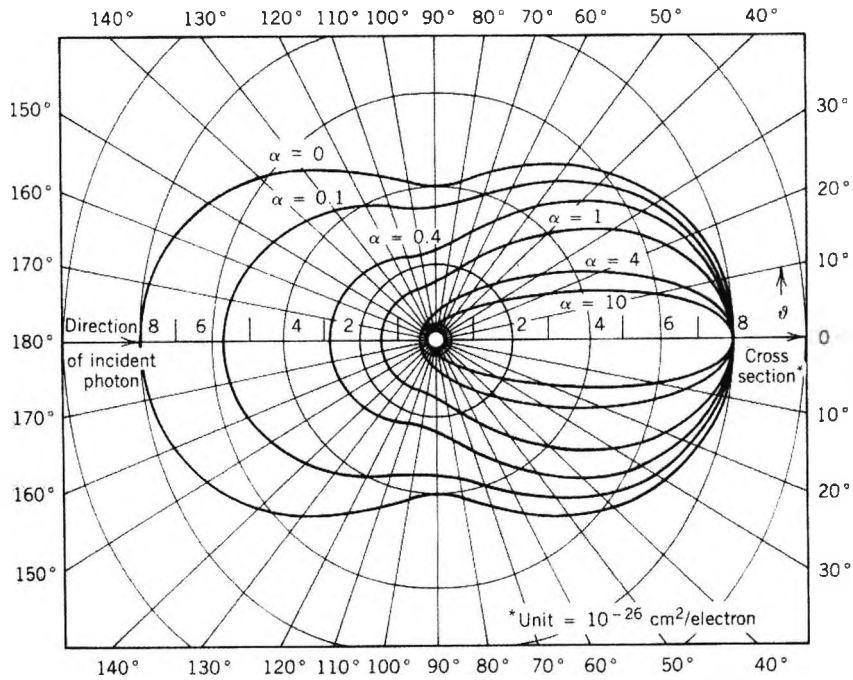


*Figure 1.10 The Compton scattering cross section for various incident energies
(Evans 1955)*

This figure shows that as the incident photon energy increases Compton scatter increases in the forward direction. It also shows that scatter is at a maximum in the forward direction and at a minimum at 90° for lower photon energies.

1.3.4.3 The effects of binding energy on Compton scatter

Binding energy is significant for low energy photons and high Z materials. The energies used within this study are in the region where the binding energy of the atom and the momentum of the electron must be considered. Two main effects are seen:

1. Doppler broadening

The motion of the orbital electron taking part in the interaction causes a broadening of the apparent energy of the incident photon, which leads to a broadening of the Compton scatter peak for a given angle. This is called Doppler Broadening and the measure of the spread of the Compton peak is a measure of the Compton profile.

2. Change in reaction cross-section

The electron binding energy reduces the probability of Compton scatter interactions occurring at low incident photon energies. This is accounted for by multiplying the KN cross section by a corrective factor, the incoherent scattering function $S(\bar{x}, Z)$ to get a binding energy corrected (BEC) differential cross section:

$$\frac{d\sigma_{BEC}(\theta)}{d\Omega} = S(\bar{x}, Z) \frac{d\sigma_{KN}(\theta)}{d\Omega} \quad [1.15]$$

Figure 1.11 is a graph of the ratio of cross sections against atomic number. This graph shows how large the effect of the electron binding energy is on the interaction cross sections at low (<100keV) energies.

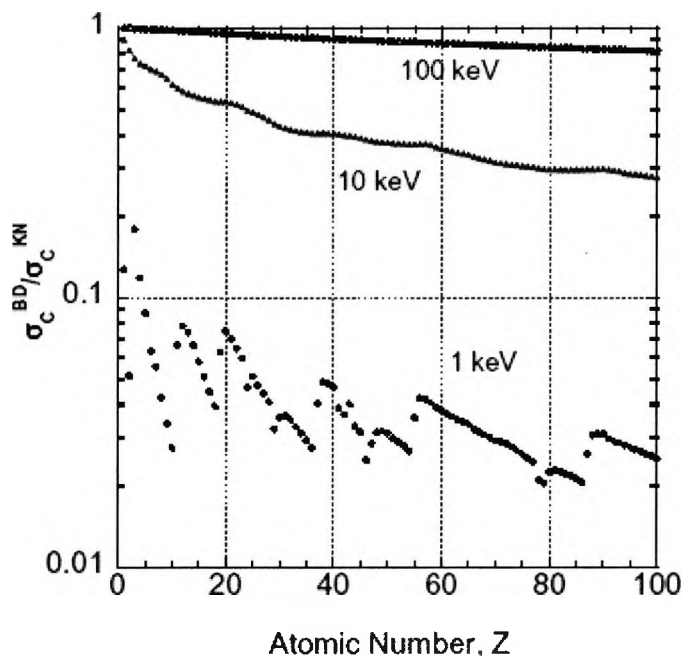


Figure 1.11 A graph showing the ratio of the bound-electron Compton scattering cross section to the free electron Compton scattering cross section. (Hirayama, 2000)

It is usual to define $S(\bar{x}, Z)$ using the Waller-Hartree approximation (Waller and Hartree 1929) which takes the electron binding for the whole atom into account. This is given as:

$$S(\bar{x}, Z) = \sum_{m=1}^Z \sum_{n=1}^Z \langle \psi_0 | \exp(i\bar{x} \cdot (\bar{r}_m - \bar{r}_n)) | \psi_0 \rangle - \left| \sum_{m=1}^Z \langle \psi_0 | \exp(i\bar{x} \cdot \bar{r}_m) | \psi_0 \rangle \right|^2 \quad [1.16]$$

where \bar{x} is the momentum transferred during the reaction, ψ_0 is the ground state wave function, \bar{r}_n is the position of the n^{th} electron and \bar{r}_m is the position of the m^{th} electron within an atom of atomic number Z . (Hubbell *et al.* 1975) have reviewed the computational methods used by various authors to obtain incoherent scattering functions and has extensively tabulated them for all elements of the periodic table.

Veigele *et al* (1966) produced a simplified formula for calculating S based on the Thomas-Fermi model of the atom:

$$S(V) = Z \left[1 - \exp(-4.88V^{0.856}) \right] \quad [1.17]$$

where

$$V = \frac{2}{3} \frac{137\lambda_c}{Z^2 \lambda} \sin \frac{\Theta}{2} \quad [1.18]$$

λ_c is equal to $\frac{h}{m_e c}$, λ is the wavelength of the incident photon and Θ is the angle between the incident and scattered photon. Values of $S(\bar{x}, Z)$ have been formulated using semi-empirical methods or interpolation of the incoherent scattering function tables published by (Hubbell *et al.* 1975). This method has been employed in this work, which is explained in Section 3.2.

The incoherent scattering coefficient, σ_{inc} , is given by:

$$\sigma_{inc}(\bar{x}, Z) = \rho N_A \frac{d\sigma_{KN}}{d\Omega} \frac{S(\bar{x}, Z)}{M} \quad (m^{-1} sr^{-1}) \quad [1.19]$$

and is the probability that a photon will be Compton scattered when interacting with a material of density ρ and molecular mass M . N_A is Avogadro's constant. At high values of \bar{x} , $S(\bar{x}, Z)$ becomes equal to Z .

1.3.4.4 Polarisation effects

For linearly polarised photons interacting with a free electron the Klein-Nishina angular distribution function per steradian of solid angle Ω is:

$$\frac{d\sigma_{KN}}{d\Omega} = \frac{1}{4} r_0^2 \left(\frac{k}{k_0} \right)^2 \left(\frac{k}{k_0} + \frac{k_0}{k} - 2 + 4 \cos^2 \Theta \right) \quad [1.20]$$

where k , k_0 and r_0 were defined in equations 1.10, 1.11 and 1.12. Θ is the angle between the incident polarisation vector and the scattered polarisation vector.

1.3.5 Coherent scattering

When a photon scatters without losing any of its energy it is called a coherent scatter event. The recoil is absorbed by the interacting atom as a whole; and there is no excitation of this atom as it does not absorb any energy. The angle that the photon is scattered through depends on both the energy of the incident photon and the Z of the absorber. Coherent scattering is relevant for the same low energy, high Z region where electron binding energy influences Compton scatter.

1.3.5.1 Coherent cross section

The classical theory states that coherent scattering takes place when an incident photon interacts with an atomic electron. The probability of this occurring is given by the Thompson scattering differential cross section, $\frac{d\sigma_{Th}}{d\Omega}$:

$$\frac{d\sigma_{Th}}{d\Omega} = \frac{r_0^2}{2} (1 + \cos^2 \varphi) \quad (cm^2 sr^{-1} e^{-1}) \quad [1.21]$$

where r_0 is the classical electron radius and φ is the azimuthal angle. This theory has been adapted to account for the fact that the photon does not interact with a single electron but with all the electrons in the atom as a combined charge distribution. This is taken into account with the form factor, $F(\bar{x}, Z)$. F^2 is the probability that an incident photon will be scattered by the atomic electrons without any loss of energy and the recoil momentum is absorbed totally by the atom. The Thompson cross section is the probability that coherent scattering will take place with a single electron, this multiplied by F^2 gives the probability that coherent scattering will take place with an atom as a whole.

The linear coherent scatter cross section, σ_{coh} for unpolarised photons is given as:

$$\sigma_{\text{coh}} = \rho N_A \frac{F^2(x)}{M} \frac{d\sigma_{\text{th}}}{d\Omega} \quad (\text{cm}^{-1} \text{sr}^{-1}) \quad [1.22]$$

where

$$\frac{F^2}{M} = \sum_i \frac{F_i^2(x)}{m_i} \omega_i \quad [1.23]$$

Molecular form factors indicate how experimental results deviate from traditional theoretical calculations based on the assumption that electrons involved in scattering interactions are free. $F(\bar{x})$, as stated above, is the molecular form factor, which can be expressed as (Narten and Levy 1971):

$$F^2(\bar{x}) = f^2(x)[1 + H(\bar{x})] \quad [1.24]$$

where $f^2(\bar{x})$ is the form factor calculated using the Independent Atomic Model (IAM). This model assumes that there are no inter-molecular interference effects and so is the theoretical form factor for free atoms. $H(\bar{x})$ is the oscillatory structure function and is a measure of the coherent interference pattern.

1.3.5.2 Polarisation effects

The Thomson scattering cross section per electron for a linearly polarised incident photon beam of energy E from an atom with atomic number Z is given as follows:

$$\frac{d\sigma_{\text{th}}}{d\Omega} = r_0^2 \cos^2 \Theta \quad [1.25]$$

Θ is the angle between the incident polarisation vector and the scattered polarisation vector.

1.4 Literature review

The application of utilising Compton scatter has mainly been limited to bone densitometry (Olkkonen and Karjalainen 1975; Speller *et al.* 1989; Webber and Kennett 1976). A variety of approaches have been taken with regard to the number of radioactive sources and detectors that are used. All methodologies, however, work on the principle that the intensity of Compton scattered photons is proportional to the number of available scattering sites within the scattering volume.

Webber and Kennett (1976) designed a system using square portions of dry bone. This was then developed into a clinical system. They used two sources and two detectors configured at 90° to each other. Two sources were used, a Sm-153 source filtered to give a monoenergetic beam at 103 keV and a Tm-170 source with a photon energy of 84.3 keV. The energy of the second source is chosen to be as close to the energy of the Compton scattered photons from the Sm-153 as possible. This is so that the assumption can be made that the linear attenuation coefficient of the low energy source is approximately equal to the linear attenuation coefficient of the Compton scattered photons. The electron density, ρ_{e^-} , is calculated as:

$$\rho_{e^-} = k \left(\frac{S_1 S_2}{T_1 T_2} \right)^{1/2} \quad [1.26]$$

where k is a constant, which can be measured using a material of known density, i.e. water. S_1 and T_1 are the number of transmitted and scattered counts from the Tm-170 source and S_2 and T_2 are the scattered and transmitted counts from the Sm-153 source. Using this method the electron density was then used to calculate the physical density using tabulated values of Z/A for water and bone. The study was then carried out on 12 healthy volunteers, measuring the density of the *os calcis* in the foot. The errors were found to be very large, due to the excessive attenuation of the low energy photons by soft tissue.

Webber and Coates (1982) developed a system using the same sources (Sm-153 and Tm-170) but using 3 sources and 3 detectors, to eliminate the need to rotate the sample. This system was used to measure the lung density of human volunteers.

Other groups have used similar techniques to measure the density of bone. Clarke and Vandyk (1973) utilised the same beam arrangement but used a Co-60 and a Cs-137 source. Olkkonen and Karjalainen (1975) arrive at the same equation to calculate the electron density but use only one source (Tm-170) and one detector. They place the detector in three different positions, at 150°, 180° and 210° from the source, and rotated the sample once to obtain scatter and transmission measurements. In order to avoid using two energies the experiments were made with a low energy source (84 keV) and a small scattering angle (30°). The assumption is then made that the energy and attenuation coefficient of the scattered photons are approximately the same as the incident photons.

Duke and Hanson (1984) looked at the possibility of using a polychromatic x-ray source to overcome the problems associated with using sealed sources. The high output and small focal spot of an x-ray tube improves the spatial resolution of the system and shortens measurement times making this a more viable clinical technique. This paper also takes into account the effects of Compton energy shift, multiple scatter and sample composition uncertainties, factors that have been assumed to be negligible by other groups. Bias correction factors (bcf) are calculated using computer modelling to account for beam hardening of the polychromatic source. A system was then developed for measuring lung density.

A slightly different approach was taken by Huddleston and Sackler (1985), who used a 90° geometry with an Ir-192 source. Tubes of the materials under investigation were placed inside a second material (water) and scatter measurements were made using the dual energy output of the Iridium source (317 and 468 keV photons). The diameter of the inner sample was varied and scatter against diameter was plotted to find an equation of the form

$$I_s(E) = \alpha \exp - \beta d \quad [1.27]$$

where I is the intensity of scattered photons and d is the diameter of the sample. α is a product of the electron density and the average scatter intensity per electron and β is the sum of the linear attenuation coefficients of the two substances. The dual energy

method means that these values can be found and no transmission measurement is needed.

Al-Bahri and Spyrou (1998) developed a system using a single Am-241 source and a single detector with a 90° geometry. The calculation of electron density did not take attenuation of the source into account as the measurement volume contained the entire sample and some surrounding air. The tissues had been freeze dried before measurement and were corrected for this using the weight of the water removed. This study was the first to attempt to characterise breast tissue using this parameter. Paired samples from nine patients were analysed. The results found that adipose had lower electron density than the malignant tumour samples with a 3% difference between them. The electron density values published were malignant 3.546×10^{23} electrons per cm^3 ; adipose 3.463×10^{23} electrons per cm^3 and healthy glandular tissue 3.482×10^{23} electrons per cm^3 . However the study found that there was a large spread of results for each tissue type and the differences found were ambiguous due to the experimental error being 5%.

Coherent scattering and diffraction patterns have been much more widely applied to the area of breast tissue characterisation. Narten and Levy (1971) first measured the Wide Angle X-ray Scattering (WAXS) pattern of water and tabulated the coherent scatter coefficients against the momentum transfer. This set a gold standard, not only for the scatter cross-section measurements, but as an experimental gold standard for measures made of other materials. Since then this method has been used to interrogate a variety of biological materials.

Evans *et al.* (1991) proposed a method applying a coherent scattering technique for breast tissue characterisation. In total 19 breast tissues were investigated and 3 breast equivalent materials (water, olive oil and Perspex). The data was analysed by measuring the peak height and the FWHM of the main peak of the recorded diffraction patterns. The group concluded that there was a measurable difference between normal and diseased tissue, however they found no significant difference in the peaks for benign and malignant tissue. This study only included one benign and

four carcinoma samples and this sample size is not adequate to detect the small differences that are expected.

Tartari *et al.* (1997) investigated the scattering properties of non-biological materials (water, PMMA and carbon black) and animal fat. They used an x-ray source and a Siemens D-500 powder diffractometer to obtain a monoenergetic beam of 8.0keV. The results for PMMA and fat were compared to the results from Kosanetzky *et al.* (1987) and whilst the PMMA values were comparable, the fat values were not. This was assumed to be due to differences in fat sample preparation.

Peplow and Verghese (1998) looked at animal tissues and human breast tissue, with an aim of assessing breast equivalent materials, used as phantoms in mammography. This study used a synchrotron source at two energies, 20 and 8 keV. This study only looked at one unclassified human breast tissue sample, and so has a very small sample size. The results are displayed in terms of molecular form factor over the square root of molecular weight $\left(\frac{F}{\sqrt{M}}\right)$ versus momentum transfer (\bar{x}) . This is a composite scattering factor that is calculated without knowledge of the molecular formula. This is useful when using tissue samples as the precise molecular formula is not known.

Kidane *et al.* (1999) have examined the structure of normal and diseased breast tissue in terms of x-ray scatter signatures. The group looked at 100 histopathologically classified samples including 8 benign and 30 carcinoma samples. They found a large difference between adipose and other types of tissue. However, no significant difference was observed between fibroadenoma, carcinoma, fibrocystic change and benign tissues. The measurements were made using an energy dispersive technique, i.e. a polychromatic source was used with a fixed scattering angle. The inaccuracy caused by source polychromacity may have masked measurable effects.

Poletti *et al.* (2002) have proposed a method to facilitate the measurement of scatter profiles using a lab based x-ray set. This method is tested on amorphous samples (Lucite), adipose and glandular breast tissue, and eight breast equivalent materials. The samples used were water, PMMA, nylon, polyethylene and 4 commercial breast equivalent materials. The breast tissues used were 4 adipose and 3 glandular tissue

samples from mastectomy procedures, but here there were no diseased tissues involved.

The work performed to date by our group involving the classification of breast tissue has focused on the use of coherent scattering combined with x-ray fluorescence (XRF) to measure differences in the elemental composition of diseased and normal tissue. Geraki *et al.* (2004) describe a technique using coherent scattering profiles to determine the relative proportions of adipose and fibrous tissue within a sample. This information is used to normalise the XRF signal from iron, copper, zinc, and potassium within normal and diseased breast tissue. It was found that all four elements are present in elevated levels in diseased tissue. The work was taken a stage further, using a combination of these two measurements in a multivariate analysis technique to differentiate between tissue types (Farquharson and Geraki 2004b). A partial least-squares regression and principal component analysis was used to create a prediction model which was then tested on 17 samples and found to be able to predict 77.8% that were normal correctly and 77.2% that were diseased correctly.

Wide angle x-ray scattering has been used to act as a method of contrast improvement when used in conjunction with conventional x-ray planar imaging (Griffiths *et al.* 2004b). The technique of Diffraction Enhanced Breast Imaging (DEBI) has been developed as an improvement to mammography by capturing the scatter signal at the position of maximum scatter contrast for breast tissue types, where the adipose signal is at a peak. A beamline at the Elettra Synchrotron was used to scan a breast phantom at 18keV, an energy close to that of mammographic imaging. Images were produced with a low light level CCD, which have shown to offer a contrast twice the level of that obtained with mammography alone.

A similar method has been used to produce enhanced tomographic images. Kosanetzky *et al.* (1987) developed a system for combining diffraction with computerised tomography to produce an axial image. In order to optimise the CT system they measured the diffraction patterns (scatter profiles) of plastics and biological materials. They were the first group to display these profiles in terms of scattering cross-sections against momentum transfer. They looked at water, plastics, fat, muscle, blood, liver, bone and brain tissue using low energy (6.93 keV). They

found that different tissues did produce characteristic scattering patterns, with differences greater than the contrast offered by conventional CT. A similar method has been used in the development of a micro CT system at University College London (UCL) for the diffraction CT imaging of excised breast tissue. (Griffiths *et al.* 2004a). This also makes a complementary measurement to the transmission signal detection with scatter detection at a fixed angle, corresponding to the adipose peak at 1.1nm^{-1} .

The most recent study, performed by Castro *et al.* (2005), has used the coherent scatter profile of adipose tissue to form a tomographic image of the adipose content of fixed breast tissues. They carried out simultaneous measurements of the transmission and scatter images across a plane within the tissue with detectors fixed at zero and 13° , the position of the adipose diffraction peak at 11keV. The study showed qualitative improvements to the visibility of carcinoma tissues, but this was a preliminary study using two tissue samples and so does not have enough results to be able to quantify any image improvements.

More conclusive breast tissue characterisation has been achieved by the use of small angle x-ray scattering (SAXS), which is an investigation at momentum transfer values of less than 0.25 nm^{-1} . This type of measurement shows the interference due to the collagen structures within the tissue, rather than the molecular spacing, as it interrogates structures of the order of 10 to 1000 nm. Lewis *et al.* (2000) examined breast tissue from 43 patients using SAXS. The tissues were classified into three groups; benign, malignant and healthy. The results showed the three tissue types produced scattering patterns which were distinct from one another. They suggest that the underlying collagen structure of the tissue is broken down when a malignancy occurs and the composition of benign and normal tissues differs in collagen type. This work is being developed into a technique to produce maps of the collagen distribution within ex-vivo breast tissue samples using a raster scanning pattern and synchrotron radiation (Wilkinson *et al.* 2004).

Fernandez *et al.* (2002) also suggest that collagen plays an important role in the malignant changes of tissue. This study looked at the SAXS patterns of healthy and diseased tissues and concluded that benign and normal tissues have ordered structure due to the collagen fibrils but this order is lost when the tissue has been invaded with

a malignancy. The study also established that there are large differences in the molecular and supra-molecular size and structure within the tissue when diseased tissue is compared to normal tissues.

Avtandilov *et al.* (2000) used ultra low angle x-ray scatter (ULAX) to interrogate 1000 samples of healthy and malignant tissues. This study used the total scattered integral intensity and total scattering power to quantify contrast and found significant difference between tissue types. The conclusion made is that ULAX is a consequence of the extra cellular matrix (ECM) surrounding the cells, and the detected contrast is measuring the change in the ECM in response to malignant invasion. This correlates well with the findings of the other two studies described above, as collagen is the major component of the ECM.

These studies have all been carried out using synchrotron radiation sources, utilising the high coherence over long distances. However the obvious disadvantage of these techniques is that they do not easily translate to a clinical environment. Round *et al.* (2005) have developed a SAXS system that uses a laboratory x-ray source. They tested normal samples from 4 patients and malignant tumours from 18 patients using a diffractometer. This was designed with an 8.05keV beam from a monochromator and an image plate. They found a statistically significant difference between the two tissue types offering a realistic prospect of clinical system development.

The refractive index, n , of an object is given by the equation

$$n = 1 - \delta + i\beta \quad [1.28]$$

where δ is the phase shift and β is the absorption. This shows that when an x-ray passes through a material of differing permittivity and/or permeability it suffers a shift in phase. The resultant wave is travelling at a new velocity V and this shows as an apparent change in direction. The angular deviation induced by this change in phase is very small, typically only a few μ radians. This refraction can be exploited by detecting the interference patterns produced when refracted and non-refracted waves combine at the boundary between two materials of differing refractive index.

There has been a large amount of research into imaging using refraction effects to enhance standard images. This is a relatively new technique proposed by Chapman *et*

al. (1997) at the Brookhaven National Laboratory. It is a technique that lends itself well to the use of synchrotron sources due to the high coherence of this radiation. Diffraction Enhanced Imaging uses an analyser crystal placed in the exit beam to act as a collimator with a very small acceptance angle. The analyser crystal uses Bragg diffraction from its surface to only reflect radiation of a specific wavelength to the detector surface, hence the name diffraction enhanced imaging. Figure 1.12 shows a typical experimental set-up for DEI

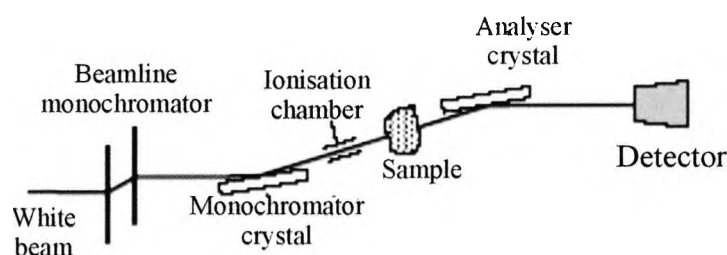


Figure 1.12 Diffraction Enhanced Imaging typical experimental set-up

(Bravin 2003)

Various authors have used this technique to analyse breast tissue (Fernandez *et al.* 2005; Kiss *et al.* 2004). Pisano *et al.* 2000 have used the synchrotron source at Brookhaven to image 7 breast samples using DEI. The *ex-vivo* sample images were correlated with histopathological information and found that the increased spiculation visualisation correlated with the disease process. These were all picked out as an improvement to conventional images by a radiologist.

Lewis *et al.* (2001) have scanned breast phantoms using a slot beam 30mm wide and 0.5mm high, moving the phantom vertically through the beam. The experiments were performed at energy 20keV with the detector at a distance of 1.5m. The image quality was graded using the Leeds TOMAM and biological phantoms, offering a better image quality score at a lower Mean Glandular Dose (MGD). A number of biological tissues were also imaged, including mouse liver, lungs, heart and legs. The contrast enhancements are demonstrated visually but not quantified. The work is being developed at the Synchrotron Radiation for Medical Physics (SYRMEP) beamline at the Elettra synchrotron in Trieste and is also being tested at Daresbury SRS (Cheung *et al.* 2003) to look at breast cancer and metastases.

Phase contrast enhancement is a technique that works on a similar principle but it does not have an analyser crystal after the beam. This technique, called Phase Contrast Enhancement was first proposed by Wilkins *et al.* (1996) as a method that could be appropriate for use with a conventional x-ray tube. In this technique the refraction effects cause enhancement of boundaries between two materials of differing refractive indexes which produces edge enhancement on an image. Kotre and Birch (1999) have used the same technique applied to mammography. The Leeds TORMAM phantom was used to assess the image contrast improvement. This phantom contains aluminium disks of decreasing diameter. Three observers found that these contrast details were easier to detect with the phase contrast imaging system.

Chapter 2 Experiment preparation

2.1 Introduction

The experimental work for this study was carried out using two different environments. Measurements were performed with both a conventional x-ray tube source and with a synchrotron source. The first scatter profile measurements were made on 15 samples at the Daresbury Synchrotron Radiation Source (SRS). These samples, and an additional 15, were then used in the laboratory for both electron density measurements and Energy Dispersive X-ray Diffraction measurements. A second set of 50 samples were measured in the laboratory using the same set-up but revised sample holders. These samples were taken to the European Synchrotron Radiation Facility (ESRF) where angular dispersive diffraction and electron density measurements were carried out.

All laboratory work was carried out at the Radiation Laboratory at City University. The equipment set-up had to be designed, aligned and calibrated. A number of preparatory procedures were performed, which consisted of aligning the collimators, determining the detector resolution and calibrating the Single and Multi Channel Analysers. The techniques used to carry out each of these procedures are outlined in section 2.2. The equipment and set-up for the measurements made at two synchrotron sources are described in section 2.3. Section 3 gives a detailed description of the samples, how they were prepared and the sample holders used for all of the experiments

2.2 Laboratory experimental set-up

2.2.1 Equipment

It was important to be able to measure the sample in the same position with the detector set to measure the signal at several different positions. This was the motivation for designing the following experimental set up. A diagram of the experimental equipment set-up is shown in figure 2.1.

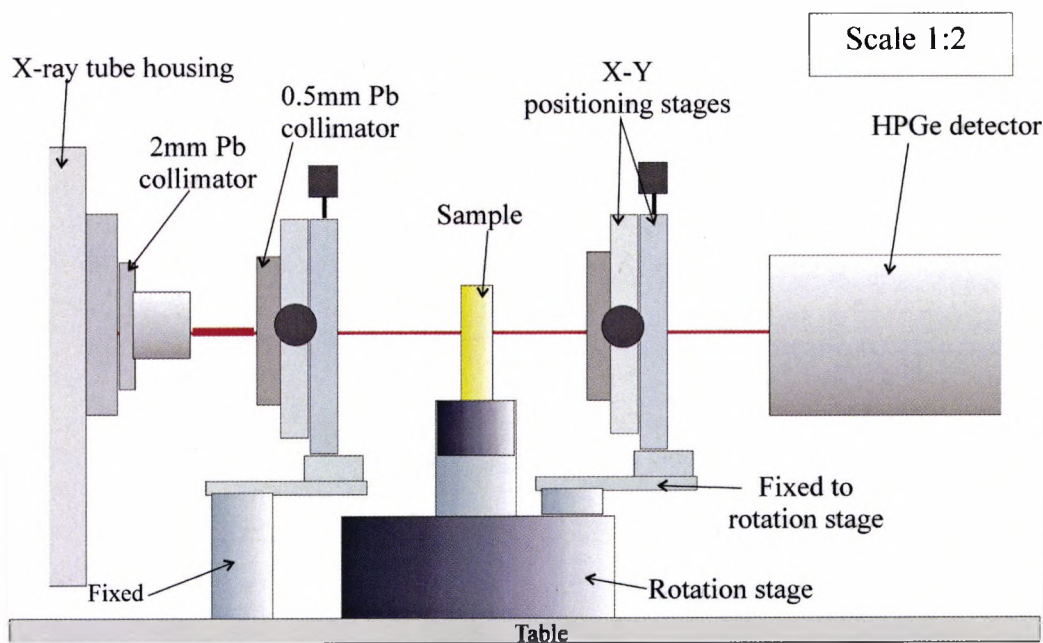


Figure 2.1 The equipment set-up used at City University Radiation Laboratory

The experiments were performed using a Pantak HF160 industrial x-ray tube. This was collimated by one lead and aluminium plate collimator on the tube housing and another close to the sample. A third collimator was used post sample in order to reduce the amount of unwanted scatter reaching the detector. This third collimator is attached to a graduated rotation stage so that it may be very accurately moved around a centre of rotation, situated at the centre of the sample. This allows for alignment of the sample so that the same part of tissue can be irradiated with the detector in different positions.

The sample was mounted on a second rotation stage which allows the sample to be rotated manually. This was so that during a measurement the sample orientation can be altered to average out any effects due to sample inhomogeneity.

Figure 2.2a shows the two axes of rotation within the measurement system. Figure 2.2b illustrates the set-up of the collimator and detector when they have been set in a position to measure a scatter signal.

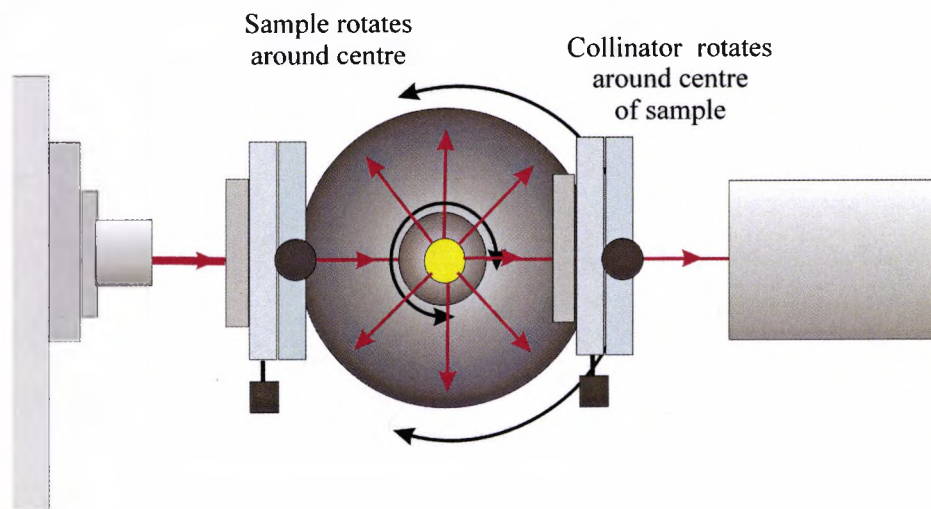


Figure 2.2a The axes of rotation of the experimental system. The detector is at zero degrees
(Not to scale)

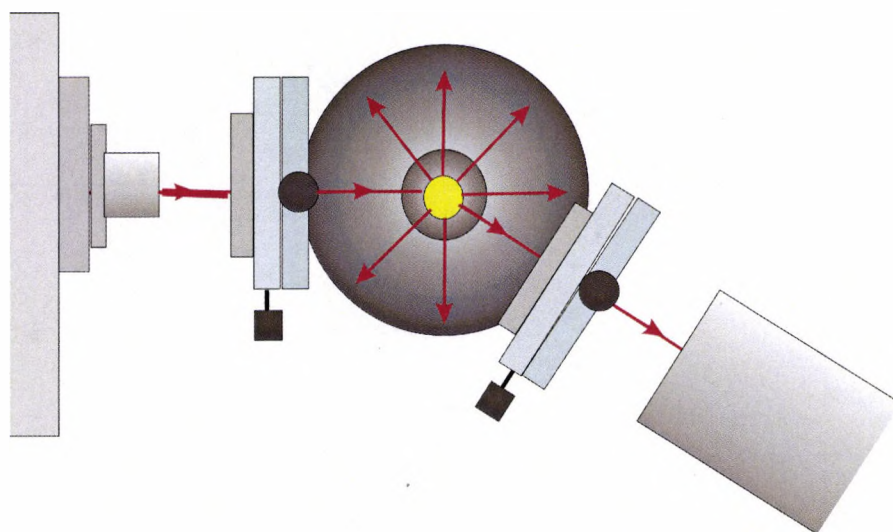


Figure 2.2b The system with the detector at thirty degrees
(Not to scale)

An HPGe detector was used because of its superior energy resolution at the energies used for the experiments. The detector has an inbuilt pre-amp which is in turn is connected to an amplifier and then a multi channel analyser. A PC was used to analyse and capture the spectra using Ortec Maestro software (EG&G Ortec) via an Ethernet card. An additional program was used to transfer the data recorded in Maestro to an Excel spreadsheet (Allday 2002). A diagram of the electronics used is shown in figure 2.3.

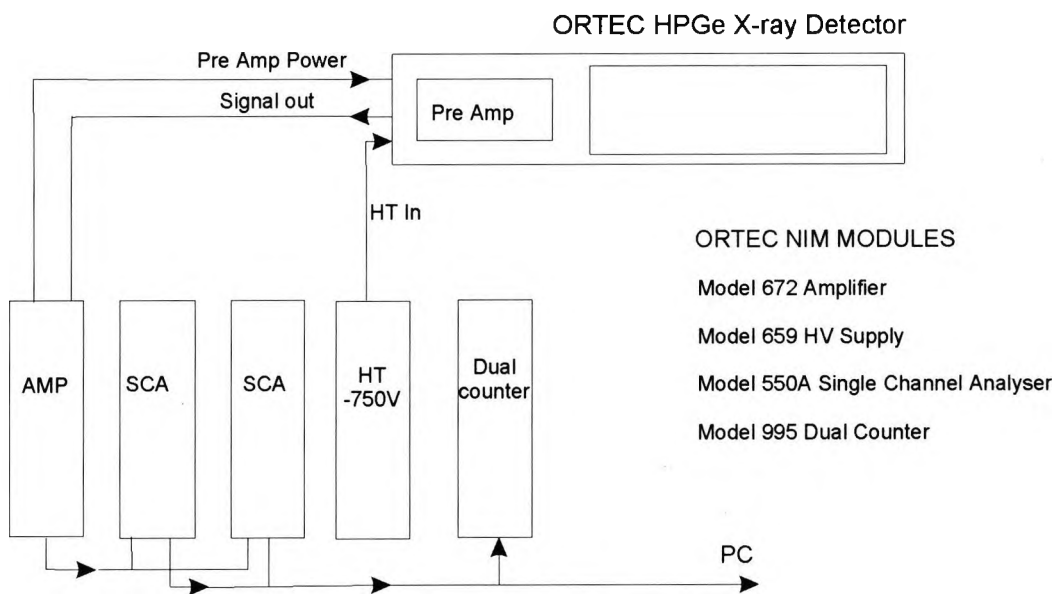


Figure 2.3 The electronics used in the laboratory experiments

2.2.2 Collimator alignment

In order to ensure that the x-ray tube and collimators were correctly aligned a set of measurements were made with an ionisation chamber and radiation sensitive paper. Firstly the position of the primary collimator was checked by making a series of measurements plotting the spatial output of the tube. The output of the x-ray tube varies as a function of distance from the position of where the electron beam strikes the target. In order to gain the maximum signal for the experiment it was essential to ensure that the maximum output was being utilised.

A Keithley 1800cc ionisation chamber was placed outside the tube housing. Each collimator in the beam was mounted on two translators, allowing the collimation hole to be moved in the x and y directions, where the beam axis is the positive z direction. The ionisation chamber was used to make measurements of the dose rate in Grays per second. The collimator was moved in 0.25mm steps over a 5mm area. This was to ensure that there was an overlap for each measurement so that there were no cold areas not mapped. The tube output is shown in figure 2.4

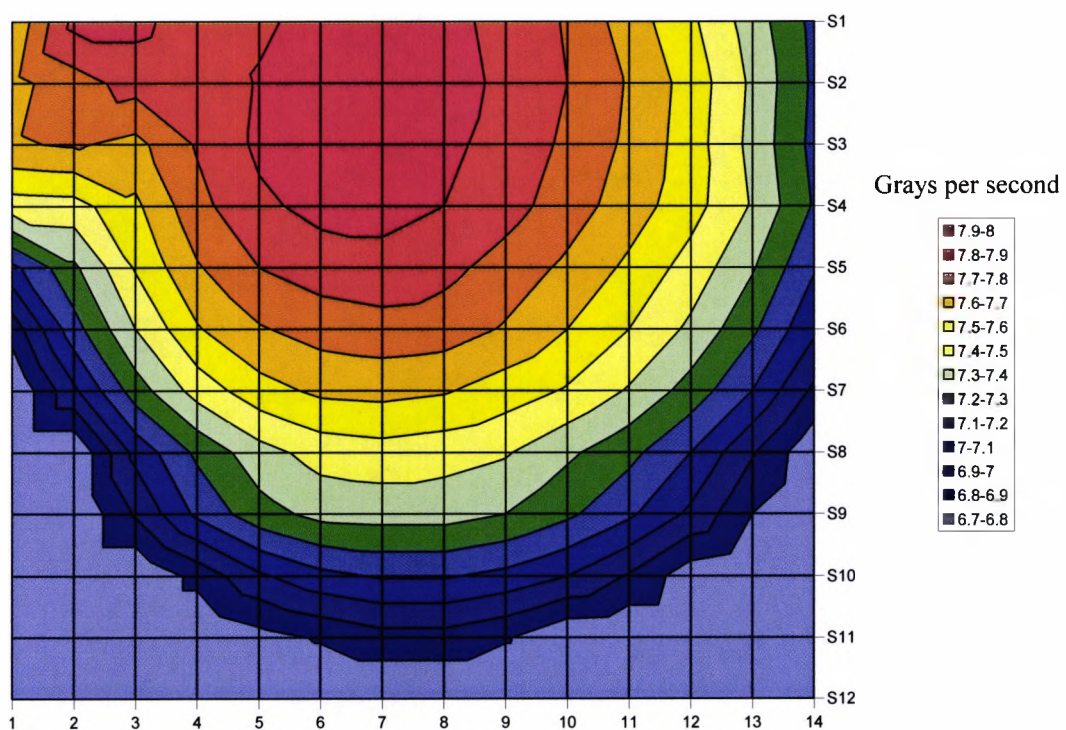


Figure 2.4 An output map of the x-ray tube

Once the collimator on the tube housing was aligned over the central axis of the beam the second collimator was aligned using an identical method. The third collimator which was post sample needed to be positioned correctly using radiation sensitive paper. This is paper that changes colour when it is exposed to x-rays. The output of the tube was not high enough to be registered by the ionisation chamber at this distance.

2.2.3 Detector energy resolution

A peak measured with the Ortec GLP-25300 HPGe detector (detector 1) and a peak measured with the GLP-36360 HPGe detector (detector 2) using an Am-241 source are shown in figure 2.5. The energy resolution is calculated as the FWHM of the peak. For the first detector the energy resolution is 0.435 keV at 59.54 keV (0.73%). Due to equipment failure the second set of experiments was performed with a detector containing a smaller diameter crystal. The detector energy resolution is an inverse function of the crystal diameter and the inferior resolution of the second detector used can be seen in figure 2.5. The resolution of the second detector was 0.66 keV (1.1%). The resolution for a NaI(Th) detector at the same energy is about 6-7%. The reason this peak was used to find the energy resolution is because the experiments that were carried out were done using the 57.97keV $K_{\alpha 2}$ peak from tungsten. This is very close in energy to the Am-241 peak at 59.54 keV and so the resolution will be approximately the same.

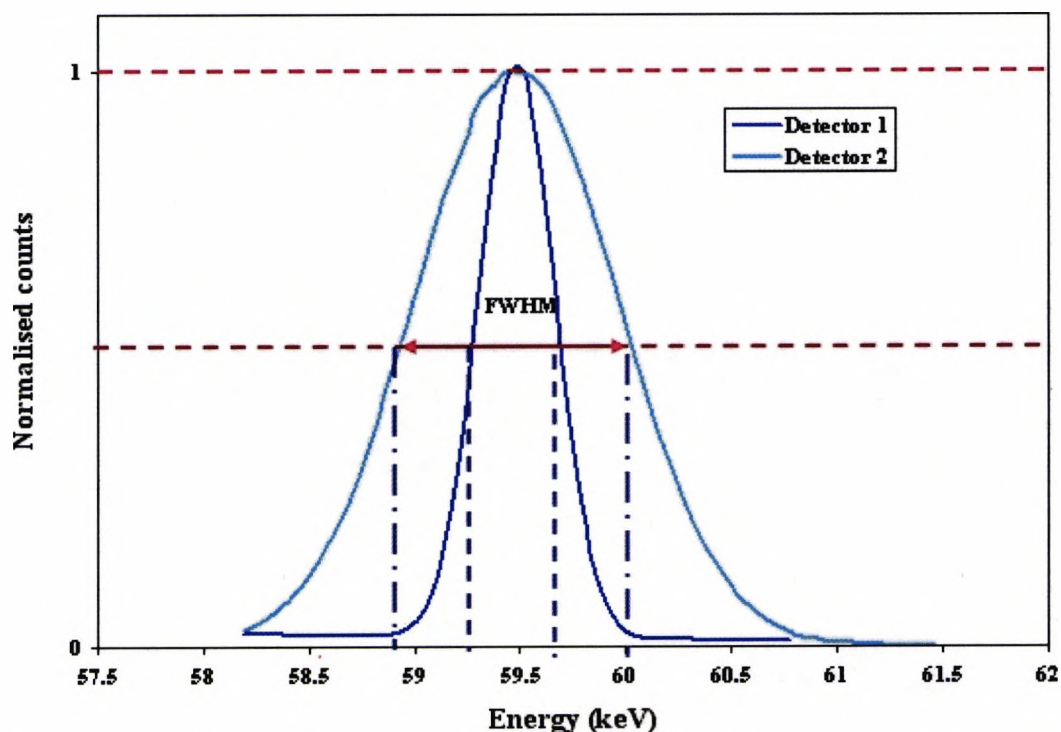


Figure 2.5 The FWHM of the 59.54 keV peak of Am-241 for both detectors used in the laboratory

2.2.4 Single Channel Analyser (SCA) energy calibration

In order to calibrate the channel numbers of the SCA to the correct energy a calibration curve was needed. This was produced by recording the spectrum from an Americium-241 source. The SCA was scanned through each channel and the output was recorded. The maximum reading corresponding to each of the peaks in the Am-241 spectrum were found and plotted against the peak energy, as shown in figure 2.6. The known energies of the Am-241 peaks can then be assigned to the appropriate channel numbers. This was repeated regularly during the experiments.

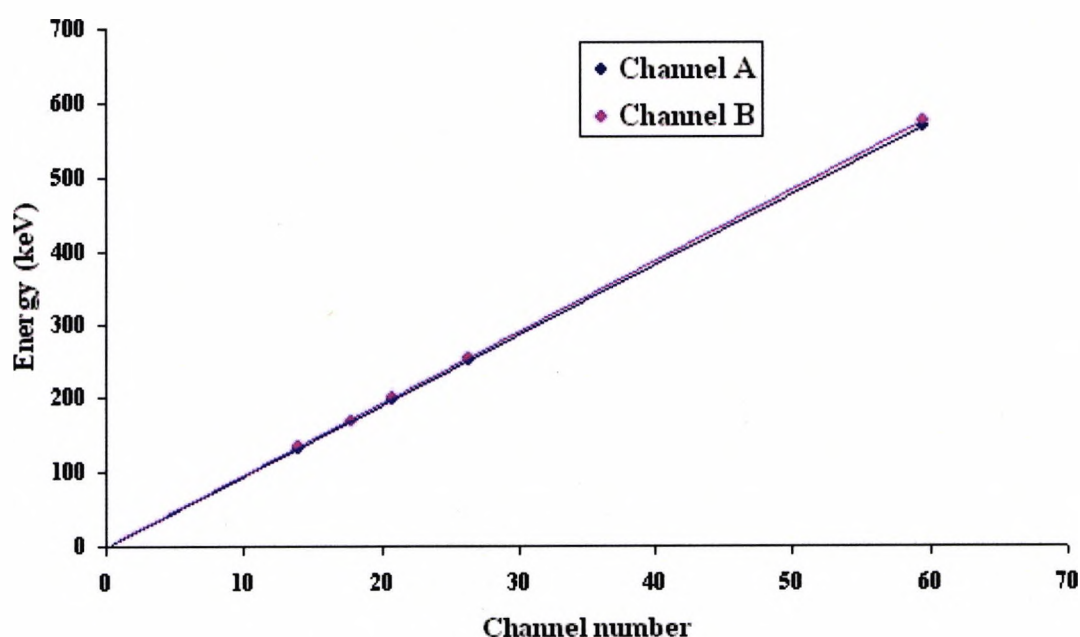


Figure 2.6 Energy calibration graph

Each single channel analyser showed a slightly different response and so they were calibrated individually. The calibration equations are as follows:

$$\text{Channel A: Energy (keV)} = 9.5442 \times \text{Channel number} - 1.3648 \quad [2.1]$$

$$\text{Channel B: Energy (keV)} = 9.6786 \times \text{Channel number} - 1.2842 \quad [2.2]$$

These equations were then used to correctly window the counters. A window width of 1 keV was chosen, from 56.1 keV to 57.1 keV, which corresponded to 10 channels.

2.2.5 Multi Channel Analyser (MCA) energy calibration

In order for the data recorded by the Maestro software (EG&G Ortec) to have the correct energy calibration the program allows a simple energy calibration to be performed using an Americium-241 source. The spectrum recorded after counting with the MCA for 30 minutes is given in figure 2.7. The channel numbers are then assigned to the correct energies using the inbuilt software calibration procedure.

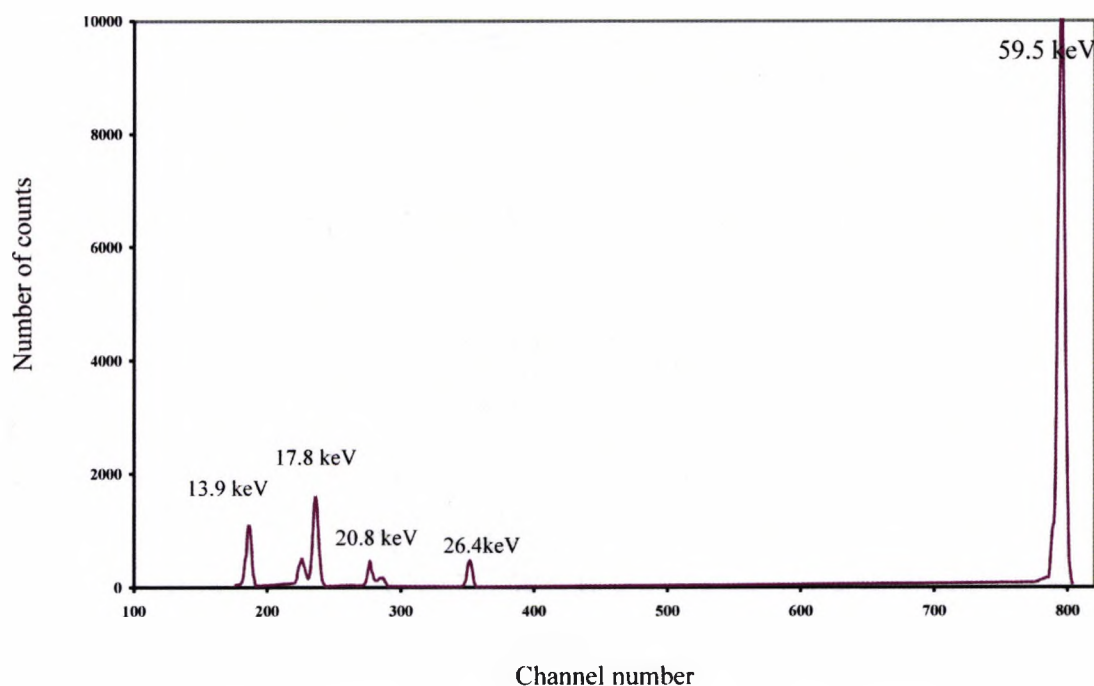


Figure 2.7 Americium-241 spectrum used to calibrate the MCA

2.2.6 Visual basic program

This program was designed to perform two functions, firstly to allow control of the counting electronics and secondly to facilitate automatic data collection. With this software the data could easily be transferred to a spreadsheet for analysis. The program is outlined in detail in Appendix 1.

2.3 Synchrotron experimental set-up

2.3.1 Daresbury synchrotron

2.3.1.1 Introduction

Some x-ray diffraction work was carried out at the Daresbury Synchrotron Radiation Source (SRS). This is a synchrotron with a 2GeV storage ring, operating at between 150 and 250mA. The beamline used was Station 16.3. This beamline operates at between 5 and 30 keV and is used for anomalous diffraction experiments, as well as magnetic scattering, strain scanning and topography.

2.3.1.2 Experimental equipment

The beamline has a 5-axis goniometer. This is a specialised piece of equipment, which allows a detector to be mounted onto a mobile arm. This arm can then be translated and rotated. All rotation is accurately centred about a single point with an accuracy of the order of microns. The sample is held by a sample holder which can be independently positioned. The sample can also be translated and rotated. An HPGe detector was mounted onto the goniometer 2-theta arm and positioned about 1m from the sample. Two sets of collimators positioned post sample define the scattered beam hitting the sample. The sample is aligned using a CCD camera and an optical telescope positioned so that the sight crosshairs are positioned on the axis of the beam.

2.3.2 ESRF Synchrotron

2.3.2.1 Introduction

Further experimental beam time was obtained at the European Synchrotron Radiation Facility (ESRF) in Grenoble, France. The synchrotron has a storage ring that circulates electrons at 6GeV and 200mA and the storage ring is 850m in circumference. The beamline used was BM28, the XMaS beamline, which is a facility specifically designed for diffraction experiments. The main work carried out on this beamline is magnetic scattering studies (XMaS stands for X-ray Magnetic Scattering)

as well as material surface and thin film analysis. The beam can be tuned up to an energy of 15keV, with the ability to easily collimate the beam to a very small size. A high flux allows for good counting statistics and short measurement times. The energy of the beam is selected by a double crystal monochromator. This is tuneable to energies of 2 to 16 keV, although the flux begins to drop off at energies above 15 keV, as shown in figure 2.8

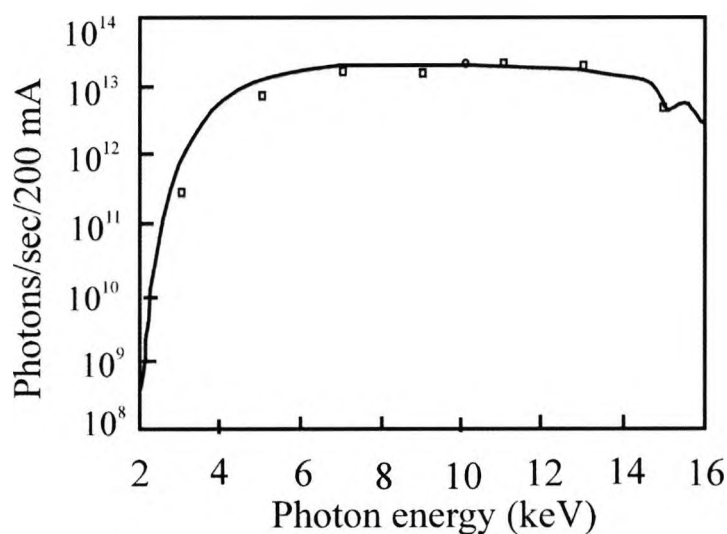
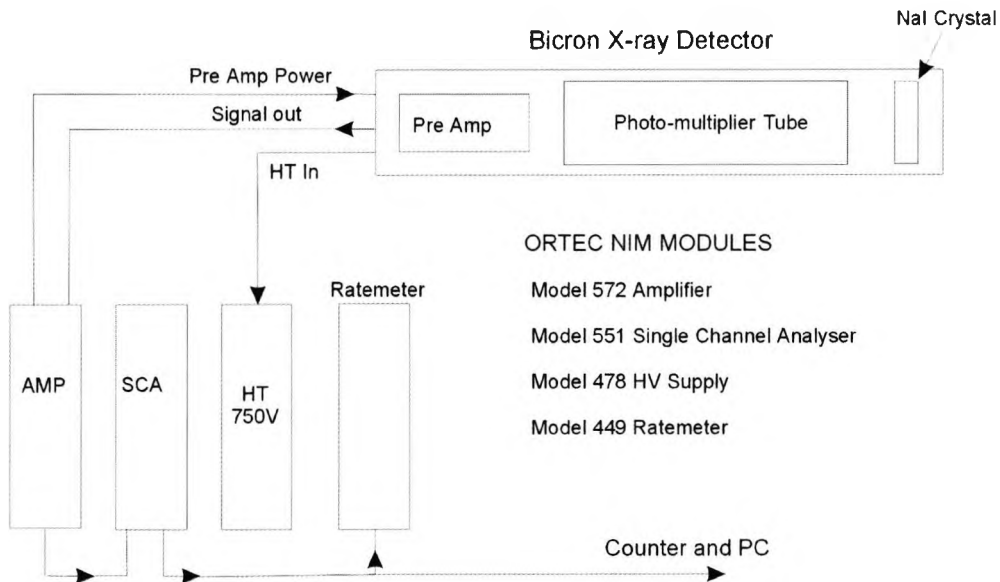


Figure 2.8 The flux of the BM28 as a function of monochromatic beam energy
(Brown et al. 2001)

2.3.2.2 Experimental Equipment

The beam is equipped with an 11-axis Huber diffractometer, similar to the one used at Daresbury. An evacuated tube was fitted between the sample and the detector to collimate the post sample beam. This reduces background scatter and allows for very precise collimation close to the sample. The tube houses a set of four slit collimators along its length, two sets in the x-direction and two sets in the y direction. The detector used was a Bicron NaI scintillation detector. This consists of a NaI crystal coupled to a photomultiplier tube (PMT). The PMT is connected to a pre-amplifier, which is in turn connected to an amplifier and a single channel analyser (SCA). This configuration is shown in figure 2.9. SPEC software was used to record the counts from a counter card connected to the SCA.



*Figure 2.9 The electronics chain used at the ESRF
(European Synchrotron Radiation Facility 2004)*

2.3.2.3 Beam alignment

There is a focussing mirror after the monochromating crystals to facilitate a high photon flux with a small beam size. Tuning the monochromator causes a shift in the beam position. The beam must therefore be easily realigned, and this is done with the second crystal within the monochromator system. The crystal is controlled by a set of precision motors. Radiation sensitive paper is used to determine the position of the beam at the Huber centre of rotation and the beam position can then be altered until it is aligned with the rotational centre.

2.4 Sample preparation

2.4.1 Tissue storage and preparation

For the first set of experiments, which consisted of scatter measurements performed at the Daresbury synchrotron and the first measurements in the laboratory, four different broad classifications of tissue were examined. These were collected from 22 patients. A portion of each section was classified by a histopathologist. The tissue types consist of fibroadenoma, fibrocystic change (FCC), malignant and adipose. Due to difficulties involved in tissue collection the tissues were of short supply. Therefore each frozen section was divided into two and these were treated as independent samples.

For the second set of experiments, which are the second set of laboratory experiments and those performed at the ESRF synchrotron, a further 50 samples were measured taken from 42 patients. These were of the same tissue classifications as the first set but with normal fibrous tissue also included.

All tissues were snap frozen during surgery and then stored at a temperature of -80°C . Before measurements were made they were defrosted to room temperature. The adipose tissue is pure fatty tissue collected during breast reduction surgery from non-diseased breasts. The other tissues were removed during breast cancer surgery. The normal fibrous tissues were taken from patients that were having a lumpectomy but at a distance from the site of the malignancy. These were not paired to the malignant tissues used in this study.

2.4.2 Sample holders

The samples were placed in holders so that they could be placed in the experimental system. The first set of measurements was performed at the Daresbury SRS. An initial design of sample holder was used which was then redesigned for the measurements in the laboratory. For this initial design the samples were placed in PMMA slides which were 2mm thick with a 6mm hole drilled out of the centre. The samples were placed in the hole and then sliced on each side so that the samples were 2mm thick. Each side

of the sample holder was sealed with 6 μ m mylar film. This design is illustrated in figure 2.10.

The experiments in the laboratory were performed in two separate sets of measurements. Each time the system was calibrated and so the two measurement sets could be combined. Between the two experimental sessions the design of the container holding the samples was revised. The problem with the initial sample holder was the geometry. The cross section of the plane that the beam was intersecting was essentially a rectangle. In order to simplify the data correction process this plane needed to be cylindrical. The sample holders were redesigned with this in mind.

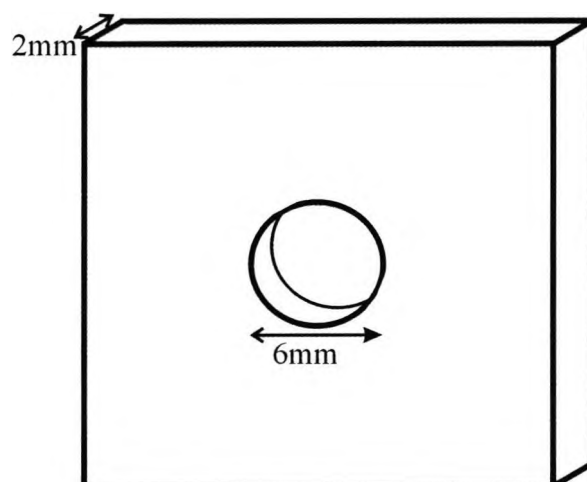


Figure 2.10 Slide sample holder used at the Daresbury SRS synchrotron

The second design consisted of simple polyethylene vials of 6mm inside diameter and 1mm wall thickness. Although the walls of the container were relatively thick and would cause significant attenuation of the scattered beam, these containers were chosen because they offered a number of important advantages: The sides were completely rigid so the samples could be placed into the pots and lightly compressed with a stopper to remove any air gaps without the pot becoming distorted. This also minimised tissue movement throughout the experiment. The samples also needed to be symmetrical about a centre of rotation in order for the attenuation correction to be straight forward. An illustration of these sample holders is given in figure 2.11.

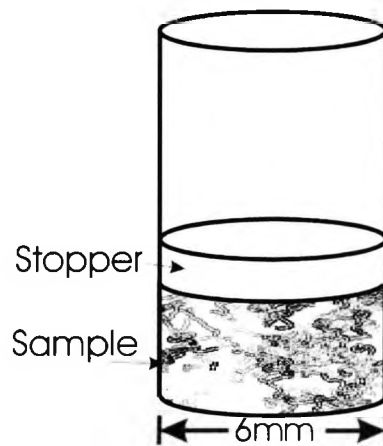


Figure 2.11 Sample holder for the second set of experiments

For the third set of experiments a design was sought which would eliminate most of the attenuation due to the surrounding plastic. This was an important issue mainly because the tissues were to be measured at the synchrotron source at a much lower energy than in the laboratory, and so the attenuation by the sample would be much greater and much more significant. Once the samples had been measured at the synchrotron the measurements were repeated in the laboratory on the same samples in the same holders with a similar alignment to allow a comparison of the two experimental environments. The third set of sample holders were manufactured from polyethylene tubes with a hole machined out of them for the entrance beam and a groove machined for the exit beam. The samples were wrapped in $6\mu\text{m}$ mylar film and sealed with superglue before being inserted into the tube and the secured at each end of the tube with a rubber stopper. The advantage of the incident and scattered beam only passing through two mylar windows rather than plastic was offset by the loss of rigidity of the sample holder. The windowed sections meant that it was harder to ensure that the sample was of a uniform cross section over the measurement volume plane as the film is liable to bulge at the window areas. Also the calibration solutions were difficult to prepare whilst ensuring that the liquid volume was not bulging at the windowed areas.

2.5 Summary

A system was designed and constructed for measuring the scatter signal from breast tissue samples. In the laboratory the alignment of the system was optimised using an ionisation chamber. The energy resolution of each detector used was measured and the system was calibrated using an Americium-241 sealed source. A description of the equipment used at the Daresbury and ESRF synchrotrons has been given.

Three different designs of tissue sample holders were used, with the design being improved with each subsequent configuration, so that the amount of corrections needing to be applied to the data was reduced.

Chapter 3 Electron density measurement

3.1 Introduction

Dr. Otto Warburg first observed in 1930 that cancer cells have a fundamentally different energy metabolism than normal cells (Warberg 1930). Since then research has shown that tumour cells undergo anaerobic glycolysis, the process where glucose is converted to lactic acid through the process of fermentation. This process is extremely inefficient compared to normal cell aerobic respiration. Glucose consumption rate has been shown to be proportional to histological grade (Vaupel *et al.* 1989) and high grade tumours can absorb about 40 times more glucose in order to supply their high energy demands for increased growth. This process is what makes positron emission tomography (PET) imaging so effective at imaging tumours using ^{18}F -FDG, an analogue of glucose. It enables PET to distinguish between benign and malignant neoplasms with a high degree of accuracy, as benign tissues do not exhibit increased glucose consumption (Brock *et al.* 1997). Anaerobic glycolysis causes a build up of lactic acid to occur within the tissue. The lactic acid ($\text{CH}_3\text{-CH}(\text{OH})\text{-CO}(\text{OH})$) which builds up within the tumour has a high electron density compared to the host tissue of 8.2×10^{23} electrons/cm³ and so could cause a measurable increase in electron density. There is also an increase of ketones and glutamine (Vaupel *et al.* 1989), which may also increase the overall electron density of tumour tissues. Although no direct measurements have been made of the composition of benign and malignant tissues, the above suggests that there are significant differences in composition. It is difficult to estimate the precise nature of the composition changes, given that there are a number of processes occurring in the tissue during tumourgenesis. This study has been interested in establishing whether these differences produce a measurable variation in the tissue structure and/or composition, and hence the concentration of electrons.

The aim of these experiments was to determine the electron density of five classifications of breast tissue and to assess whether the measurement of electron density using Compton scattered photons is an effective way of distinguishing

between breast tissue types. The electron density was determined by constructing a calibration model using substances prepared in the laboratory with an electron density that could easily be calculated.

The experiments were performed in the laboratory with a conventional x-ray source on two different sets of tissues. One of these tissue sets was also brought to a synchrotron source where the experiments were repeated on the same area of the tissue samples under different measurement conditions. The high flux and monochromaticity of the synchrotron source make it the ideal facility for making these measurements.

Section 3.2 describes the theory and rationale behind the electron density measurements. Section 3.3 outlines the experimental methods used, both in the laboratory and at the synchrotron. The system calibration method and results are presented in section 3.4 with a summary of the experimental work given in section 3.5. The results are presented in Chapter 4.

3.2 Theory

The relevant experimental parameters for the two measurement systems used are given in the following table

| Experiment | Energy (keV) | Angle (degrees) | Momentum transfer (nm^{-1}) | Klein-Nishina cross section ($\text{cm}^2/\text{electron}$) |
|-------------|--------------|-----------------|--|---|
| Laboratory | 58 | 30 | 12.1 | 5.206×10^{-26} |
| Synchrotron | 13 | 112 | 8.9 | 7.082×10^{-26} |

Table 3.1 The experimental parameters used for the electron density measurements

The momentum transfer was calculated using equation 1.13 and the Klein-Nishina (KN) cross section was calculated using equation 1.9 and is the probability that a photon is incoherently scattered by an electron within an atom. At these momentum

transfer values the binding energy of the atom has a significant effect and cannot be ignored. To take this into account the KN cross section must be reduced by the Incoherent Scattering factor $S(\bar{x})$, as explained in section 1.3.4.2. In this section the incoherent scattering coefficient, σ_{inc} , was given in equation 1.19, but is reproduced here for clarity:

$$\sigma_{inc}(\bar{x}, Z) = \rho N_A \frac{d\sigma_{KN}}{d\Omega} \frac{S(\bar{x}, Z)}{M} \quad [1.19]$$

and is the probability that a photon will be Compton scattered when interacting with a material of density ρ and molecular mass M . N_A is Avogadro's constant. As stated in section 1.3.4.2 the incoherent scattering function $S(\bar{x}, Z)$ is a corrective factor, needed to account for the effect of the electron binding energy on the KN cross section. Hubbell *et al* (1975) have extensively tabulated the values of S for all elements of the periodic table, and much work has gone into the theoretical calculation of S values (Waller and Hartree 1929; Viegele *et al* 1966).

For the analysis of this experiment an empirical equation of the simplest form has been found to quantify the Z dependency of the values of $S(Z)$ given by (Hubbell *et al.* 1975) for a fixed value of \bar{x} . Figure 3.1 shows the results obtained by plotting the values of $S(Z)$ for $\bar{x}=12.1\text{nm}^{-1}$ and $\bar{x}=8.9\text{nm}^{-1}$ over the range of Z values relevant to this work ($Z=1-20$).

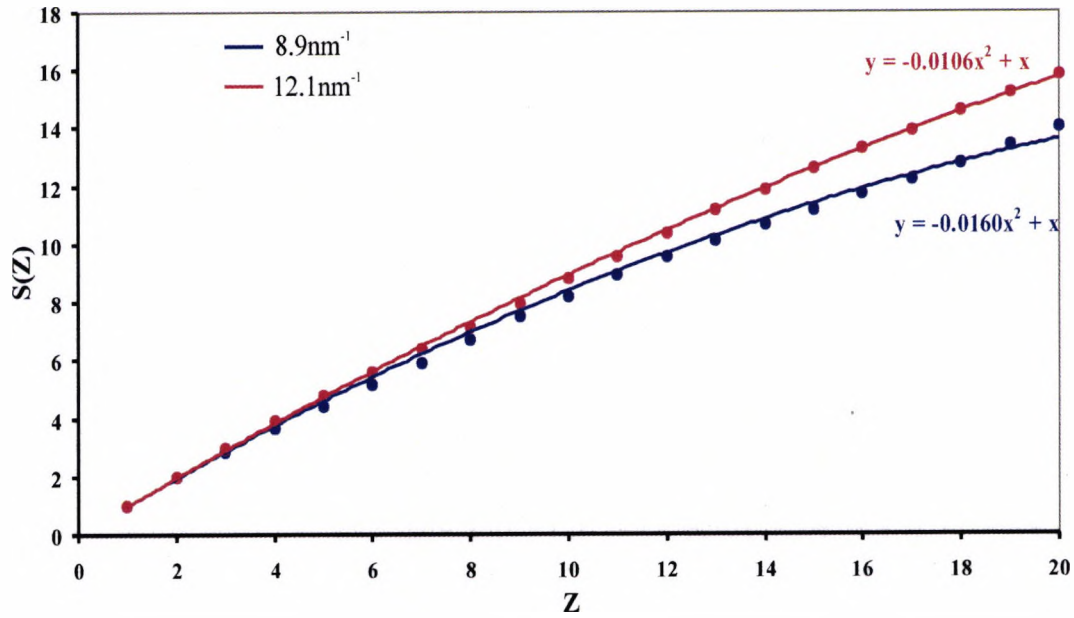


Figure 3.1 A graph plotting $S(Z)$ values

From figure 3.1 it can be seen that:

$$S(Z) = Z - k_1 Z^2 \quad [3.1]$$

where k_1 is an empirical constant, dependent on Z . This approximation is only valid for the specified momentum transfer value and the range of Z values used here. Substituting this relationship into equation 1.19 gives:

$$\sigma_{inc}(Z) = \rho N_A \frac{d\sigma_{KN}}{d\Omega} \frac{(Z - k_1 Z^2)}{M} \quad [3.2]$$

The electron density, ρ_{e^-} , for a material Z is given as:

$$\rho_{e^-} = \frac{\rho N_A Z}{M} \quad [3.3]$$

Rearranging this relationship and substituting into equation 3.2 gives:

$$\sigma_{inc}(Z) = \frac{d\sigma_{KN}}{d\Omega} (\rho_{e^-} - k_2 \rho_{e^-}^2) \quad [3.4]$$

where k_2 is a constant equal to $\frac{Mk_1}{\rho N_A}$. This can be considered to be constant as $\frac{M}{\rho}$ varies slowly over the values of interest, and is approximately equal to 14.3. This value changes by 2.2% for the calibration solutions used in this work. A table of $\frac{M}{\rho}$ values for each calibration solution is given below:

| Substance | M/ ρ |
|--------------|-----------|
| Water | 14.3 |
| 2% solution | 14.5 |
| 5% solution | 14.5 |
| 10% solution | 14.2 |

Table 3.2 M/ ρ values for the calibration solutions

The corrected counts, S_{corr} , measured during the Compton scatter experiments can be plotted against the incoherent scattering coefficients, σ_{inc} , where:

$$\sigma_{inc} = \frac{1}{N_0} [S_{corr}] \quad [3.5]$$

N_0 is the number of counts incident on the sample. S_{corr} is counts measured in the Compton scatter peak, corrected for attenuation, and is given by:

$$S_{corr} = \frac{[S_{meas} - B_s]}{A_f} \quad [3.6]$$

where S_{meas} is the number of counts, B_s is the background counts and A_f is an attenuation correction factor.

The electron densities of the calibration solutions are calculated using equation 3.3. As the substances being used are not mono-molecular the ratio of atomic mass to atomic weight, Z/M , must be replaced by the sum rule:

$$\frac{Z}{M} = \sum \frac{Z_i}{A_i} \omega_i \quad [3.7]$$

where Z_i/A_i is the ratio of atomic number to atomic weight for the i^{th} element of mass fraction ω_i . Z/A values were taken from (Attix 1986).

The intensity of the scattered signal must be corrected for the attenuation of the beam due to the sample. As the attenuation coefficients of the tissue samples are not known and cannot be calculated they must be measured experimentally.

Consider the cylindrical geometry shown in figure 3.2. A beam of photons is in the direction AB with energy E_1 and a detector is placed at a scatter angle θ to the incident beam.

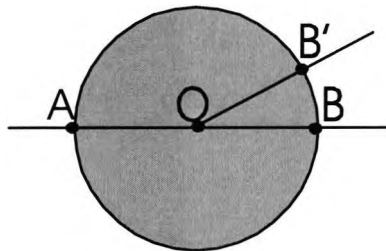


Figure 3.2 Cylindrical geometry of the sample holder

The number of scattered photons, S , with energy E_2 reaching the detector is reduced by a proportion due to the attenuation of the beam, given by:

$$S \propto \exp\left(-\int_A^O \mu_1(x) dx\right) \exp\left(-\int_O^{B'} \mu_2(x) dx\right) \quad [3.8]$$

where μ_1 is the attenuation coefficient of photons at the incident energy, and μ_2 is the attenuation coefficient of the Compton photons, scattered through angle θ with reduced energy E_2 . If the incident energy E_1 and scatter angle θ are carefully chosen it can be assumed that $E_1 \approx E_2$ and therefore that $\mu_1 \approx \mu_2$. Using these assumptions it follows that

$$\exp\left(-\int_A^B \mu_1(x)dx\right)\exp\left(-\int_B^C \mu_2(x)dx\right) \approx \exp\left(-\int_A^C \mu_1(x)dx\right) \quad [3.9]$$

and equation (2) becomes

$$S \propto \exp\left(-\int_A^B \mu_1(x)dx\right) \quad [3.10]$$

From the exponential law of attenuation it is found that

$$\frac{I}{I_0} = \exp\left(-\int \mu_1(x)dx\right) \quad [3.11]$$

where I_0 is the incident photon intensity and I is the transmitted photon intensity. Using these assumptions it follows that for a cylindrical (circular cross section) sample the attenuation factor, A_f is equal to:

$$A_f = \frac{I}{I_0} = \exp\left(-\int_0^D \mu(x)dx\right) \quad [3.12]$$

where I_0 is the incident photon intensity, I is the transmitted photon intensity, x is the thickness and D is the diameter of the sample. Applying these assumptions enables an attenuation correction to be measured for each individual sample, this being the attenuation along a straight path through the centre of the sample.

Using XCOM (Berger and Hubbell 1998) data to assess the error produced by this method has shown that for water the difference in I/I_0 is $<0.1\%$ and for the most attenuating calibration solution the difference is $<0.25\%$

3.3 Method

3.3.1 Laboratory measurements

3.3.1.1 Introduction

Ideally a monoenergetic source should be used so that the Compton scatter peak is easily detectable. The characteristic lines produced by the x-ray tube were used to generate a pseudo-monoenergetic source. Using this method the Compton and Coherent peaks can be easily resolved and windowed. The bremsstrahlung background can then be subtracted.

The desired outcome from the experiment was to be able to resolve the Compton and coherent peaks, whilst keeping them as close in energy as possible. The detector characteristics dictate that the minimum resolvable energy is about 0.8 keV.

3.3.1.2 Experimental set-up

The Compton scatter equation (1.6) was used to calculate the angle required to give an appropriate difference in energy between the incident and scattered peaks. To obtain $E_1 - E_2 \cong 0.8$ keV, there was a choice between either using a higher energy and a small scattering angle or a lower energy with a larger scattering angle. Both of these options were explored and the conclusion was that using a higher energy and minimising the angle offered a number of advantages. Firstly the attenuation of the beam by tissue will be lower with a higher energy. Secondly the scatter is at a maximum in the forward direction and at a minimum at 90° . Therefore the flux reaching the detector will be much higher with a smaller angle, reducing count times. A smaller beam size can also be used, improving the geometry of the measurement.

The distance between the source, sample and detector were kept to a minimum to decrease the loss of flux due to inverse square law effects. The experimental set-up is shown in figure 3.3.

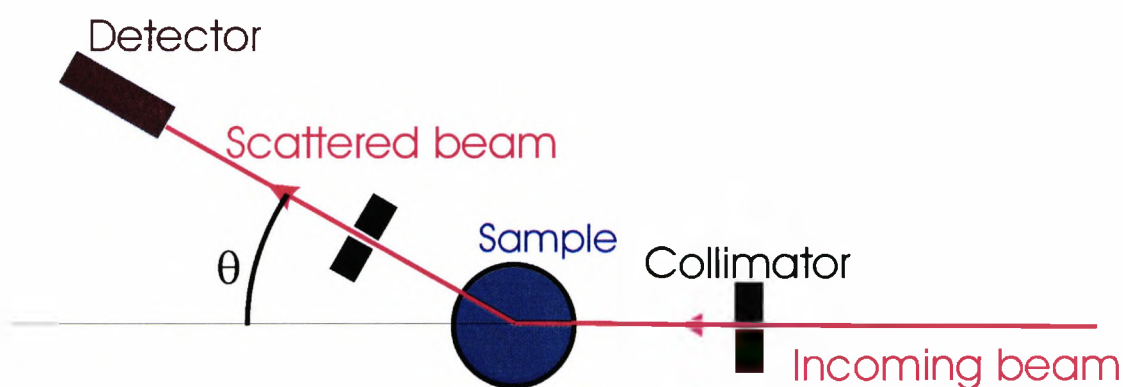


Figure 3.3 Experimental set-up for scatter measurements

The x-ray beam was collimated to 0.5mm diameter, both before and after the sample. This was the smallest beam size viable whilst maintaining a reasonable photon flux. The $K_{\alpha 2}$ line from the tungsten target of the x-ray source ($E_{K_{\alpha 2}}=57.97$ keV) was used. At this energy a scattering angle of 30° gave a peak separation of 0.7 keV between the Compton and coherent scatter peaks. The scattering volume is defined as the region of intersection of the collimated incident pencil beam and the collimated angular acceptance to the detector.

3.3.1.3 Scatter measurements

The scatter volume is contained within the sample and does not extend into the sample holder or surrounding air. It is Compton scattering from electrons within this volume that reach the detector at the measured energy and contribute to signal. Any scatter outside this volume reaching the detector is regarded as noise. Each sample was measured for a total time of four hours, with the sample being rotated throughout the measurement in order to reduce any effects due to the inhomogeneity of the tissues. This measurement time was chosen to reduce the statistical error of counting to below 0.5%.

An example of an observed scatter spectrum is shown in figure 3.4. The two coherent peaks of the $K_{\alpha 1}$ and $K_{\alpha 2}$ W lines and the two Compton scatter peaks can be seen.

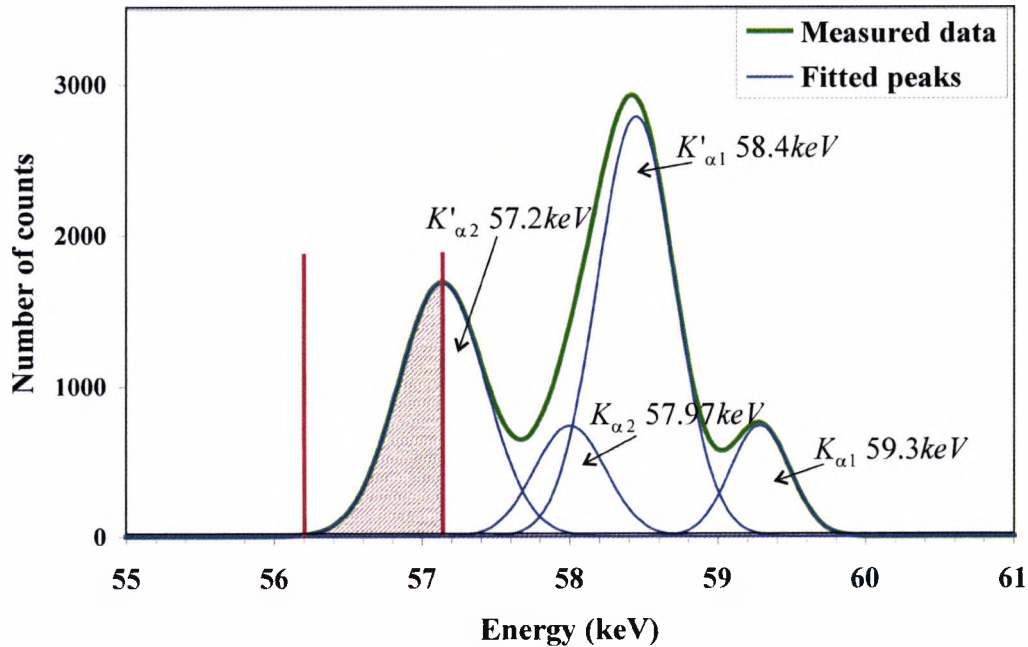


Figure 3.4 Single Channel Analyser windowed area

The $K_{\alpha 2}$ Compton peak was measured for this experiment. This is because the $K_{\alpha 1}$ peak, although it has a stronger signal, is significantly overlapped by the two coherent peaks. The first half of the $K_{\alpha 2}$ peak was windowed so that the counts under this area were integrated. This is illustrated by the red hatched area in the diagram. The background counts were subtracted from these counts. This method was chosen to give an accurate peak count unaffected by any other peaks present.

In order to subtract the background (bremsstrahlung) spectra the counts from two channels were recorded, one above the peaks of interest (60keV) and one below (56keV). The straight line joining these two points was found using the straight line equation. The counts below this line within the windowed area were then subtracted from the total number of counts.

3.3.1.4 Transmission measurements

The transmission measurements are a measure of the reduction in intensity of the unscattered peak and is a measure of the loss of counts due to tissue attenuation. For these measurements the detector was placed at zero degrees. This means that the count flux was much higher than during the scatter measurements. Therefore the detector was moved further away and the count times were shortened. A small amount of copper (0.5mm) was placed in the beam to protect the detector from the high flux

The set-up is shown in figure 3.5

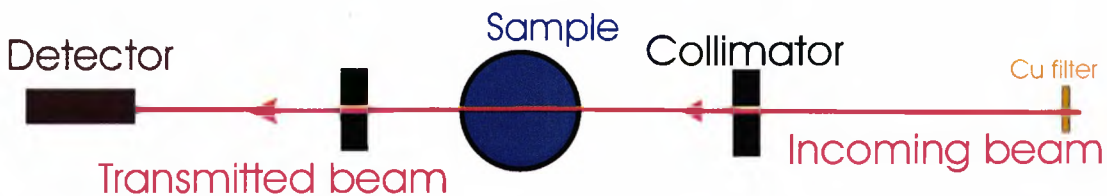


Figure 3.5 The transmission measurement set-up

One Single Channel Analyser (SCA) window was changed to detect the transmitted peak and the other was set to record a background area. This area was set as 10 channels directly below the $K_{\alpha 2}$ peak. The peak SCA window was set to record the counts under the whole $K_{\alpha 2}$ transmitted peak, as there are no problems with overlapping peak areas. The peak areas chosen are shown in figure 3.6 below.

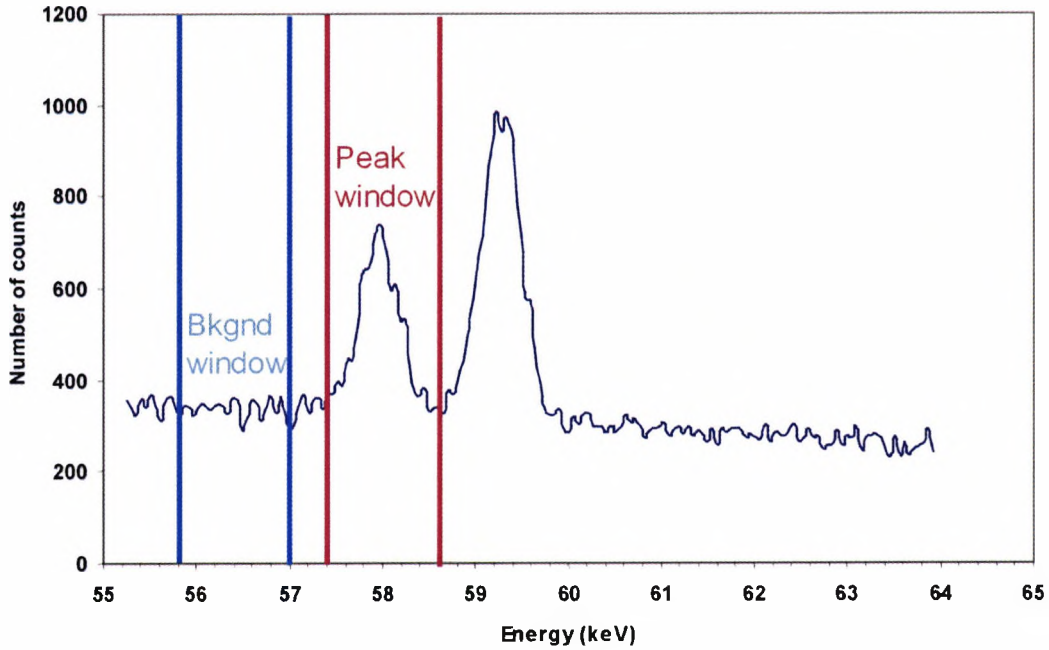


Figure 3.6 The windowed areas chosen for the transmission measurements

The counts were recorded for 300 seconds at each rotation and were rotated 12 times. The count time for each sample was 1 hour. The beam collimation was identical to the collimation for the scatter measurements, with 0.5mm circle collimators both before and after the sample. A reading was also made with no sample present to give the unattenuated count intensity I_0 .

3.3.2 Synchrotron measurements

3.3.2.1 Introduction

The aim of repeating the measurements at the synchrotron was to verify the repeatability of the measurements using a separate experimental set-up and to establish whether the laboratory experiments could be improved upon using an inherently better experimental system. The experiments were performed at the European synchrotron radiation facility (ESRF) over 72 hours of beamtime.

3.3.2.2 Experimental set up

The equipment used for the experiments was outlined in section 2.3.2. The source was tuned to an energy of 13keV, which is the maximum energy achievable on this beamline without any loss of flux. The sample was mounted at the centre of rotation of a moveable arm on which the detector was mounted. The beam was collimated to a size of 0.8mm x 0.8mm square at the surface of the sample. A set of vacuum slits were used to reduce the loss of signal flux due to attenuation by air between the sample and detector.

3.3.2.3. Scatter measurements

The angle of the detector was selected so that the Compton and coherent peaks could be easily resolved using a peak fitting software program (PeakFit, SPSS AISN software Inc.). The experiments were made for 20 minutes each in order to achieve good counting statistics well below 0.1%. An example of the scatter spectrum obtained is shown in figure 3.7 below.

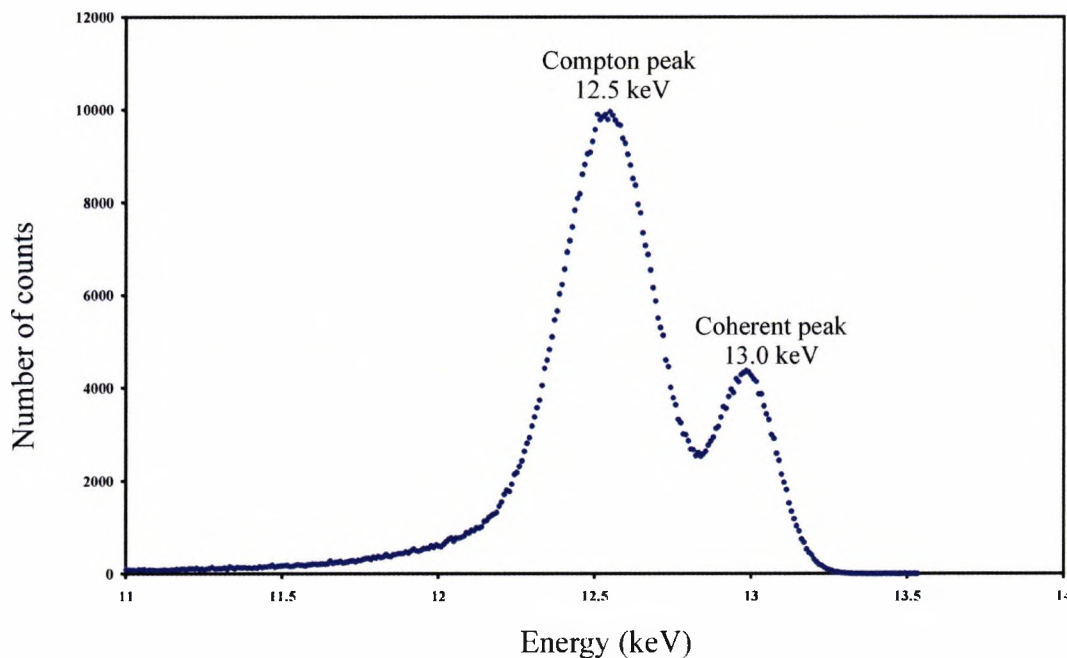


Figure 3.7 A synchrotron scatter spectrum

As the energy of the beam is monochromatic there is no background bremsstrahlung spectrum to be subtracted. The entire spectrum at 112° was recorded with the energy dispersive detector and saved.

The sample holder used in the first set of experiments in the laboratory was redesigned to be suitable for use in the low energy set-up of the synchrotron. These sample holders were then also used in the laboratory to repeat the measurements. The samples are therefore identical to the ones used in the second set of laboratory measurements and have been described in detail in section 2.4.2. Care was taken to ensure that each sample was correctly aligned with the mylar window positioned over the beam. This was done by burning a piece of radiation sensitive paper over the sample holder and checking the position of the beam before the measurement was carried out.

3.3.2.4 Data correction

The beam flux decreases with time after the storage ring has been filled with a new injection of electrons. This means that the scatter signal must be normalised to the flux of the incident beam. To allow this a scintillation counter is positioned at 90° to the incident beam with a scattering foil in the beam. The number of counts detected by the scintillation counter is proportional to the beam flux and so provides a measure of the beam flux. The scatter signal is then normalised to this scintillation count. The count, however, is only recorded for 40 seconds at the beginning of the measurement. In order to ensure the most accurate signal normalisation possible a graph was constructed of the number of counts per second recorded by the scintillation counter against the time since a refill was performed. A function was then empirically fitted to this graph. For each scan the time since last refill is recorded in the data file at the end of each measurement. This time was used to find the number of counts incident on the sample by integrating the area under the curve, using the start and finish times as limits of integration. This graph is shown in figure 3.8.

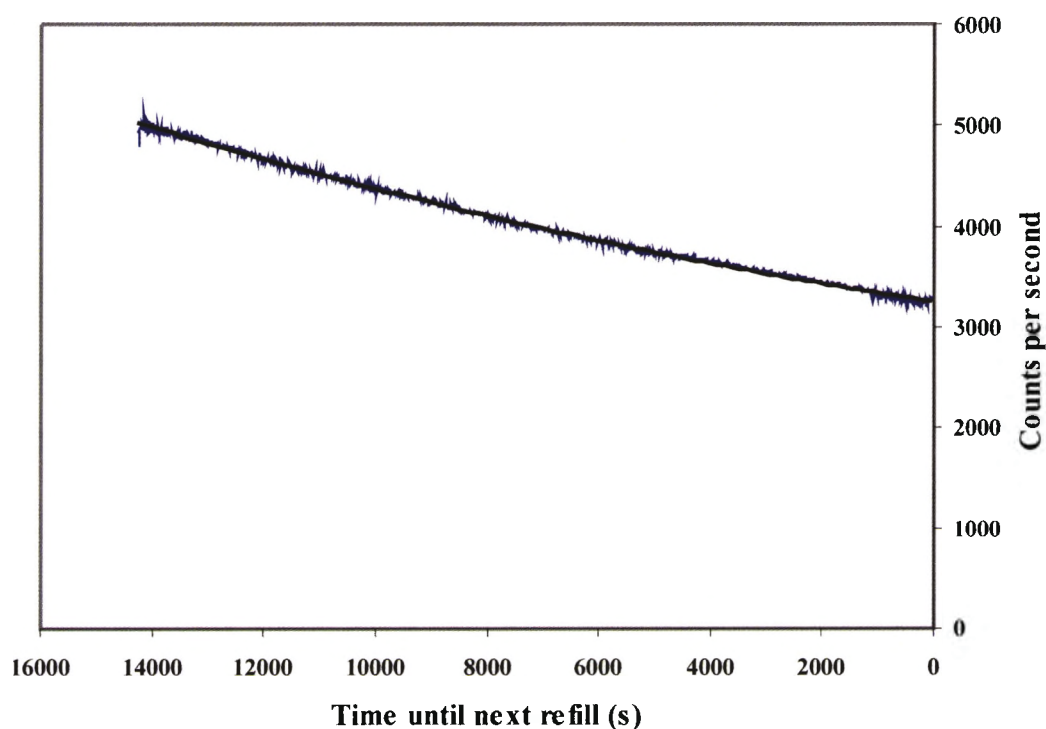


Figure 3.8 A graph of the number of counts incident on the sample against time after refill

A polynomial was empirically fitted to the curve with an equation of the form

$$y = at^2 + bt + c \quad [3.13]$$

where y is the number of counts per second and t is the time until the next refill. a , b , and c are constants. The area under the curve represents the number of counts incident on the sample between refills, and so equation 3.13 can be integrated to find the number of counts incident on the sample per measurement if the time until the next refill at the start and end of the measurements are used as the limits of integration.

The spectra were peak fitted and then the area of the Compton peak was divided by the normalisation peaks to give a normalised scatter count.

3.3.2.5 Transmission measurements

In order to correct the scatter measurements for sample attenuation transmission measurements were made, in the same manner as with the laboratory measurements. For this purpose the detector was placed at zero degrees. 1.25mm of aluminium was placed into the beam in order to protect the detector from being damaged by the direct beam which was corrected for. Because the beam is so highly monochromatic a spectrum was not recorded but a number of counts with a scintillation detector. The measurements were made at two energies, E_0 (13 keV) and E_1 (12.5 keV). This was to enable accurate calculation of the attenuation of the beam before and after scattering. This is more accurate than the technique used in the laboratory, as the assumption that the incident and scattered beam have the same attenuation coefficient need not be applied. Due to the high flux of the transmission measurements a count time of 5 minutes was sufficient. The data were corrected for attenuation using the transmission measurements as outlined in the previous section.

3.4 System calibration

As the composition of the tissues being measured is unknown, the electron density measurement system needed to be calibrated. This was carried out by measuring substances with a known composition. The solutions chosen were water, iso-propanol, and solutions of potassium hydrogen phosphate K_2HPO_4 . These substances were chosen because they are readily available, easy to handle and have an electron density that is close to that of biological materials. The concentration of the phosphate solutions were varied to provide solutions with differing electron densities. In order to have values close to that of tissue solutions of 2%, 5% and 10% were used.

Iso propanol could not be used as a 5th solution when using the 3rd design of sample holder as the glue sealing the mylar in place was dissolved by the alcohol and so the liquid could not be contained. Due to this fact only 4 calibration solutions were measured during the second laboratory experiments and at the ESRF.

For each of the solutions the incoherent scattering coefficient, σ_{inc} (calculated using equation 1.19), was plotted against corrected scatter counts, S_{corr} (corrected according to equation 3.6). These graphs are shown by Figures 3.9a and b below. Figure 3.9a is the results from the laboratory and figure 3.9b is the results from the ESRF. These graphs demonstrate the relationship given in equation 3.5, reproduced here for clarity:

$$\sigma_{inc} = \frac{1}{N_0} [S_{corr}] \quad [3.5]$$

where N_0 is the number of counts incident on the sample for the laboratory case and counts per monitor unit in the synchrotron case, due to the normalisation procedure performed on the synchrotron measurements.

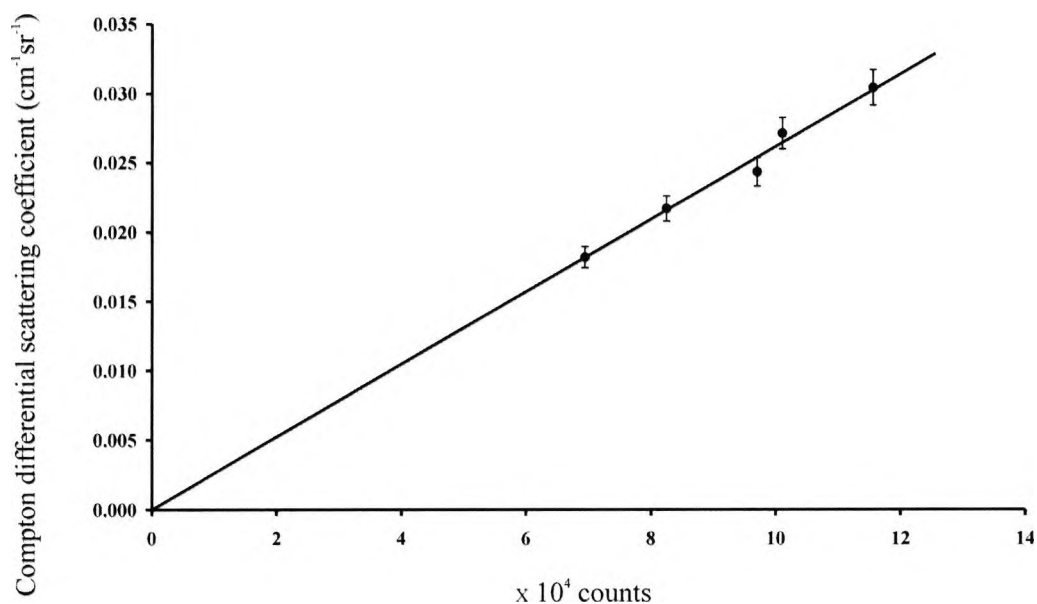


Figure 3.9a Incoherent scattering coefficient against number of counts in the scatter peak for laboratory measurements

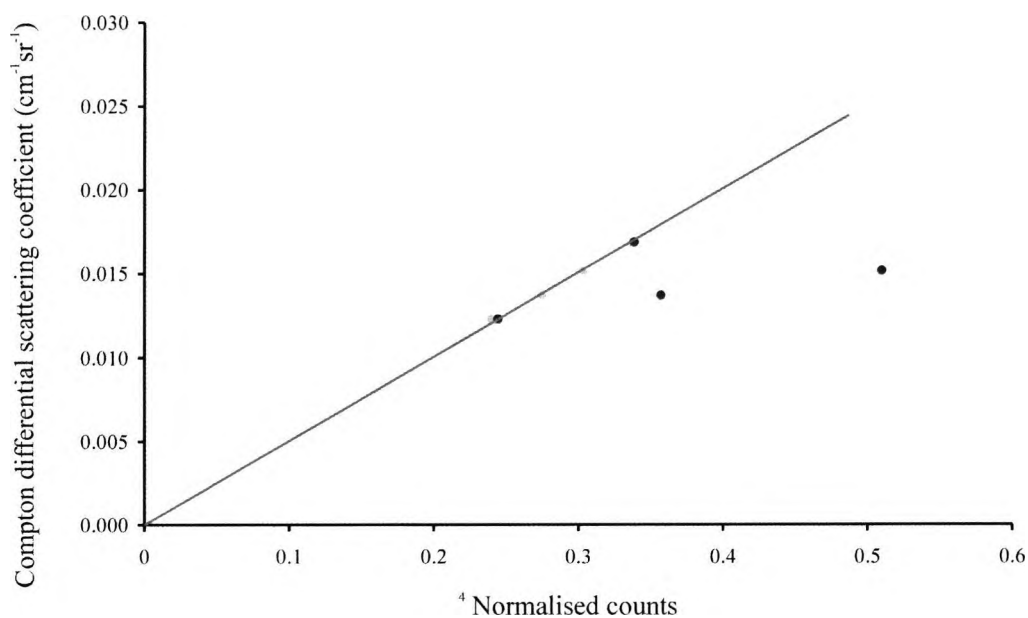


Figure 3.9b Incoherent scattering coefficient against number of counts in the scatter peak for ESRF measurements

Using the graphs in figures 3.9a and b, the incoherent scattering coefficient for each sample was calculated. The electron density, ρ_{e^-} , of each calibration solution (calculated using equation 3.3) was then plotted against the electron density to give a

second calibration curve. These are shown in figures 3.10a and b. Again the laboratory and ESRF results are presented separately.

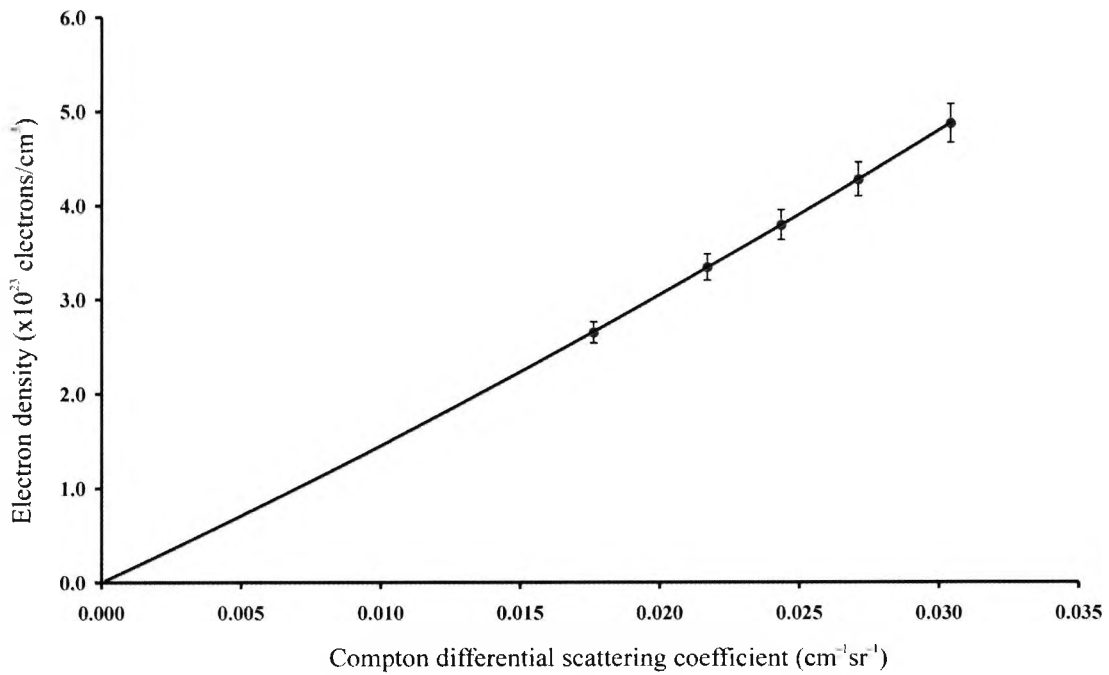


Figure 3.10a Electron density against incoherent scattering coefficient for laboratory measurements

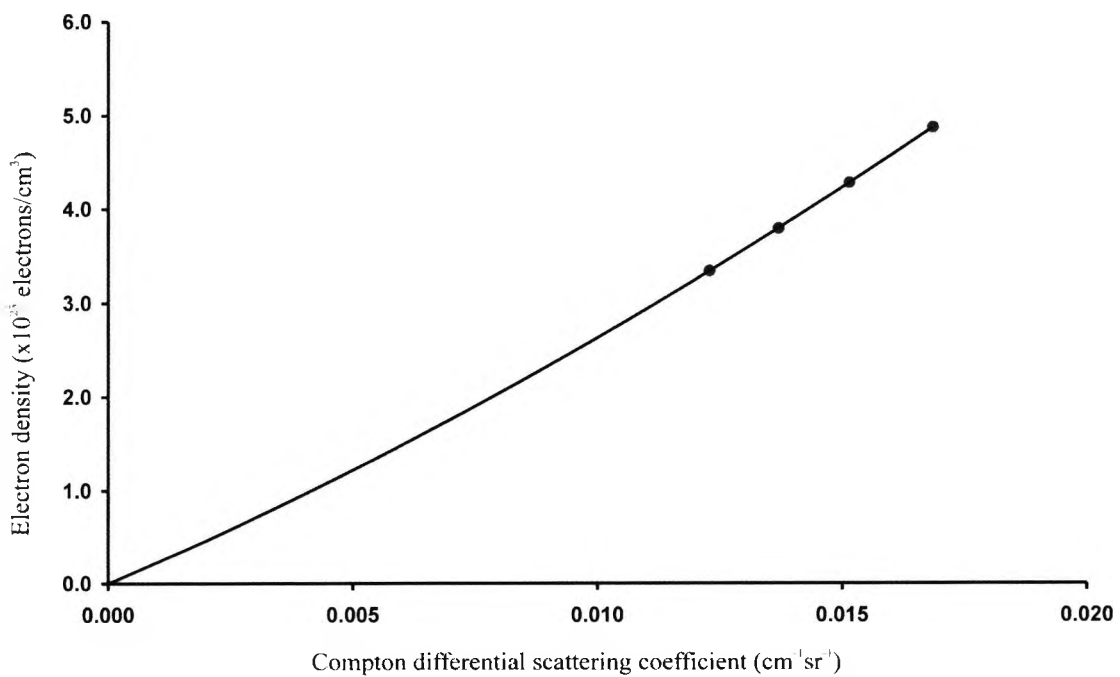


Figure 3.10b Electron density against incoherent scattering coefficient for ESRF measurements

Figures 3.10a and b allow the electron density for each sample to be calculated using the equation of these calibration curves.

Figure 3.9b is the calibration graph from the ESRF synchrotron. In this graph it can be seen that a straight line passes directly through the origin and two points on the graph, but a further two points are seen as outliers. These two data points do not fit along the calibration curve and have been omitted from the calibration model. The reason that these two points lie so far from the curve can only be explained if the calibration solutions did not mix properly and were more concentrated than expected, or if some of the glue used to seal the mylar film was present in the measurement volume, as glue is very dense.

The calibration solutions were much denser than the tissue samples and hence had to be counted for a much longer time to obtain good counting statistics. The 10% solution was counted for 4 hours, the 5% solution was counted for 1 hour and the 2% solution was counted for 40 minutes. Due to the extremely tight time constraints involved when working at a synchrotron source it was not possible to perform the calibration measurements first to ensure that precise calibration data has been collected and so this error arose without there being an opportunity to repeat the measurements. However the calibration graph has been plotted without the two anomalous points included. Although a calibration graph with only two points plus the origin is not ideal it has produced results which are consistent with the results produced in the laboratory and so was assumed to be the correct data points to include.

3.5 Summary

The electron density of 85 samples of 5 different breast tissue classifications were measured in the laboratory. The $K_{\alpha 2}$ line from a tungsten target industrial x-ray tube was used and the scattered x-rays collected at an angle of 30° . The Compton and coherent photon peaks were resolved using an energy dispersive detector and peak fitting software. The measured counts were corrected for the attenuation by the sample of both the primary and scattered beam. The system was calibrated using solutions of known electron density. Five of these samples were also taken to the European Synchrotron Radiation Facility. Here measurements were performed at 13keV with the detector at 112° . The same calibration and correction procedures were applied as for the laboratory measurements. These repeat measurements were performed as a test of consistency. The results of each of these sets of measurements are presented in chapter 4, as well as a comparison between the laboratory and synchrotron measurements.

Chapter 4 Electron density measurement results and analysis

4.1 Introduction

The measurements in the laboratory were performed in two sessions, each with the same energy and experimental configuration but with different sample holder designs, which were discussed in section 2.4.2. The system was calibrated each time, allowing the results to be presented together as one data set. In section 4.2.4 the results are assessed by comparison to average tissue data published in International Commission on Radiological Units and Measurements (ICRU) Report 46. (1992). This report was prepared in order to provide the required information to those using tissue substitute materials to calculate absorbed doses for dosimetric purposes. This report contains tabulated values for the elemental composition, mass densities and the electron densities for a range of important human body tissues.

The results were obtained using the theory outlined in section 3.2 and the methods described in Section 3.3.1. The calibration graphs were presented in section 3.4. The measurements performed at the ESRF synchrotron were carried out on the same areas of the same samples measured in the laboratory and so cannot be regarded as independent measurements. These results are presented in section 4.3 and are then compared to the results obtained in the laboratory in section 4.4. These measurements serve to act as a test for reproducibility and consistency.

4.2 Laboratory measurements

4.2.1 Final results

Figure 4.1 is a box and whisker plot of the results obtained in the laboratory. The box plot was drawn with the statistical analysis package Sigmastat version 3.1 (Systat Software Inc.). The thick line shows the median of each tissue type. The interquartile range is a stable measure of spread and is shown by the box. It is the difference between the 25th and 75th percentile. The whiskers show values within 1.5 box lengths

of the box. Any values that lay more than 3 box lengths from the edges of the box are shown as outliers which appear as circles on the graph. This is a useful way in which to visualise this data set and using the median, rather than the mean, is more representative when examining data sets that may have outliers, as is the case for this data.

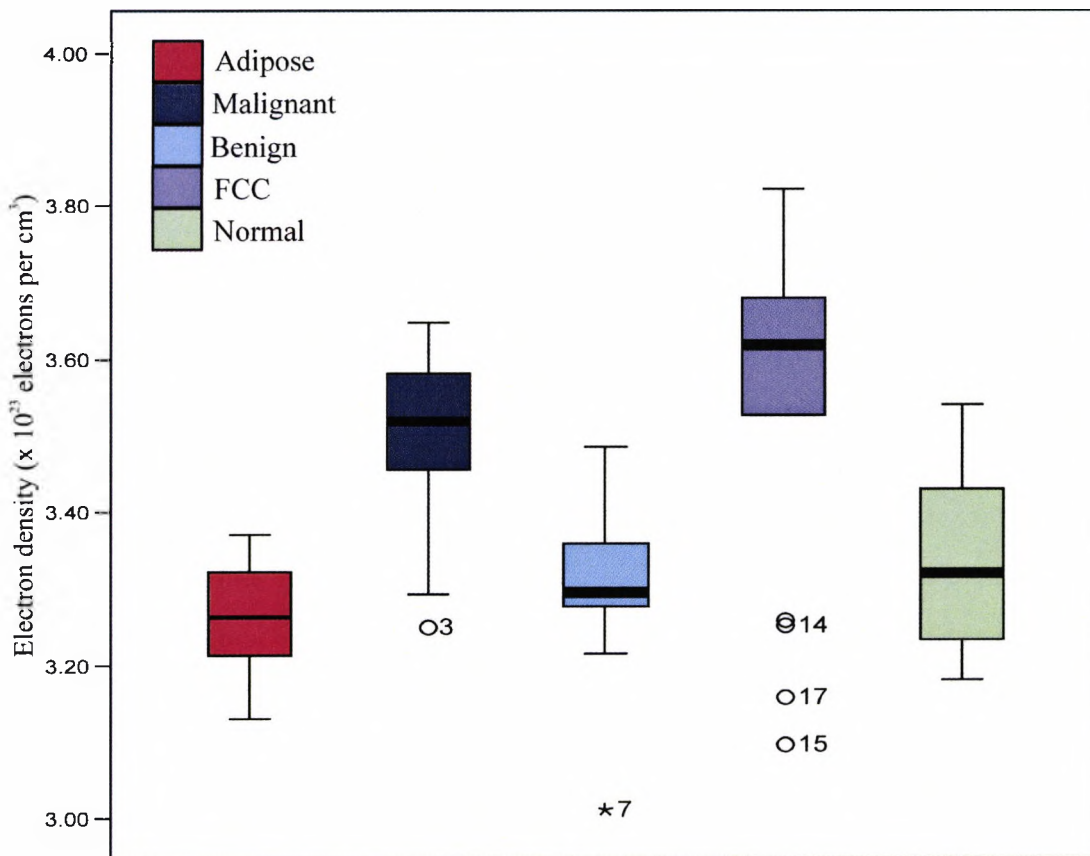


Figure 4.1 A box and whisker plot for the laboratory electron density data

The statistical parameters for the results are given in table 4.1. It should be noted that the sample size for the normal samples is only 7. For any sample size lower than about 12 it is difficult to make any useful assessments of the population that the samples have come from. These data have still been included in the analysis but it is important to bear this in mind.

Chapter 4 Electron Density Measurement Results and Analysis

| | Adipose | Tumour | Benign | FCC | Normal |
|----------------------|---------|--------|--------|--------|--------|
| Mean | 3.262 | 3.503 | 3.296 | 3.537 | 3.338 |
| Sample size | 17 | 24 | 20 | 17 | 7 |
| Standard deviation | 0.073 | 0.086 | 0.052 | 0.211 | 0.142 |
| Median | 3.267 | 3.506 | 3.283 | 3.618 | 3.321 |
| Lower 95% conf limit | 3.224 | 3.467 | 3.271 | 3.429 | 3.207 |
| Upper 95% conf limit | 3.299 | 3.539 | 3.320 | 3.646 | 3.470 |
| 95% conf. interval | 0.075 | 0.072 | 0.049 | 0.217 | 0.263 |
| Minimum | 3.130 | 3.292 | 3.212 | 3.097 | 3.181 |
| Maximum | 3.371 | 3.647 | 3.394 | 3.821 | 3.540 |
| Normality test KS | 0.1357 | 0.1033 | 0.1875 | 0.2461 | 0.2128 |
| P value | >0.10 | >0.10 | >0.10 | >0.10 | >0.10 |
| Passed? | Yes | Yes | Yes | Yes | Yes |

All quantities are $\times 10^{23}$ electrons per cm^3

Table 4.1 The statistical parameters for the electron density results obtained in the laboratory

In table 4.1 the 95% confidence interval is the range of values which the true mean of the population that the sample has been taken from, and so the true mean should lie within these limits in 95% of cases where a sample of this size and standard deviation has been analysed from the population in question. A large confidence interval indicates that the mean of the sample data may be quite different from the population mean.

The data samples have all passed the Kolmogoro-Smirnov (KS) test for normality. The KS value represents how far the sample data deviates from a Gaussian distribution. The P value then shows the likelihood that this sample distribution could have been sampled from a non-Gaussian distribution and still have produced the quoted KS value by chance. If the P value is greater than 0.01 then the sample is said to have passed the test for normality and the population was most likely to be Gaussian. In this data set all the sample groups have passed the normality test. The results for each tissue type have been displayed as a histogram to give a clear picture

of the spread of results obtained for each tissue type. These are shown in the figures 4.2 to 4.6, with the Gaussian distribution curve added.

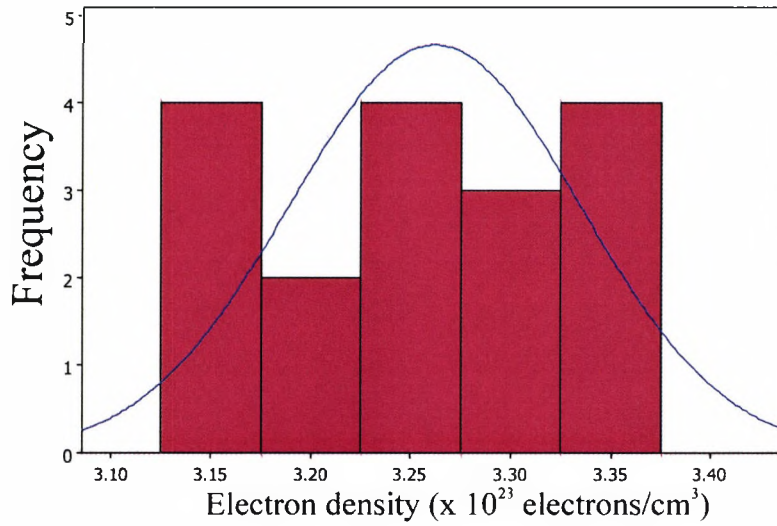


Figure 4.2 Histogram of adipose electron density results

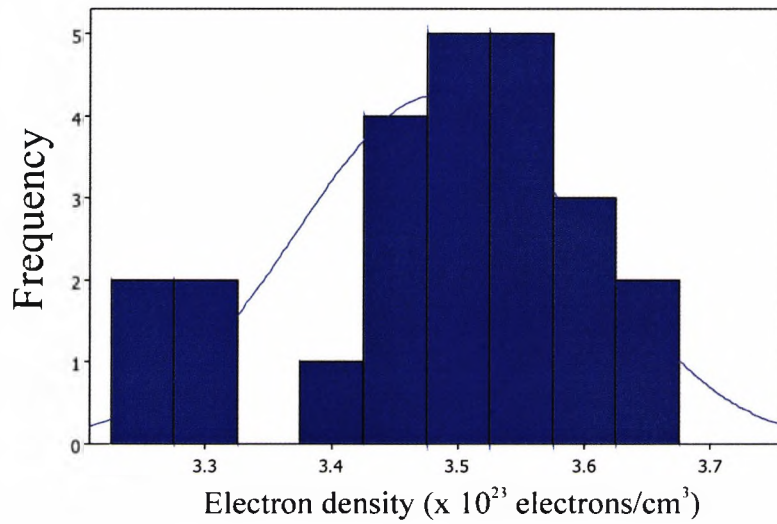


Figure 4.3 Histogram of malignant tissue electron density results

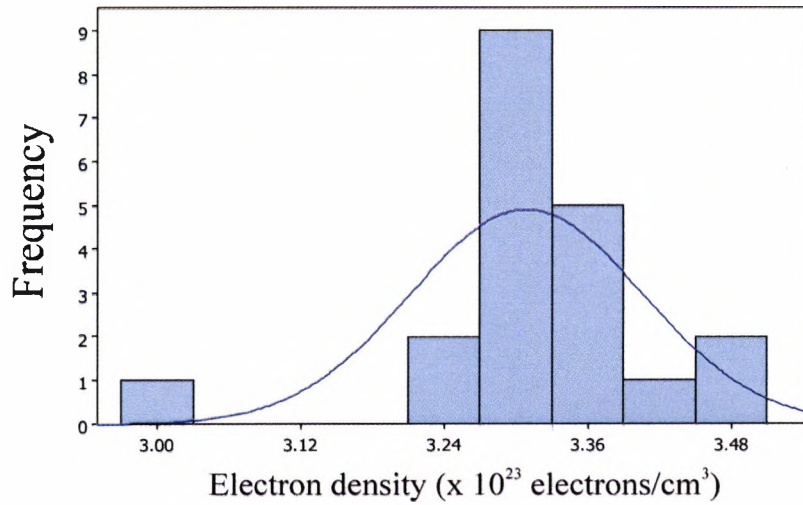


Figure 4.4 Histogram of benign electron density results

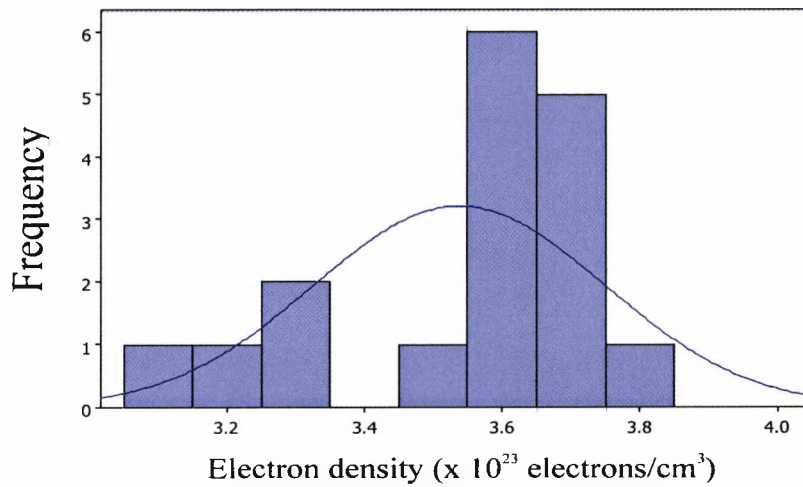


Figure 4.5 Histogram of FCC electron density results

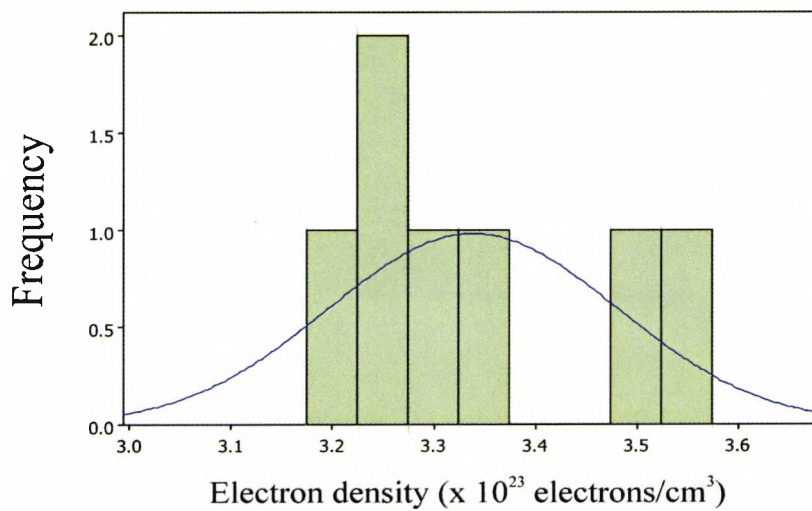


Figure 4.6 Histogram of normal tissue electron density results

4.2.2 Errors

There are a number of errors associated with each measurement. The dominant error to take into account is the error in determining the background counts to be subtracted from the peak counts.

Each individual measurement is subject to statistical variation. The error σ is given as:

$\sigma = \sqrt{\frac{\bar{x}}{N}}$ where \bar{x} is the mean number of counts if the reading is repeated N times.

For the scatter readings each measurement was measured for a long enough time (4 hours) to ensure that the error on the counts was sufficiently low (>0.5%).

The largest error is associated with the subtraction of the background counts. As described above the background was calculated by taking readings from two channels. These readings were repeated 10 times each. If x_1 is the channel number and \bar{y}_1 is the mean number of counts recorded over 10 measurements, then the error on the number of counts measured in the first channel is given by

$$\sigma_{y_1} = \pm \sqrt{\frac{y_1}{10}} \quad [4.1]$$

and the error on the number of counts measured in the second channel is given by

$$\sigma_{y_2} = \pm \sqrt{\frac{y_2}{10}} \quad [4.2]$$

If the gradient, m, of the line joining these two points is given by

$$m = \frac{\Delta y}{\Delta x} = \frac{y_2 - y_1}{x_2 - x_1} \quad [4.3]$$

The error on Δy is found by propagating the errors on y_1 and y_2 :

$$\sigma_{\Delta y}^2 = \sigma_{y_1}^2 + \sigma_{y_2}^2 \quad [4.4]$$

Assuming the error on x is zero then the fractional error on m is the same as the fractional error on Δy and is given by

$$\left(\frac{\sigma_m}{m}\right)^2 = \left(\frac{\sigma_{\Delta y}}{\Delta y}\right)^2 \quad [4.5]$$

If $c = y_1 - mx_1$, where c is the point of intersection of the line joining points (x_1, y_1) and (x_2, y_2) the error on c is equal to:

$$\sigma_c^2 = \sigma_{y_1}^2 + \sigma_m^2 \quad [4.6]$$

For each channel in the peak window area the background counts for channel X_i is given by $Y_i = mX_i + c$ and the error on the counts in channel X_i is given by

$$\sigma_{Y_i}^2 = (\sigma_c^2 + \sigma_m^2) + (\sqrt{Y_i})^2 = \sigma_{y_1}^2 + 2\sigma_m^2 + Y_i \quad [4.7]$$

Where the $(\sqrt{Y_i})^2$ term represents the statistical fluctuation in Y_i counts. As the straight line is only found from two points the error on the straight-line equation is minimal. Therefore the error on the background count calculation is dominated by the statistical error of the counts in each channel.

Using this method the overall error on the background count calculation is 4.2%

Other sources of error are the effect of multiple scatter, the error in positioning and the error in repositioning the sample for the transmission measurements. None of these other errors have been considered as they are very difficult to quantify and are small compared to the background subtraction error outlined above.

4.2.3 Statistical Analysis

The hypothesis (H_0) that is being tested by this experiment is that adipose, benign, malignant, FCC and normal tissues are distinguishable from one another using the parameter of electron density. The median value of electron density of each tissue type is significantly different from the other. This can be expressed as:

$$H_0 : \bar{x}_m - \bar{x}_n \neq 0 \quad [4.8]$$

where \bar{x}_m is the median value of electron density for one tissue type and \bar{x}_n is the median for another tissue type. The corresponding null hypothesis (H_A) states that all tissue types have the same median value for their electron density values, and any apparent difference observed is purely as a result of random sampling. This is stated as:

$$H_A : \bar{x}_m - \bar{x}_n = 0 \quad [4.9]$$

In order to be able to treat the data as parametric the data must pass a normality test, which analyses whether the data are taken from a Gaussian distribution, and the data sets being tested must have identical standard deviations. As shown above in table 4.1 the electron density data results have passed a normality test. The standard test to compare many groups is the ANOVA (Analysis of Variance) test. However for this test to be robust the variance of each data group must be similar. Bartlett's test was applied to see whether the variances are similar enough for the data to be considered as parametric, however this test gave a negative result. In some cases transforming the data through taking the log of each result can result in the data set becoming a more normal distribution, however in this case transforming the data was not successful in reducing the difference in variances. Therefore instead of using the ANOVA test the Kruskal-Wallis analysis of Variance test was used. This is the best test to use in this case to test the study hypothesis. This is a non-parametric test which is better for data with large variation within groups. However non-parametric tests have less power with small sample sizes, those less than about 50. In the case of small

sample sizes the P values returned tend to be higher, increasing the likelihood that a significant difference may be returned as non-significant. This is the type I error rate, which is higher for small sample sizes.

The Kruskal-Wallis (KW) test compares all the data as though they were from a single data set and tests whether all the data could be from the same population. The KW test gives a value of H and a P value which needs to be small. Dunn's pairwise test is then used to examine each pair of data sets to see whether they are significantly different. This test returns a P value for each pair of data sets. A low value of P is required for different populations. The data analysis has been carried out utilising Graphpad Instat version 3.06.

The results returned by this statistical package are $H = 38.999$, $P < 0.001$. The results of the post-hoc test, which makes pairwise comparisons to identify the different groups, are given in table 4.2.

| | | | Mean rank | | |
|-------------------|-----|-----------|-------------------|--------------------|----------------|
| Comparison | | | difference | Significant | P value |
| Adipose | vs. | Malignant | -37.105 | significant | $P < 0.001$ |
| Adipose | vs. | Benign | -6.697 | ns | $P > 0.05$ |
| Adipose | vs. | FCC | -38.529 | significant | $P < 0.001$ |
| Adipose | vs. | Normal | -10.79 | ns | $P > 0.05$ |
| Malignant | vs. | Benign | 30.408 | significant | $P < 0.001$ |
| Malignant | vs. | FCC | -1.424 | ns | $P > 0.05$ |
| Malignant | vs. | Normal | 26.315 | ns | $P > 0.05$ |
| Benign | vs. | FCC | -31.832 | significant | $P < 0.001$ |
| Benign | vs. | Normal | -4.093 | ns | $P > 0.05$ |
| FCC | vs. | Normal | 27.739 | ns | $P > 0.05$ |

Table 4.2 Dunn's multiple comparisons for the laboratory electron density results

In table 4.2 significant is when $P < 0.001$ and not significant (ns) is when $P > 0.05$.

4.2.4 Comparison to ICRU Report 46 data

The values of electron density for standard tissue compositions given in the International Commission on Radiation Units and measurements (ICRU) report 46 (ICRU, 1992) are also displayed. In this report three separate values are given for different tissue compositions. The elemental compositions of these six tissues have been given in the table below (table 4.3). It is worth noting that the values quoted in this report are for healthy tissues only, as there are no published data for malignant tissue growths.

| Tissue | H | C | N | O | Other | Electron density ($\times 10^{23} \text{ e}^-/\text{cm}^3$) |
|--------------|------|------|-----|------|------------------------------|--|
| Adipose #1 | 11.2 | 51.7 | 1.3 | 35.5 | 0.1 Na, 0.1 S, 0.1 Cl | 3.241 |
| Adipose #2 | 11.4 | 59.8 | 0.7 | 27.8 | 0.1 Na, 0.1 S, 0.1 Cl | 3.179 |
| Adipose #3 | 11.6 | 68.1 | 0.2 | 19.8 | 0.1 Na, 0.2 S, 0.1 Cl | 3.118 |
| Glandular #1 | 10.9 | 50.6 | 2.3 | 35.8 | 0.1 Na, 0.1 P, 0.1 S, 0.1 Cl | 3.299 |
| Glandular #2 | 10.6 | 33.2 | 3 | 52.7 | 0.1 Na, 0.1 P, 0.2 S, 0.1 Cl | 3.390 |
| Glandular #3 | 10.2 | 15.8 | 3.7 | 69.8 | 0.1 Na, 0.1 P, 0.2 S, 0.1 Cl | 3.511 |

*Table 4.3 The elemental compositions (percentage by mass) of adult tissues
(ICRU Report 46, 1992)*

It is usually assumed that malignant tissue has approximately the same structure as healthy glandular tissue. This is because tumours are usually within fibrous tissue rather than growing in purely fatty (adipose) tissue. The electron densities of the tissues can be compared to the values obtained experimentally. These are presented in figure 4.7.

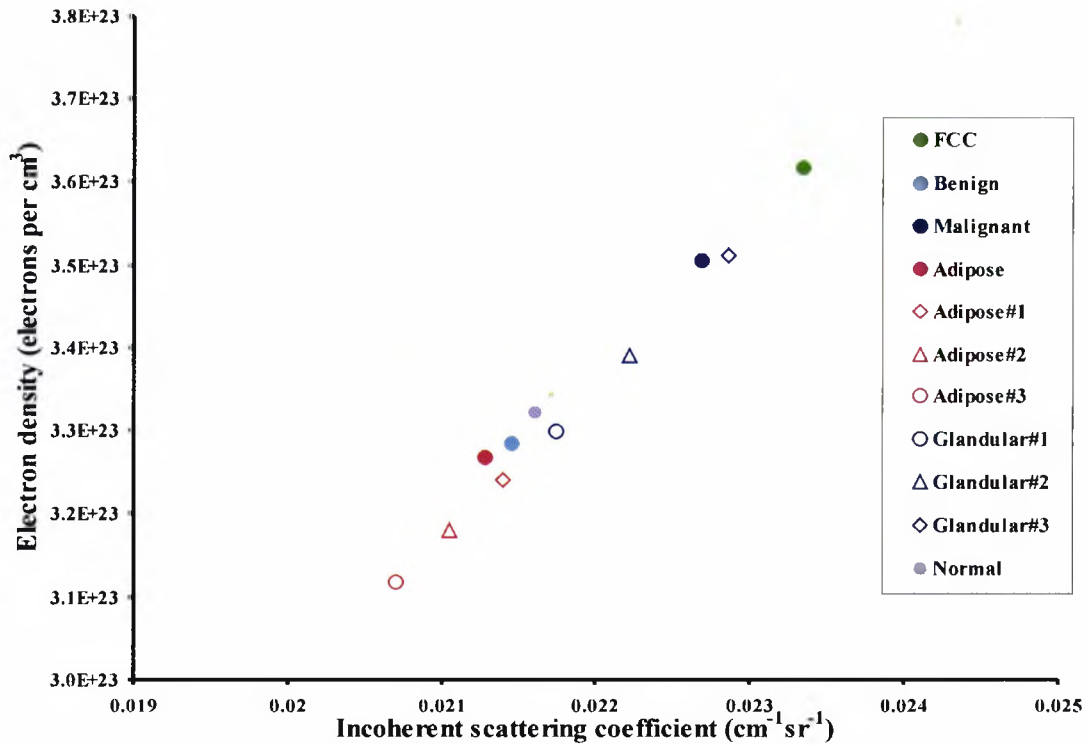


Figure 4.7 A graph comparing the values for the experimental data and the published values from ICRU Report 46 (1992)

4.2.5 Discussion

The results given in table 4.1 show that there is a difference between the electron density of adipose and malignant tissue, to a value of 7.3% when comparing the median values. Statistical analysis has shown the difference between adipose and malignant tissues to be significant, with a p-value of <0.001. This magnitude is broadly consistent with the values found by using the adipose and glandular tissue values from ICRU report 46. The average value for glandular tissue (ICRU 46 glandular#2) is 6.6% higher than the average adipose value (ICRU 46 adipose #2). The electron density value found for malignant tissue is in very good agreement with Al-Bahri and Spyrou (1998), who quoted a value of 3.564×10^{23} electrons per cm³, where this study found a value of 3.504×10^{23} electrons per cm³. These values are 1.7% different. They found a smaller (3%) difference between these two tissue types, with the malignant tissue having the higher electron density value.

There has been no composition values published for fibroadenoma or FCC tissues. However the measurements made within this study found a difference in the electron density of fibroadenoma and adipose tissues to the value of 2.2% and a difference

between FCC and adipose tissue to be 10.7%. It is difficult to verify these results using the literature, as there are no published data from any previous studies that have used these tissue types. Statistical analysis has shown the difference between fibroadenoma and adipose tissues to be non-significant. The comparison between the adipose and FCC tissues is highly significant, with a p value of <0.001.

The value found for the normal fibrous (glandular) tissues was 3.321×10^{23} electrons per cm^3 . This falls within the range of published values for normal tissues, being 0.7% higher than the ICRU Glandular #1 value and 2% lower than the average glandular value. The statistical analysis shows that the normal results are not significantly different from any of the other tissue groups. This is due to the large spread of values. This data group has a standard deviation which is twice as large as the standard deviation for the adipose tissues.

The results of the FCC measurements have a bimodal distribution, and this is also seen to some extent with the normal and the tumour tissues. This does suggest that there may be sub-groups within one classification of tissue that may be linked to other differences, for example age or diet, which this sample size is not sufficient to detect. As a result the FCC data shows a number of outliers and the normal tissues have a large range. The malignant tissues show just one outlier. It would be incorrect to discard these results as anomalous and so therefore have been included in any subsequent analysis. Further measurements are needed to see whether these trends are true data trends or are due to random experimental errors. As the normal and other tissues seem to demonstrate this bimodal behaviour this could be investigated using matched pairs of samples.

The biggest source of inaccuracy comes from the small number of samples used. The results found with a small sample size can give a good indication of the population under observation but with a low power. Power calculations were carried out using Sigmastat (Systat Software Inc.) and Minitab (Minitab Inc.) in order to find out the number of samples that are required in each tissue type in order to be able to get results of a 95% confidence level and 80% power. The values of required sample size, n were calculated to be 42 by Sigmastat and 46 by Minitab. This shows that the sample sizes used here are only about one third, or less, of the minimum numbers needed for a valid study.

4.3 Synchrotron measurements

4.3.1 Final results

The results for this section have been displayed in the same way as the results for the laboratory results, with a box plot (figure 4.8), a table (table 4.4) and a histogram for each tissue type (figures 4.9 to 4.13). The box and whisker plot shows the results of the electron density measurements made at the ESRF synchrotron radiation facility.

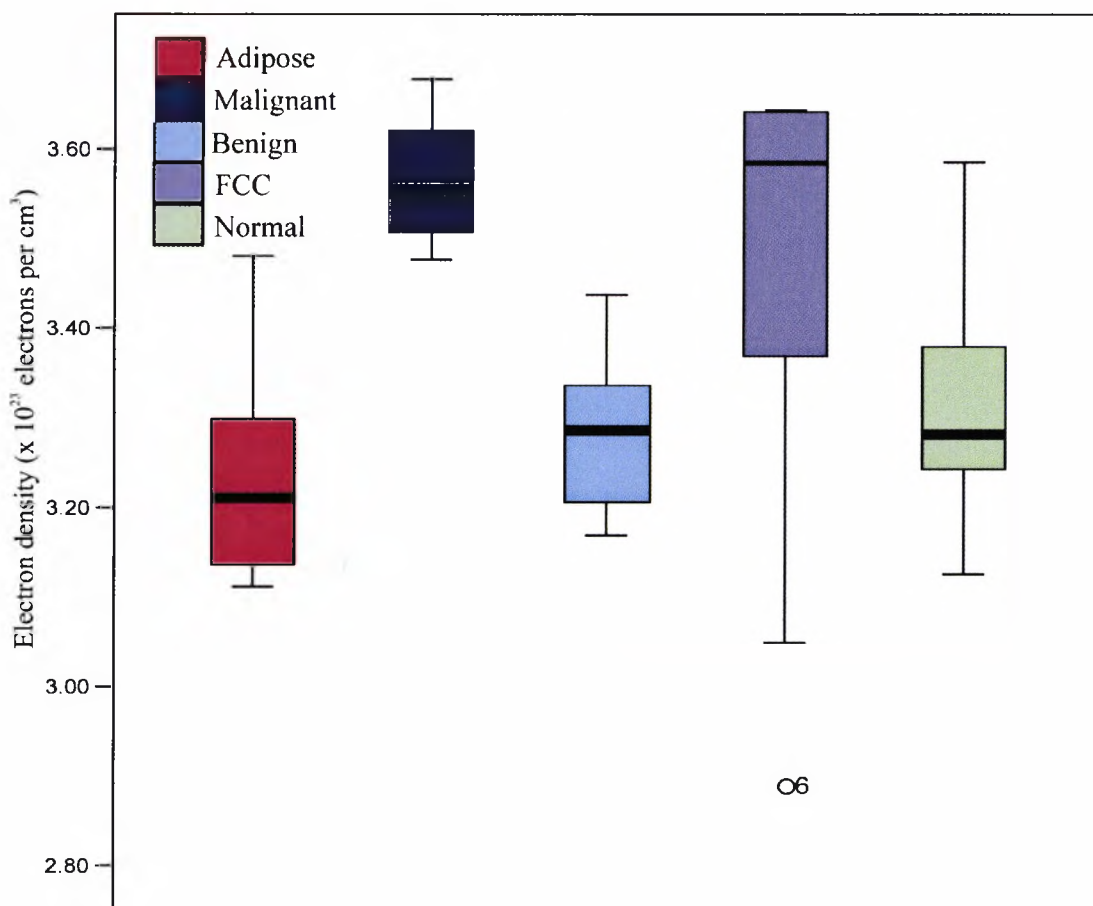


Figure 4.8 A box and whisker plot for the ESRF electron density data

| | Adipose | Malignant | Benign | FCC | Normal |
|----------------------------|---------|-----------|--------|------|--------|
| Mean | 3.25 | 3.57 | 3.29 | 3.51 | 3.18 |
| Sample size | 8 | 10 | 9 | 10 | 9 |
| Standard deviation | 0.04 | 0.02 | 0.03 | 0.10 | 0.09 |
| Median | 3.25 | 3.55 | 3.31 | 3.64 | 3.24 |
| Lower 95% confidence limit | 3.15 | 3.52 | 3.22 | 3.28 | 2.96 |
| Upper 95% confidence limit | 3.35 | 3.62 | 3.36 | 3.74 | 3.40 |
| Minimum value | 3.12 | 3.48 | 3.17 | 2.89 | 2.84 |
| Maximum value | 3.48 | 3.68 | 3.44 | 3.81 | 3.73 |

All quantities are $\times 10^{23}$ electrons per cm^3

Table 4.4 The statistical results for the ESRF measurements of electron density

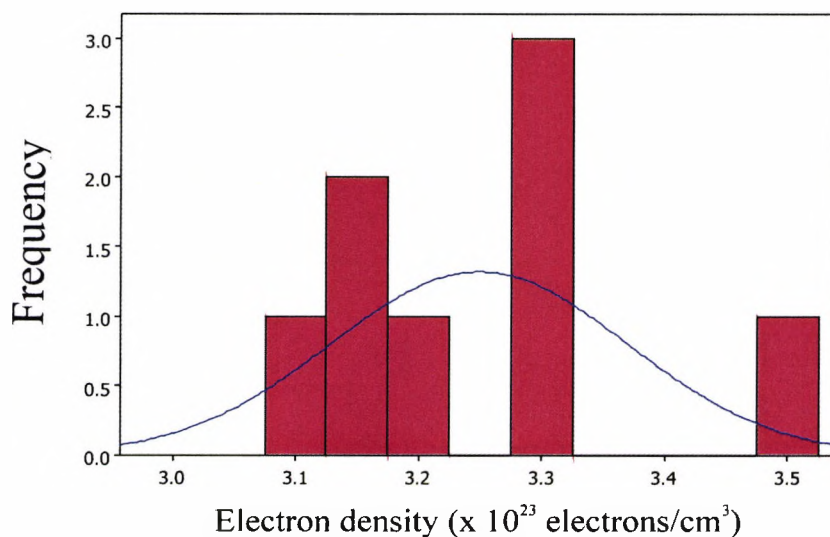


Figure 4.9 Histogram of adipose tissue electron density results

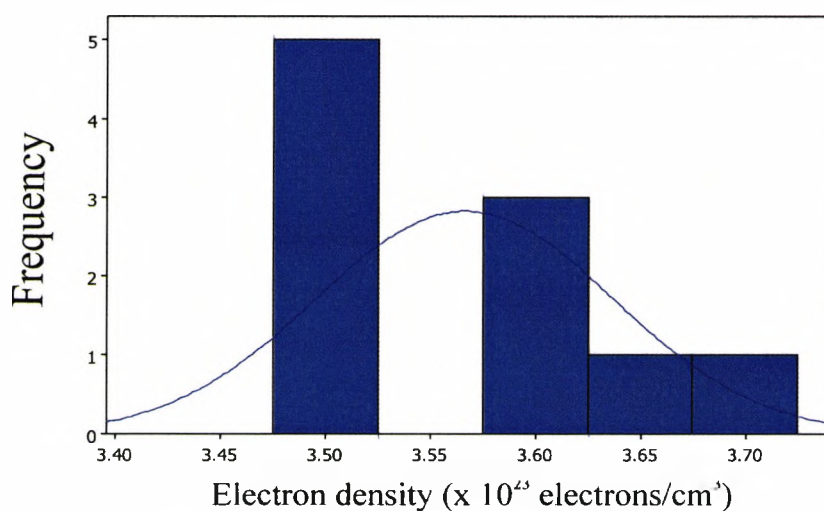


Figure 4.10 Histogram of malignant tissue electron density results

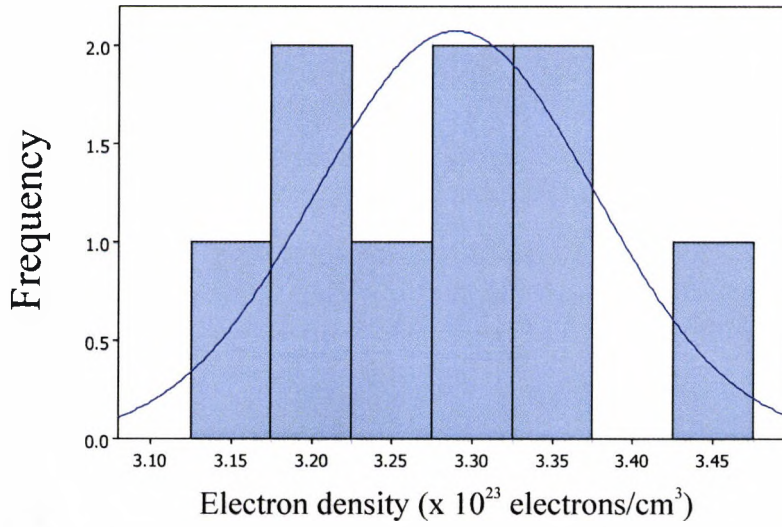


Figure 4.11 Histogram of benign tissue electron density results

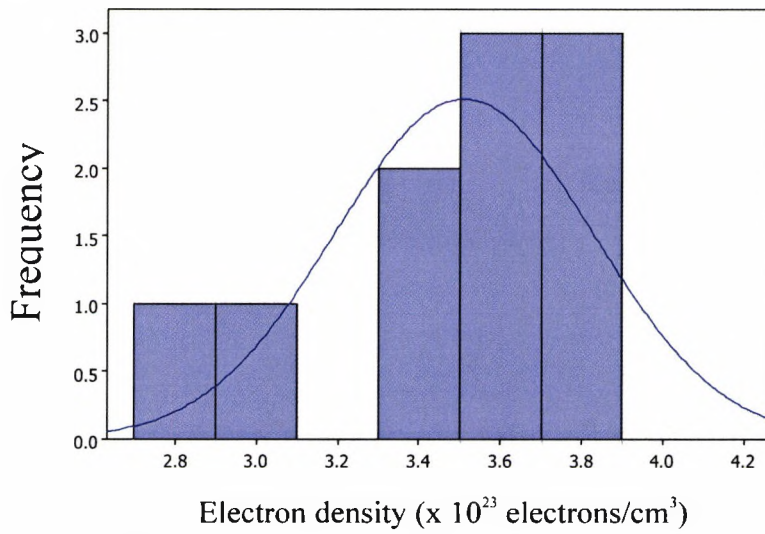


Figure 4.12 Histogram of FCC tissue electron density results

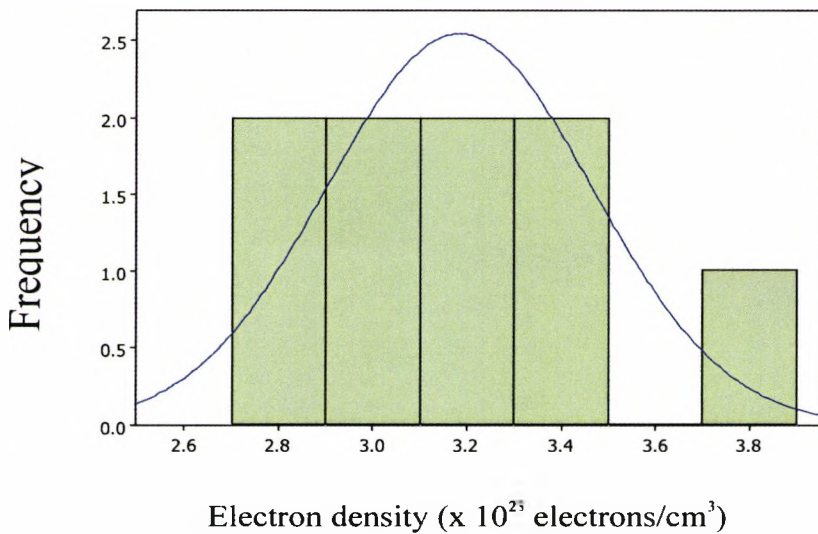


Figure 4.13 Histogram of normal tissue electron density results

4.3.2 Errors

The errors on the measurements are much smaller than those for the laboratory results. This is because there is no background subtraction to be done and the number of counts is also much larger because of the higher flux. This is the largest error and is quantified as $\frac{1}{\sqrt{n}}$ where n is the number of counts in the scatter peak.

4.3.3 Statistical Analysis

The formal and null hypotheses are the same as for the laboratory results (equations 4.8 and 4.9), and will be tested in the same way. The data sets were much smaller than those from the laboratory experiments, due to the time constraints involved with working with a synchrotron source. For sample sizes of 10 or less, as these are, it is difficult to test for normality. As these samples have passed a normality test before when part of a larger sample set it can be assumed that they are from a normal population. A Kruskal-Wallis test was performed on the data. The P value for the data is 0.0006, which is considered extremely significant. Therefore variation among column medians is significantly greater than expected by chance. The P value has been approximated (from chi-square distribution) because exact calculations would have taken too long, as the sample sizes are so small. The results of the KW test are given in table 4.5. The Kruskal-Wallis Statistic $KW = 19.444$

| Number of group | Sum of points | Mean of ranks | Ranks |
|------------------------|----------------------|----------------------|--------------|
| Adipose | 8 | 121 | 15.13 |
| Malignant | 10 | 349 | 34.90 |
| Benign | 9 | 166 | 18.44 |
| FCC | 10 | 316 | 31.60 |
| Normal | 9 | 129 | 14.33 |

Table 4.5 The parameters found from the Kruskal-Wallis sum of ranks test

Dunn's Multiple Comparisons Test was also performed on the data and the results of these tests are given in table 4.6. In the following table, * = quite significant, when $P < 0.05$; ** = significant, when $P < 0.01$; ns = not significant, when $P > 0.05$.

| | | | Rank difference | | P value |
|-----------|-----|-----------|-----------------|----|------------|
| Adipose | vs. | Malignant | -19.78 | * | $P < 0.05$ |
| Adipose | vs. | Benign | -3.32 | ns | $P > 0.05$ |
| Adipose | vs. | FCC | -16.48 | ns | $P > 0.05$ |
| Adipose | vs. | Normal | 0.79 | ns | $P > 0.05$ |
| Malignant | vs. | Benign | 16.46 | ns | $P > 0.05$ |
| Malignant | vs. | FCC | 3.30 | ns | $P > 0.05$ |
| Malignant | vs. | Normal | 20.57 | ** | $P < 0.01$ |
| Benign | vs. | FCC | -13.16 | ns | $P > 0.05$ |
| Benign | vs. | Normal | 4.11 | ns | $P > 0.05$ |
| FCC | vs. | Normal | 17.27 | ns | $P > 0.05$ |

Table 4.6. Dunn's multiple pairwise comparison tests for the ESRF electron density data

These tests are inconclusive as for small sample sizes the type I error rate, not picking up differences in data sets that may actually be significant, are increased. This can be seen in table 4.6, where only small differences have been detected between adipose versus malignant and malignant versus normal. This data set, therefore has limited use in being able to help differentiate between the tissue types. The real value in this data was to be able to compare the measurement systems, which is described in the following section.

4.4 Comparison of measurement systems

Figure 4.14 is the two sets of measurements made displayed on the same box plot to make comparison easier. It can be seen from this figure that the results display the same trends and the medians for similar samples are also similar. It is difficult to quantify this statistically due to the small sample sizes. However a t-test has been performed on each pair of data sets (comparing like tissue samples measured with the two systems) and these tests showed no significant difference between the data sets.

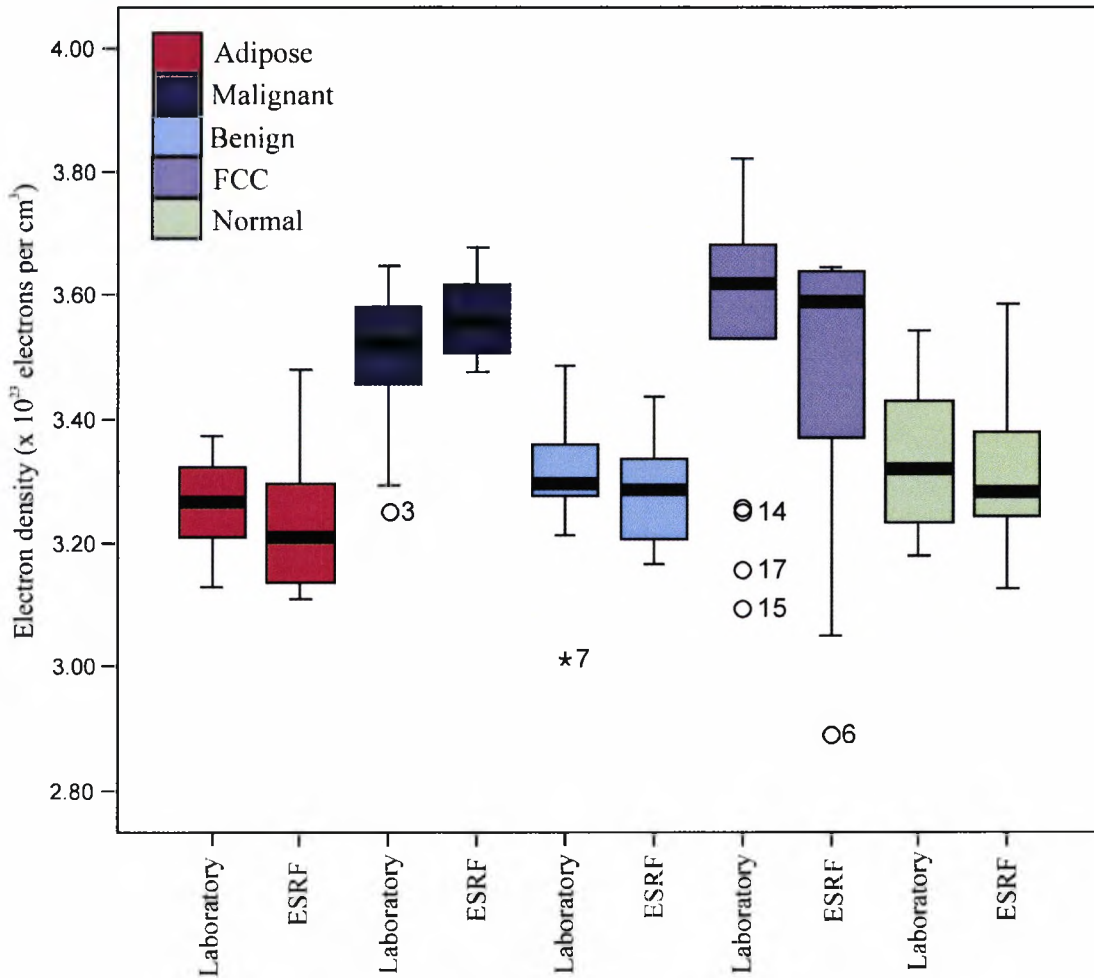


Figure 4.14 Box plot comparing the Laboratory and synchrotron measurements

Figure 4.15 is a histogram of the differences between the two measurements made on the same sample. The differences are calculated as the absolute difference between the two measurements and given as a percentage of the laboratory measurements, so the differences quoted show how different the synchrotron measurements are compared to the laboratory. The results show that 72.3% of the measurements were within 5% of each other. 23.4% of the measurements were between 5% and 10% and 4.3% (2 samples) were above 10% different when measured in the two experimental systems.

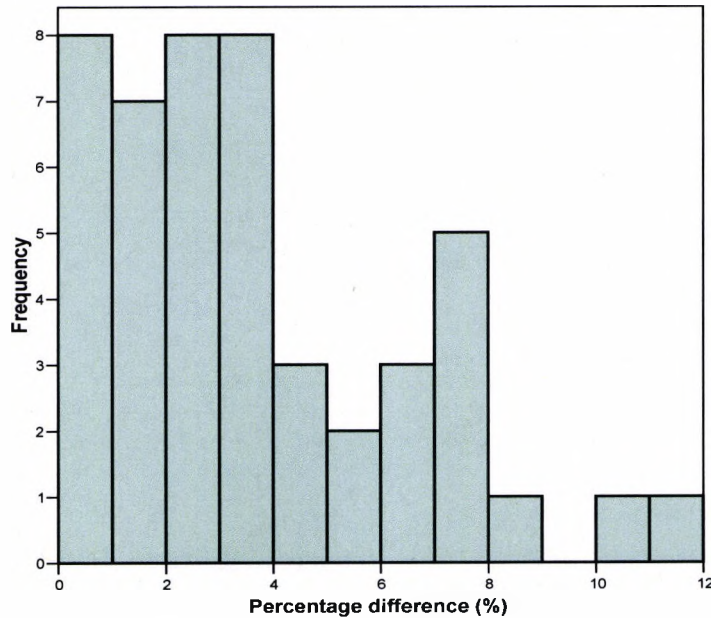


Figure 4.15 Histogram of the synchrotron measurements as a percentage difference from the laboratory measurements for individual samples

The two measurement systems have given comparable results. Despite the sample numbers used at the synchrotron being very small it has provided good verification of the measurement system used in the laboratory.

4.5 Summary

The results of the laboratory and synchrotron results were presented. A Kruskal-Wallis test was applied to the data followed by Dunn's pairwise test. This was to evaluate whether each combination of tissue types were statistically significant from one another. The results obtained have shown that there is a difference between adipose and malignant tissue, to a value of 7.3%, and between adipose and FCC, to a value of 10.7%. These were both shown to be significant. The differences between adipose and fibroadenoma tissues (0.5%) and between malignancy and FCC (3.2%) are not significant. The results have been compared to the data tables published by the International Commission of Radiological Units (ICRU, 1992) and found to be in good agreement.

A comparison of the laboratory and synchrotron measurement systems showed that 72.3% of the results were within 5% of each other for the two result sets, which is a good verification of the results, although the sample sizes measured at the ESRF are too small to draw any statistically sound comparisons between tissue types.

Chapter 5 Scatter Profile Measurement

5.1 Introduction

The coherent scattering distribution holds valuable information regarding the molecular structure of the material used as a scattering medium. The first diffraction experiments involving crystals were performed by Max von Laue in 1912. He verified that x-rays have wavelike properties and the evenly spaced atoms in a crystal act as a diffraction grating producing an interference pattern. Sir William Bragg and his son Laurence performed extensive work on the x-ray analysis of crystals and formulated the Bragg condition for x-ray diffraction. This is given as

$$2 d \sin \theta = n \lambda \quad [5.1]$$

where d is the spacing of the planes within the crystal, λ is the wavelength of the incident wave and θ is the angle of incidence. Equation 5.1 states that constructive interference from a crystal occurs when the Bragg condition is met, i.e. when the path length difference between two waves diffracted from successive planes within a crystal is an integral number of wavelengths of the incident photon.

It has been known for a long time that amorphous materials display a diffraction pattern, similar to that displayed by crystalline structures (Johns and Yaffe 1983). The interference of coherent photons is related to the interatomic and molecular forces within the material. Amorphous materials such as body tissues show an oscillatory pattern fading to the free electron case (i.e. the theoretical assumption that all electrons within the material are independent) at high scattering angles. As each material exhibits a different pattern, this pattern may be used to characterise different media, and because of this has been termed a scatter signature or profile.

From looking at the Bragg condition (equation 5.1) it can be seen that the conditions for constructive interference are dependent on the angle of scatter and the wavelength (or energy) of the incident photons. This has led to the development of two different techniques for the x-ray analysis of materials, angular dispersive and energy dispersive. The first uses a monochromatic source and measures the intensity of

scattered photons at a range of angles (Angular Dispersive X-Ray Diffraction (ADXRD)). The second looks at a fixed angle for a range of incident energies (Energy Dispersive X-Ray Diffraction (EDXRD)). The oscillatory structure function describes the interatomic and molecular bond effects. The coherent differential cross section (1.22) against momentum transfer (1.13) is usually graphically displayed and this is what is termed the scatter signature.

This study has looked at using both techniques for the analysis of breast tissue. The aim of these measurements is to see whether there is a discernable difference in scatter profile between five tissue types, adipose, benign, malignant, FCC and normal tissues.

Section 5.2 will look at the theory used to convert the measured scatter counts into coherent scatter cross sections. The methods used at both synchrotrons and in the laboratory are described in section 5.3. The correction and normalisation processes are also outlined in this section. The results are presented in the next chapter (chapter 6).

5.2 Theory

The aim of the experiment is to measure the value of the coherent scattering coefficient per unit solid angle σ_{coh} as a function of momentum transfer. A detector will be used to measure the number of counts at each value of momentum transfer $N(\bar{x})$. These counts will be converted to the coherent scattering coefficient from the measured data. In order to do this a number of corrections must be applied and then the data must be normalised. These corrections are different for each measurement technique, due to the different physical processes that are taking place. The following relation is applicable when analysing Energy Dispersive X-Ray Diffraction (EDXRD) spectra. The linear coherent scattering coefficient, σ_{inc} , is given by:

$$\sigma_{coh} = \left\{ \frac{(N(\bar{x}) - B)}{A_f T} \right\} \alpha - \sigma_{inc} \quad [5.2]$$

$N(\bar{x})$ is the number of counts measured at each momentum transfer value. The term B denotes the background signal. A_f is a factor which accounts for the differential attenuation, or beam hardening of the scatter signal. T is a factor which is to correct for the output spectrum of the x-ray tube and α is a normalisation factor, which is found by using the independent atomic model. σ_{inc} is the linear incoherent scattering coefficient and is given by equation 1.19 and is reproduced here for clarity

$$\sigma_{inc}(\bar{x}, Z) = \rho N_A \frac{d\sigma_{KN}}{d\Omega} \frac{S(\bar{x}, Z)}{M} \quad [1.19]$$

and is the probability that a photon will be Compton scattered when interacting with a material of density ρ and molecular mass M . N_A is Avogadro's constant. This is a background signal from Compton scattered photons. If the sample composition is known then σ_{inc} can be calculated using the sum rule to find S/M for a mixture, as given by equation 5.3

$$\frac{S(\bar{x})}{M} = \sum_i \frac{S_i(\bar{x})}{m_i} \omega_i \quad [5.3]$$

The density can be substituted for the electron density, ρ_{e^-} , as given by equation 3.3:

$$\rho_{e^-} = \frac{\rho N_A Z}{M} \quad [3.3]$$

Rearranging this gives

$$\rho N_A = \rho_{e^-} \frac{M}{Z} \quad [5.4]$$

Equation 5.4 can now be substituted into equation 1.19

$$\sigma_{inc}(\bar{x}, Z) = \rho_{e^-} \frac{M}{Z} \frac{d\sigma_{KN}}{d\Omega} \frac{S(\bar{x}, Z)}{M} \quad [5.5]$$

where

$$\frac{M}{Z} = \sum_i \frac{m_i}{Z_i} \omega_i \quad [5.6]$$

α is a normalisation factor based on the free electron case at high values of momentum transfer, called the Independent Atomic Model (IAM) correction factor and is given by:

$$\alpha = \frac{(N(\bar{x})_{corrected})_{High \bar{x}}}{(\sigma_{scatt})_{High \bar{x}}} \quad [5.7]$$

$(N(\bar{x})_{corrected})$ is the measured counts which have been corrected and is expressed as:

$$(N(\bar{x})_{corrected}) = \left\{ \frac{(N(\bar{x}) - B)}{A_f T} \right\} \quad [5.8]$$

In equation 5.7 σ_{scatt} is the total scattering coefficient:

$$\sigma_{scatt} = \sigma_{coh} + \sigma_{inc} \quad (cm^{-1}sr^{-1}) \quad [5.9]$$

where σ_{coh} was given by equation 1.22, $\frac{d\sigma_{Th}}{d\Omega}$ is the Thomson differential coherent cross section and $F(\bar{x})$ is the form factor

$$\sigma_{Coh} = \rho N_A \frac{F^2(\bar{x})}{M} \frac{d\sigma_{Th}}{d\Omega} \quad [1.22]$$

where again the sum rule must be used as stated in equation 1.23:

$$\frac{F^2(\bar{x})}{M} = \sum_i \frac{F_i^2(\bar{x})}{m_i} \omega_i \quad [1.23]$$

Therefore σ_{scatt} is given by

$$\sigma_{scatt} = \rho_e \frac{M}{Z} \left\{ \frac{F^2(\bar{x})}{M} \frac{d\sigma_{Th}}{d\Omega} + \frac{S(\bar{x})}{M} \frac{d\sigma_{KN}}{d\Omega} \right\} \quad [5.10]$$

α can now be found for high values of \bar{x} by substituting equations 5.8 and 5.10 into 5.7.

For angular dispersive x-ray diffraction (ADXRD) spectra measurements the differential coherent scattering coefficient can be found using equations 5.11 and 5.12:

$$\sigma_{coh} = \left\{ \frac{\left[\left(\frac{N(\bar{x})}{M} \right) - B \right]}{A_f V} \right\} \alpha - \sigma_{inc} \quad [5.11]$$

$$(N(\bar{x})_{corrected}) = \left\{ \frac{\left[\left(\frac{N(\bar{x})}{M} \right) - B \right]}{A_f V} \right\} \quad [5.12]$$

As for equation 5.2, $N(\bar{x})$ is the number of counts measured at each momentum transfer value. M is a normalisation reading taken from a beam monitoring detector. B is the background signal. A_f is a factor which corrects for the attenuation of the beam by the sample. V is a scatter volume correction. α and σ_{inc} are the same as for the Energy Dispersive case and are found in the same way, which will be described in section 5.3. Each of the correction factors above are described for each measurement system in the following section.

5.3 Experimental and data correction methods

5.3.1 Introduction

As previously described, both EDXRD and ADXRD measurements have been performed. The reason for the two methods being used was essentially instrumental. The angular dispersive measurements were made at the European Synchrotron Radiation Facility (ESRF) and at the Daresbury Synchrotron Radiation Source (SRS) There the equipment available is highly specialised and much more sophisticated than the equipment available in the laboratory. Without the goniometer mounted detector it is only possible to perform energy dispersive measurements as the experimental set-up required is more straight forward. It is interesting to be able to compare the results obtained with the two techniques. It is expected that the ADXRD measurements will be more accurate.

5.3.2 Angular Dispersive X-Ray Diffraction (ADXRD) measurements

5.3.2.1. Method used at Daresbury SRS:

The experiment was run using 10 keV photons. The beam was focussed down to be 0.5mm x 0.5mm at the sample surface. The tissue samples were held in a slide holder, as described in section 2.3, at 50° from the incident beam axis. This was to ensure that the frame of the sample holder would not lie within the path of the scattered beam at any measurement angle. The samples were secured with 4µm thickness Mylar film, to ensure minimum beam attenuation. The radiation reaching the detector was collimated to 0.5mm x 0.5mm at the detector surface using collimators. A measurement of the number of scattered photons was made at 0.2° intervals over an angular range from 2 to 68° in the vertical plane, as shown in figure 5.1. An HPGe detector was mounted on the 2-theta goniometer arm.

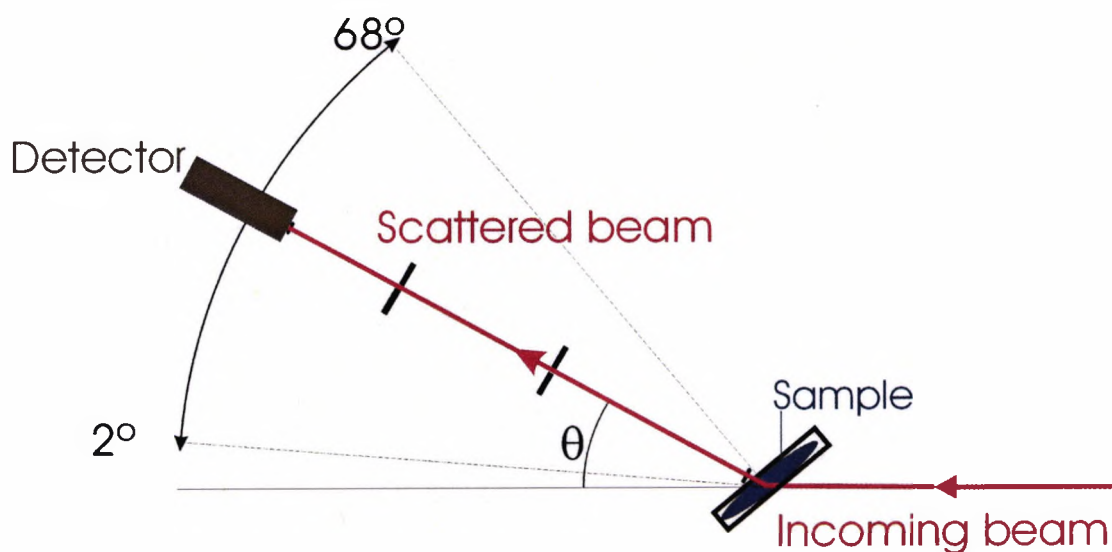


Figure 5.1 The experimental set-up used at Daresbury SRS

5.3.2.3 Data Corrections

The raw data were plotted as spectra and then corrected according to the relationship given in equation 5.2 with the following correction factors applied to the raw data:

M - Beam monitor factor

The output of the synchrotron is monitored with an ionisation chamber at a point before the beam enters the experimental hutch. Each measurement is normalised to the reading from this monitor chamber to account for any fluctuations in the intensity of the beam incident on the tissue.

B - Background

A profile was measured for an empty sample holder that had no scatter medium present but with the mylar film windows in place. The measured profile can be seen in figure 5.2. The spectrum contains a number of sharp peaks, due the long chain molecules present in the polymer. These peaks can be confused with structure peaks and must be removed.

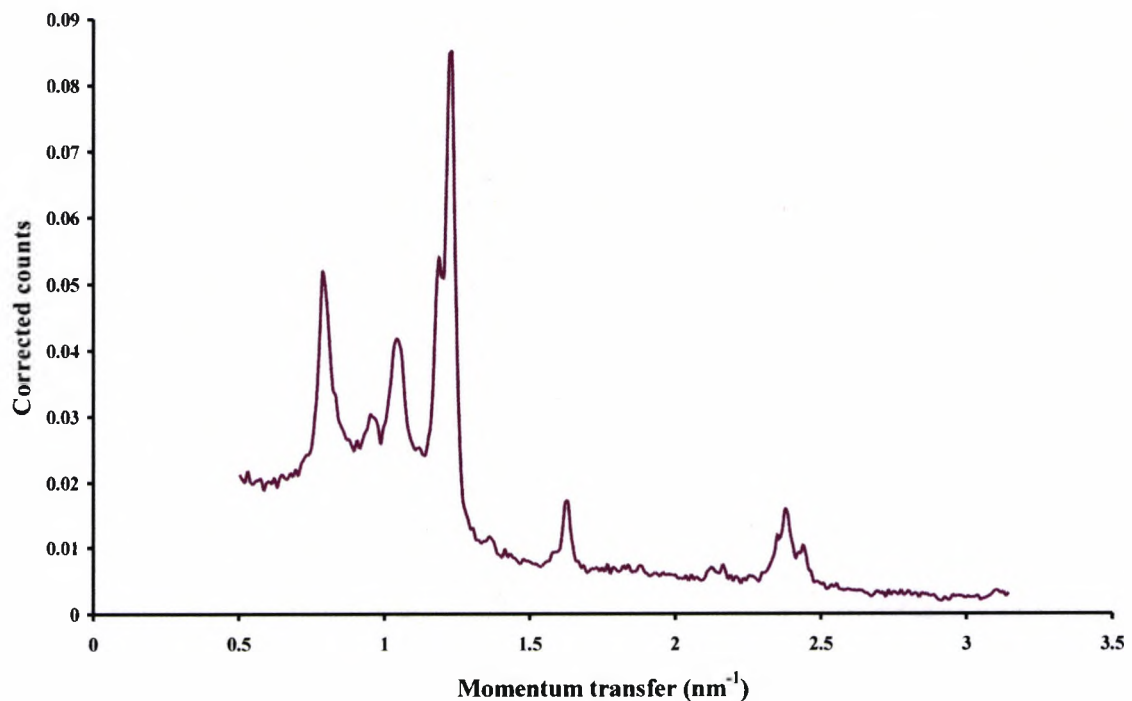


Figure 5.2 A scatter profile of mylar film

A_f - Attenuation factor

A correction for attenuation is needed. The attenuation accounts for the different path lengths travelled by the radiation within each sample. From Figure f.3 below the sample width T is at an angle of 50° to the incident beam axis.

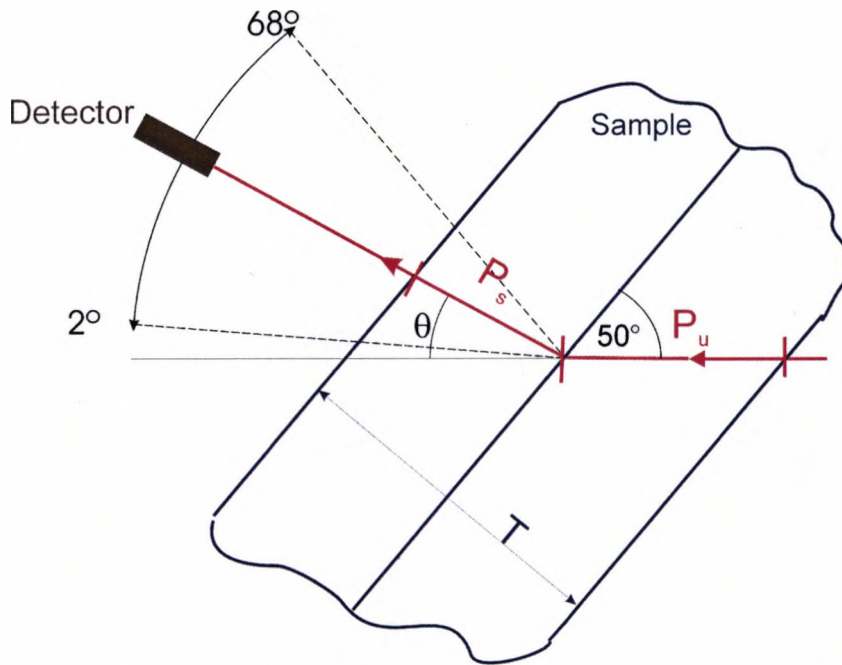


Figure 5.3 Illustration of the attenuation correction

P_u is the path length of the radiation before it is scattered and P_s is the path length of the radiation once it has been scattered by the tissue. θ is the angle of the detector from the horizontal plane, with $\theta_{\min} = 2^\circ$ and $\theta_{\max} = 68^\circ$. From the diagram above it can be seen that

$$P_u = \frac{T/2}{\cos 40^\circ} \quad [5.13]$$

$$P_s = \frac{T/2}{\cos(40^\circ - \theta)} \quad [5.14]$$

$$\text{Total path length } L = P_u + P_s = \frac{T/2}{\cos 40^\circ} + \frac{T/2}{\cos(40^\circ - \theta)} \quad [5.15]$$

$$= \frac{T/2 (\cos 40^\circ + \cos(40^\circ - \theta))}{(\cos 40^\circ \cos(40^\circ - \theta))} \quad [5.16]$$

The total path length L is then substituted into Beer's Law (equation 1.2) for the attenuation of radiation in matter to give equation 5.17:

$$A_f = \frac{I}{I_0} = e^{-\mu L} \quad [5.17]$$

where I is the number of attenuated photons, I₀ is the number of incident photons and μ is the linear attenuation coefficient of the material.

For tissue the values of μ were measured by recording number of counts with the sample of the tissue in the beam at an angle of zero degrees (I) and recording the number of counts with no sample in the beam (I₀). With this configuration the path length L is simply the thickness of the samples, which is 2 mm. By substituting these values of I, I₀ and L into Beer's law the value of μ can be calculated.

V Scattering volume correction

Figure 5.4 illustrates the concept of the scattering volume. This is the area where the incident and the scattered beam intersect. Only tissue in this volume can contribute to the scattering process. Throughout the experiment the detector is moving position and so therefore the scattering volume is changing. A correction needs to be applied to remove any effects due to this changing scattering volume.

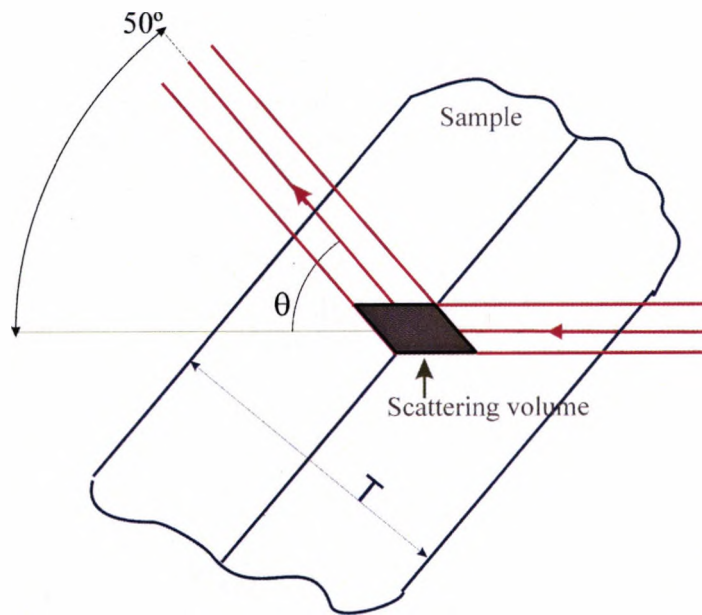


Figure 5.4 The scattering volume within the tissue

It must also be taken into account that for smaller angles some of the scattering volume lies outside the tissue and so will not contribute to the interaction process. This is shown in figure 5.5.

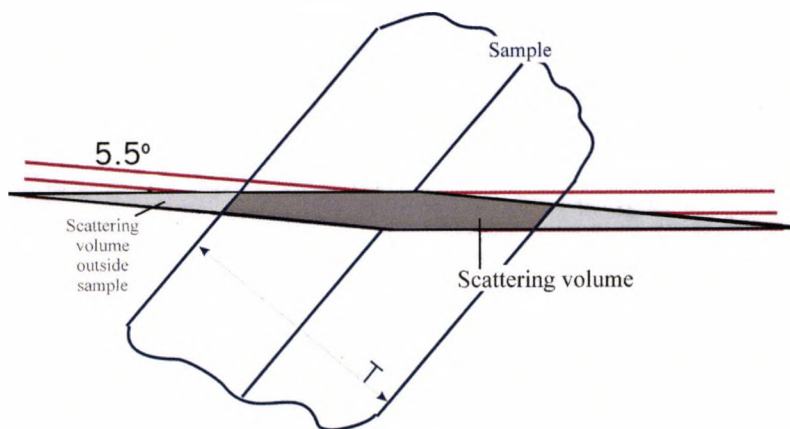


Figure 5.5 The scattering volume at small angles

There are three stages to calculating the scattering volume.

1. Calculate the angle at which the scattering volume becomes completely contained within the tissue volume. This occurs when the scattering length (S) is shorter than the tissue measurement along the same line (L).

This is calculated by

$$S = \frac{W}{\sin\left(\frac{\theta}{2}\right)} \quad [5.18]$$

$$L = \frac{T}{\cos(\theta - 40^\circ)} \quad [5.19]$$

where W is the width of the focussed beam and θ is the angle of scatter.

If $F(\theta) = S - L$ then for $F > 0$ then the scattering volume falls outside the tissue.

2. For angles where $F(\theta) < 0$, the scattering volume is calculated as

$$V = \frac{W}{2} \left(\frac{1}{\tan\left(\frac{\theta}{2}\right)} + \tan\left(\frac{\theta}{2}\right) \right) h \quad [5.20]$$

where W is the width and h is the length of the focussed beam.

3. For angles where $F(\theta) > 0$, some of the total intersection volume lies outside the tissue, so the volume which lies outside the tissue must be subtracted from the total intersection volume. The factor for this is calculated as follows:

$$V' = V - \left\{ 2 \left(F \sin\left(\frac{\theta}{2}\right) \right) \left(F \cos\left(\frac{\theta}{2}\right) + \frac{F \sin\left(\frac{\theta}{2}\right)}{\tan 50^\circ} \right) h \right\} \quad [5.21]$$

5.3.2.2. Method used at the ESRF

At the ESRF the experimental set up, illustrated in figure 5.6, was similar to that at Daresbury. The sample holder was changed to a cylindrical tube of 4.6mm diameter, the third sample holder described in section 2.3. The experiment was performed at 13keV for an angular range of 5° to 65°. The angular resolution was used at two settings; the measurements were made at 0.25° resolution for the 5° to 45° range and at 1° resolution for the angular range 46° to 65°. This was because there is no structure at the higher angles, but just a structureless tail used for normalisation. The scattered beam was collimated to a 0.4mm x 0.4 mm square beam using evacuated slits, as described in section 2.1

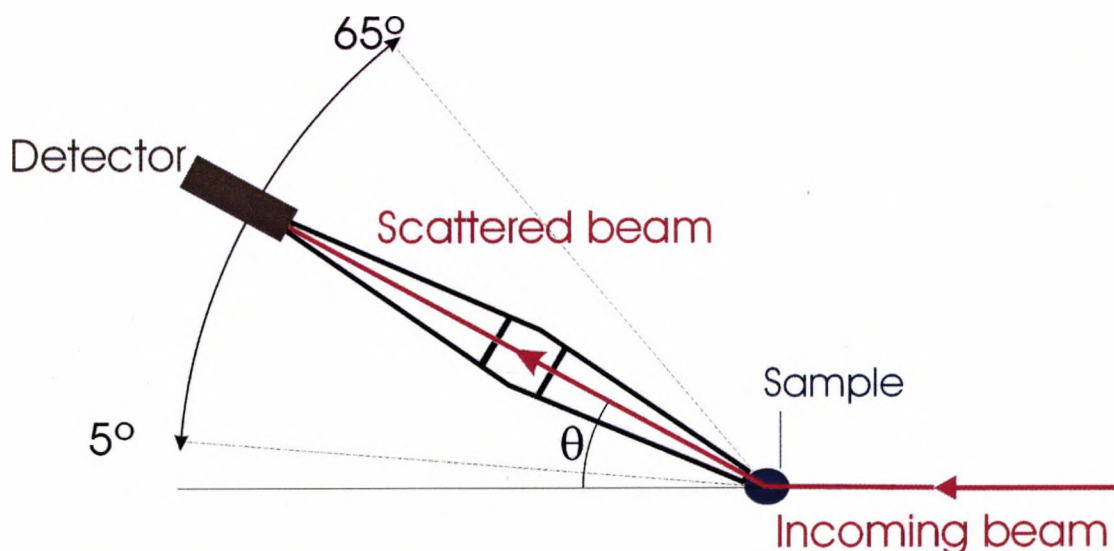


Figure 5.6 The experimental set-up used at ESRF

The attenuation was measured straight through the sample with the detector at zero degrees and then a measurement was made with no sample in the beam. The cylindrical shape meant that the path length L was the same at all positions of the detector and was not dependent on the angle of measurement. This meant that the I/I_0 factor could be directly applied to all readings and was constant.

At the ESRF the sample holder was cylindrical, meaning that the path length of the beam in the sample was constant and always equal to D the diameter of the sample. In this case the scattering volume factor is:

$$V' = V - \left(F \tan\left(\frac{\theta}{2}\right) \right) \quad [5.22]$$

The two corrections required for the cylindrical sample holders are far simpler than those needed for the slide holder design. This can be seen by comparing equation 5.21 with equation 5.22 and the attenuation correction process. This was the reason behind the redesign of the sample holder.

5.3.3 Energy Dispersive X-Ray Diffraction (EDXRD) Measurements

5.3.3.1 Method

The x-ray tube fitted in the radiation laboratory is an industrial Pantak HF160 x-ray tube unit with a tungsten primary target and a maximum operating voltage of 160keV. The tube can be set on a fluoroscopic setting and so run continuously for long periods of time. The anode is fixed and water-cooled, so care must be taken not to overheat the anode. The equipment was set up as shown in figure 5.7.

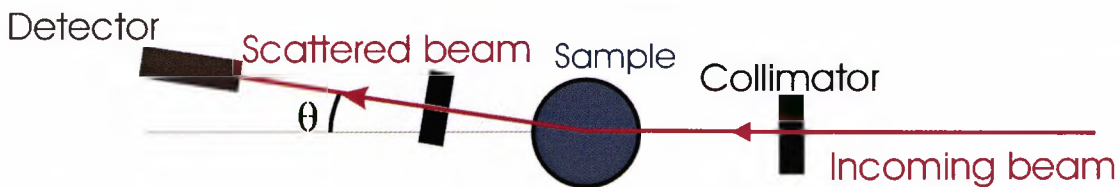


Figure 5.7 The experimental set-up for the Energy Dispersive measurements

The samples were placed at the centre of a rotating platform, positioned so that the measurement volume was in the centre of the tissue. The samples were then rotated about their central axis during the measurements. This was to reduce any effects caused by tissue inhomogeneities through the measurement plane. The beam was

collimated to 0.5mm using a lead collimator both before and after the sample. The distances between the tube, sample and detector were kept to a minimum to reduce any loss flux due to inverse square law effects. The detector was at an angle of $\theta = 9^\circ$ so that there was no plastic from the sample holder within the scattering volume. The second set of measurements were done at 7.5° . This was because the third design of sample holder had the plastic removed from the beam path, replaced with mylar film. This meant the scatter angle could be decreased.

5.3.3.2 Corrections

B – Background

The background counts are measured with the same conditions as a normal measurement but without a sample in place.

A_f – Attenuation Factor

In this case the path length stays the same but because the incident beam consists of a mixture of energies the beam is differentially attenuated. This is a beam hardening effect, as lower energies are attenuated more than higher energies. In order to correct for this in the first instance the ICRU composition values for body tissues were used with the XCOM database program (Berger and Hubbell 1998) to find attenuation factors at each energy. For adipose tissue the ‘adipose #2’ values were used. For fibrous tissues the ‘glandular #2’ values were used. The corrected profiles in the first instance, with this crude attenuation correction applied, were used to calculate the adipose to fibrous ratio of the tissues. As explained in the following section (5.3.4) this ratio was then used to estimate the composition of each individual tissue sample. Once this was done these new composition values were then used with XCOM and the data was corrected again. The process was then repeated in an iterative manner.

T – Tube profile correction

For each incident energy there is a different number of photons incident on the sample, which is dependent on the x-ray tube output profile. The relative output of the x-ray tube measured at 70kV_p is shown in figure 5.8. This spectrum shows the bremsstrahlung, where the characteristic lines have been omitted.

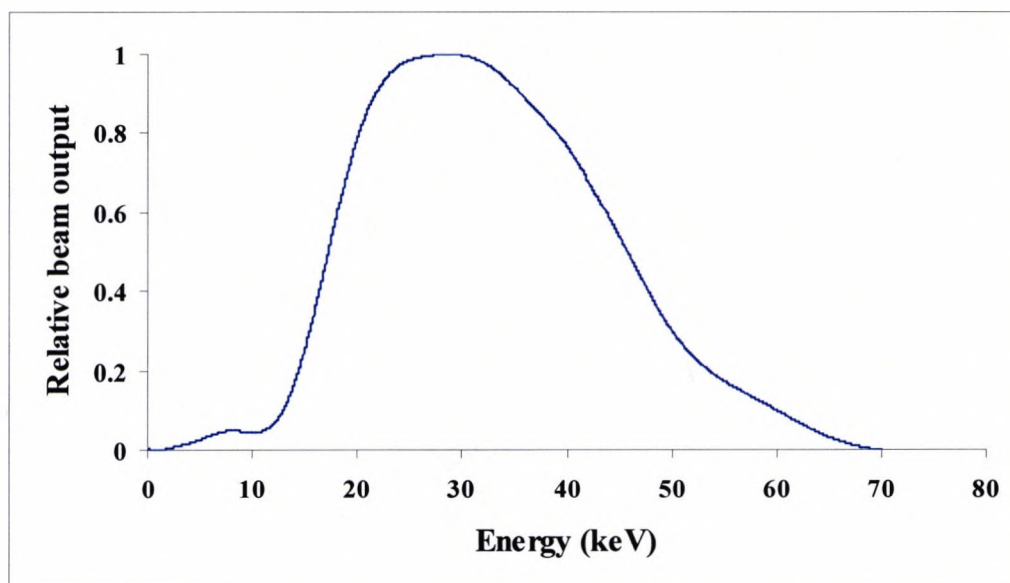


Figure 5.8 The relative output of the x-ray tube measured at $70kV_p$

The tube profile has been normalised to the maximum output. Equation 1.13 can be used to find the energy relating to each momentum transfer value required to correct the scatter profile. The graph in figure 5.8 can then be used to find the relative beam output for each energy, which is the tube correction factor T .

5.3.4 Normalisation and Compton background subtraction

5.3.4.1 Introduction

The data needs to be normalised to enable inter-comparisons between tissue types. The conventional normalisation procedure is based on the scattering at high momentum transfer values. At these high values there are no interference effects and so the scattering can be modelled on an assumption that the electrons within the material are free, and not influencing each other. This correction, called the Independent Atomic Model (IAM), can easily be calculated if the tissue composition is known. In previous studies, performed by other groups, normalisation using this method has been carried out using two techniques, either by using the average data values published in ICRU report 46 (1992) (Peplow and Verghese 1998) or by directly measuring the composition of tissues used (Poletti *et al* 2002).

Neither of these methods is suitable. The electron density measurements performed as part of this study have shown that malignant, benign and normal tissues have a different electron density and therefore molecular composition. It is therefore inaccurate to normalise these three tissue types using the same composition data (i.e. as glandular tissue), however no data has been published concerning the composition of diseased breast tissue, which may be more suitable to use. The second method, using chemical and spectroscopic techniques, results in destruction of the tissues. This was not a viable method to use because of the limited amounts of tissue available and the high costs of this type of examination.

For this study a novel method of profile normalisation has been developed, applying the electron density measurements to produce an individual normalisation factor for each sample. This is proposed as an improvement upon the methods previously used by other groups. This method entails finding the most probable composition of the tissue.

5.3.3.2 Normalisation method

Figures 5.9 and 5.10 show the values taken from ICRU Report 46 (1992) of the composition of human body tissues plotted against the electron density values also given in ICRU 46. The values for adipose and glandular tissue from the ICRU report were given in table 4.3. The data table gives three values for both adipose and glandular tissue which represent the range of tissues found across the population. The values given are high, low and average values for the tissues that were analysed by the ICRU. The values of composition for adipose tissues (figure 5.9) and glandular tissues (figure 5.10) have been displayed to show how the percentages of the four main elements of tissue, hydrogen, carbon, oxygen and nitrogen, change across the range of data given.

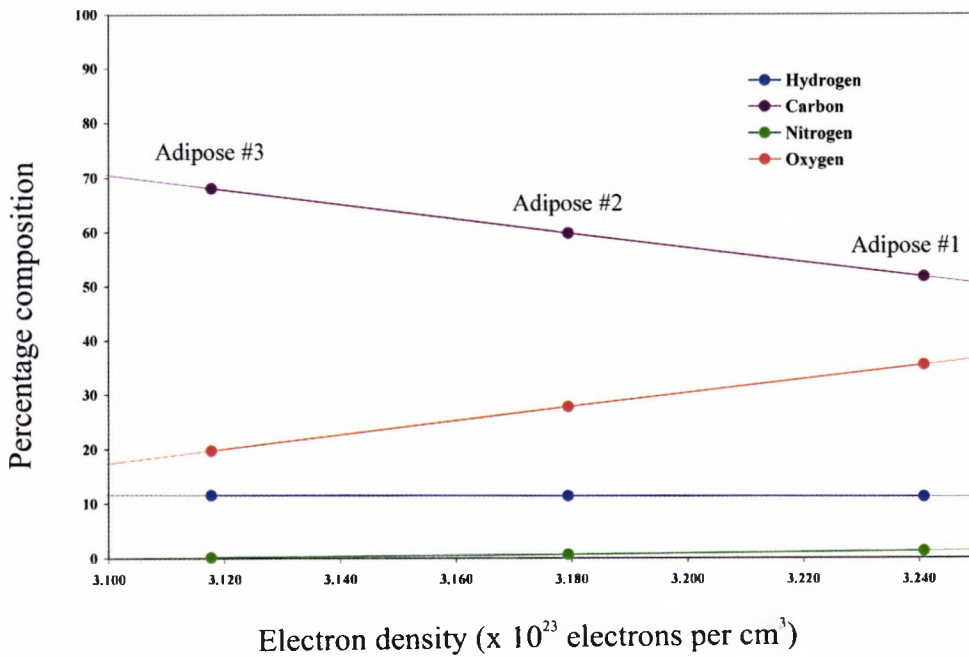


Figure 5.9 The percentage composition of adipose tissues as a function of electron density

There are also minor and trace elements present but these are not in large enough quantities to have an influence on the electron density. It can be seen from figures 5.9 and 5.10 that the percentage content of hydrogen and nitrogen in the tissue stays almost constant, there are very small variations over the range of tissues. This suggests that the variation in composition of the tissues, and hence the electron density, is due to a difference in the percentage variation of oxygen and carbon within the tissue.

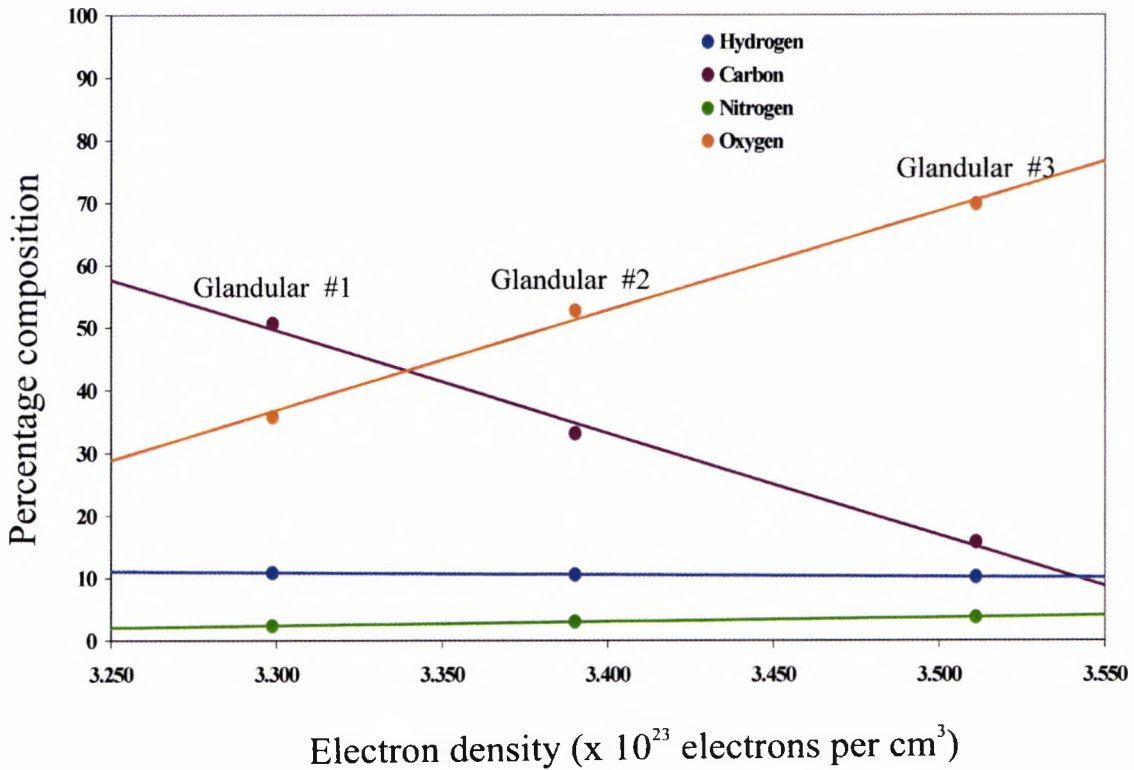


Figure 5.10 The percentage composition of glandular tissues as a function of electron density

Having measured the electron density of each tissue sample these graphs can be used to determine a value for the percentage composition of H, C, N and O for each sample. One set of values can be determined for adipose tissue, H_A , C_A , N_A and O_A , and one for glandular tissues, H_G , C_G , N_G and O_G . As it has been previously shown (Geraki 2003) the scattering profile can be used to determine the adipose and glandular/fibrous content of breast tissue. A method for determining the adipose and fibrous content of the tissue samples is described in section 5.3.3.3. Once this is determined the most probable tissue composition can be determined. This is explained in section 5.3.3.4.

5.3.3.3 Calculation of the adipose to fibrous ratio of the tissue samples

It has been shown previously (Poletti *et al* 2002; Kidane *et al* 1999) that adipose tissue displays a peak at about 1.1 nm^{-1} and fibrous tissues display a peak at about 1.6 nm^{-1} . These two peaks are present in the scatter profiles measured and will be used

to estimate the adipose to fibrous ratio of the content of these two components of breast tissue. The scatter profile spectra were analysed using peak fitting software (PeakFit, SPSS AISN software inc.). The raw spectra were corrected for each of the factors described in sections 5.3.2.3 and 5.3.3.2. They were then smoothed using a Savitzky-Golay smoothing algorithm which is an inbuilt function of the peak fitting software. This is a smoothing method recommended for spectroscopic data as it does not increase the peak widths of the data it is operating on, as is common with other smoothing methods. It applies a least squares fitted polynomial over a window of data for each point. Gaussian peaks were fitted to the data using a model consisting of five peaks. This model was formulated by fitting a peak to the adipose peak at 1.1nm^{-1} and a peak to the fibrous peak at 1.6nm^{-1} . Three other peaks were added to fit the data. This model is shown in figure 5.11. The thick blue line in this graph shows how the model fits to the measured data, which is marked by the orange line. The area of the adipose and fibrous peaks can be output from the peak fitting software. These values were then used to evaluate the amounts of adipose to fibrous tissue present in each sample.

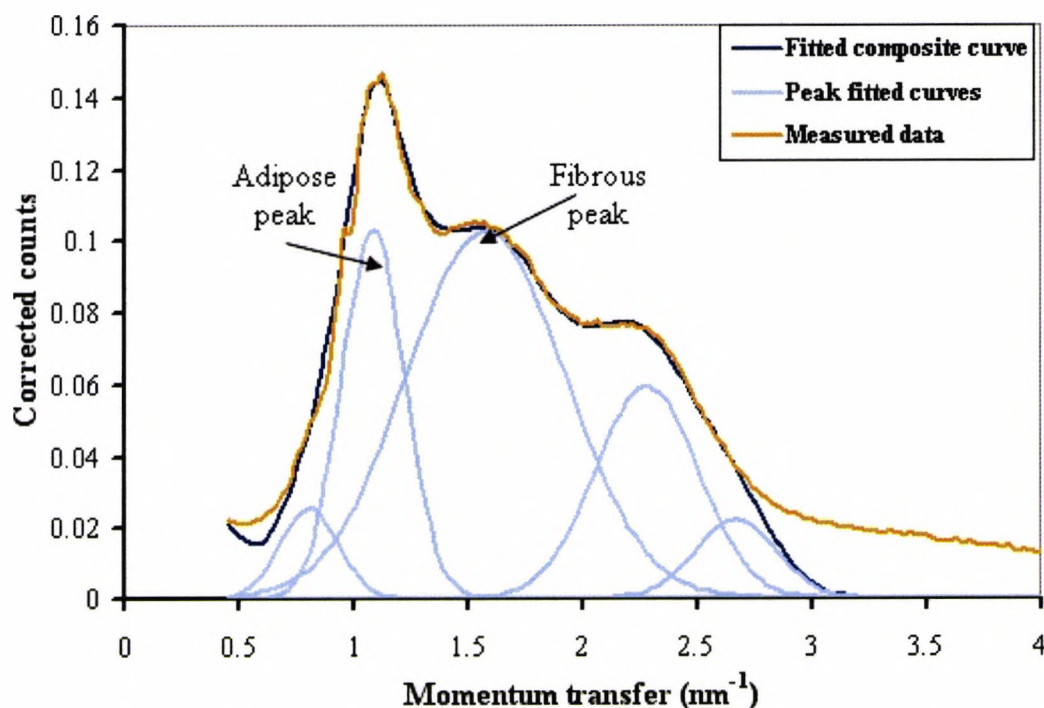


Figure 5.11 Illustration of the peak fitting model used

The adipose to fibrous ratios were then used to calculate a factor, D , between 0 and 1. This factor was found by labelling the adipose tissue with the smallest ratio as 0 and the fibrous tissue with the highest ratio as 1. A linear function was then used to convert the ratio of each tissue function to a value of D . This factor is representative of the amount of fibrous tissue present in the sample. A second factor, B , was also assigned to each tissue sample where

$$B = (1 - D) \quad [5.23]$$

B is representative of the amount of adipose tissue present in the tissue sample.

5.3.3.4 Calculation of the 'best estimate' tissue composition

As described in section 5.3.3.2 each tissue has a value of H_G , O_G , C_G and N_G and a value of H_A , O_A , C_A and N_A where H , O , C and N are the chemical symbols for the elements of hydrogen, oxygen, carbon and nitrogen, and G and A denote the ICRU data used to derive each set of values. A 'best estimate' (denoted by the subscript C) was then found for the quantities of the 4 elements present in each individual tissue sample using the B and D factors found in section 5.3.3.4, where

$$H_C = DH_G + BH_A \quad [5.24]$$

$$O_C = DO_G + BO_A \quad [5.25]$$

$$C_C = DC_G + BC_A \quad [5.26]$$

$$N_C = DN_G + BN_A \quad [5.27]$$

A complete table of these composition values for each tissue sample is given in appendix 2. This method is not intended to be a method to find precise tissue composition values. It is intended to be the best way of normalising the scatter profiles with no means of determining the tissue compositions through spectroscopic or analytical methods.

5.3.3.5 Calculation of the Independent Atomic Model (IAM) normalisation factors

The values of α and σ_{inc} from equations 5.5 and 5.7 can now be calculated. Figure 5.12 shows the cross sections calculated using the method outlined in sections 5.3.3.2, 5.3.3.3 and 5.3.3.4. The total scattering cross section is the sum of the Compton and coherent scattering cross sections. The scatter profile has been normalised to the total scattering cross section (normalised scatter profile 1) and the coherent cross section, where the Compton background has been subtracted (normalised scatter profile 2).

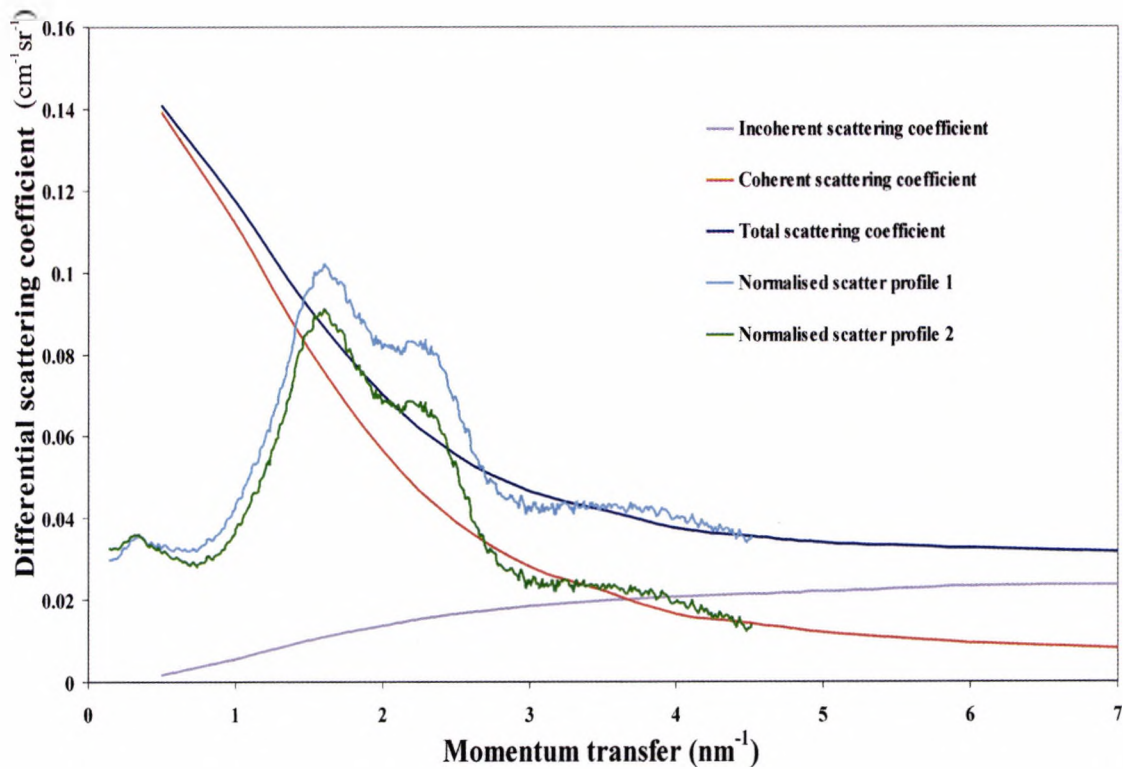


Figure 5.12 A graph of normalised scatter profiles

Once the scatter profiles had been normalised to the coherent scatter cross section the profiles were peak fitted for a second time. If the adipose to fibrous ratio had changed the normalisation process was repeated until the value did not change with any more iteration. The normalised scatter profiles for each tissue type are presented in the next chapter.

5.4 Summary

A measurement was made of the coherent scatter profile of each tissue type, using an energy dispersive method in the laboratory and an angular dispersive method at the Daresbury and ESRF synchrotrons. A number of corrections were applied to the data to convert the number of counts into a coherent scattering coefficient. A novel normalisation technique was developed, which uses the electron density values for each sample, measured during the first part of this study. The results of these measurements have been analysed using a method of fitting peaks to the scatter profiles, which is presented in chapter 6.

Chapter 6 Scatter profile measurement results and analysis

6.1 Introduction

The aim of these measurements was to see if it is possible to distinguish between tissue types using coherent scatter profiles. The profiles obtained were measured during four experimental runs, using two different techniques. Although the results have been extensively corrected for any experimental variation it will become evident upon examination of the results that it is extremely difficult to account for all experimental parameters, such as differences in detector efficiency and resolution and geometrical effects. This does not matter when comparing tissue types with a single set of measurements, but when combining different sets of results any subtle differences may be masked by the system differences.

The results were obtained using the theory outlined in section 5.2 and the methods described in section 5.3. The results are presented in section 6.2, with analysis and statistical analysis in section 6.3. A discussion of the results is included in section 6.4. As with the electron density measurements the samples used during the second run in the laboratory were taken to the ESRF synchrotron. These results therefore cannot be regarded as independent and are analysed separately in section 6.4. Conclusions are included in the final chapter (Chapter 8)

6.2 Scatter profile measurement results

Figures 6.1 to 6.4 present the measured scattering profiles in terms of σ_{coh} for all samples. The results for each measurement run are presented separately

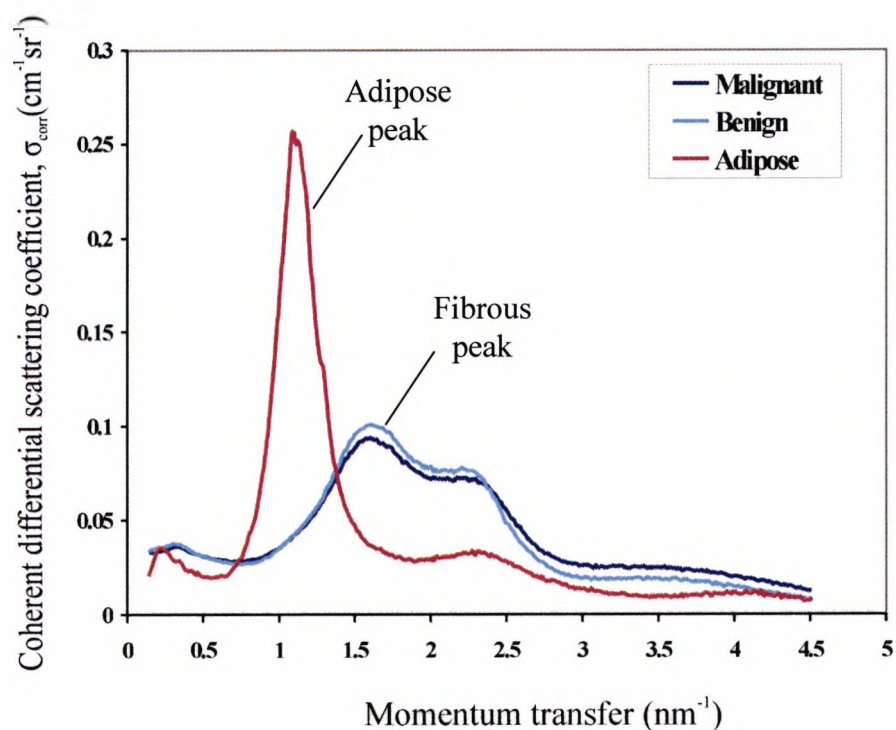


Figure 6.1 Scatter profiles from Daresbury SRS

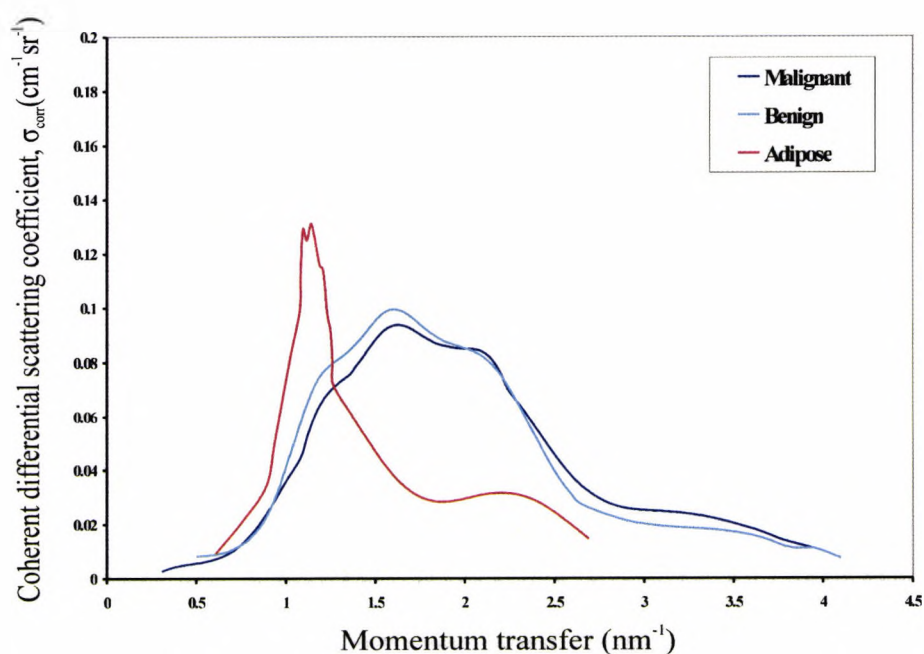


Figure 6.2 The scatter profiles obtained in the laboratory during the first run of experiments

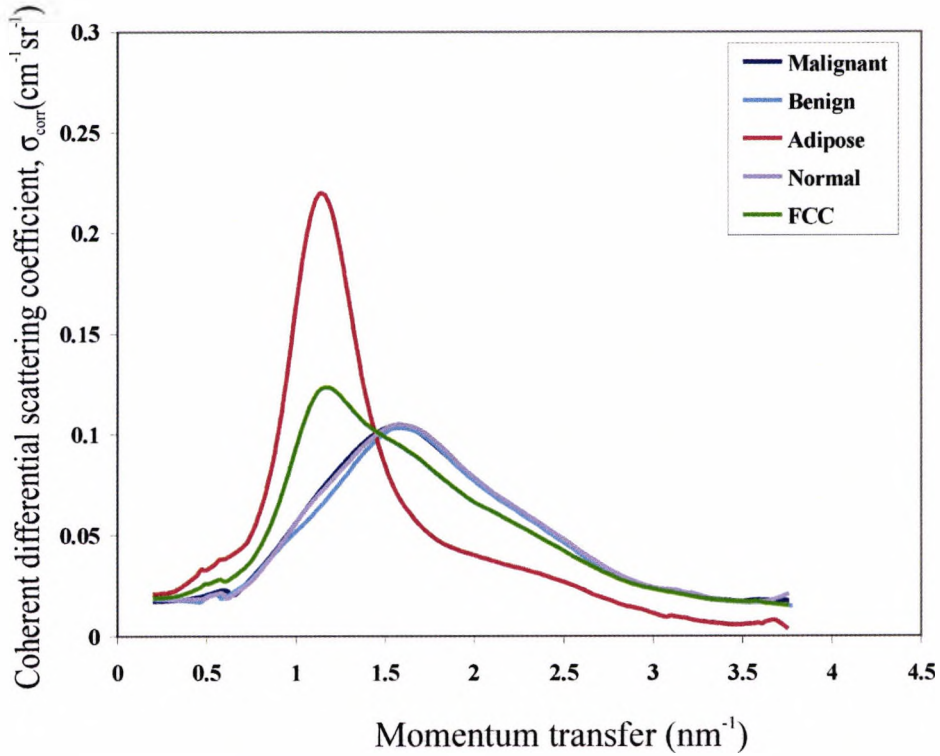


Figure 6.3 Scatter profile obtained in the laboratory during the second run of experiments

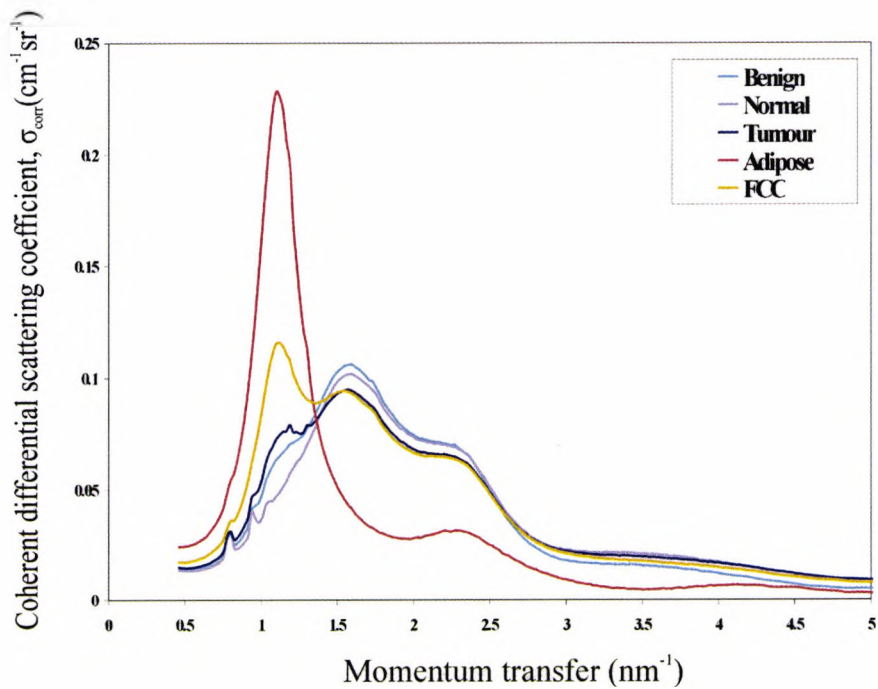


Figure 6.4 Scatter profiles obtained at the ESRF

Each set of experimental results are displayed separately. The four sets of measurement for each tissue type are displayed together in figures 6.5 to 6.7. There were differences in set-up which have not been accounted for in the measurement

corrections. The difference in geometry has not been accounted for, apart from the difference in sample thickness and the sample holder. Any other geometrical factors, such as loss in flux due to divergence of the beam and attenuation in air are not accounted for. In addition to this each detector has a unique efficiency and energy resolution. Figure 6.6, displaying each measurement of fibrous tissue, shows clearly the resolution on the second run of experiments in the laboratory to be worse than the first, due to the use of a different detector.

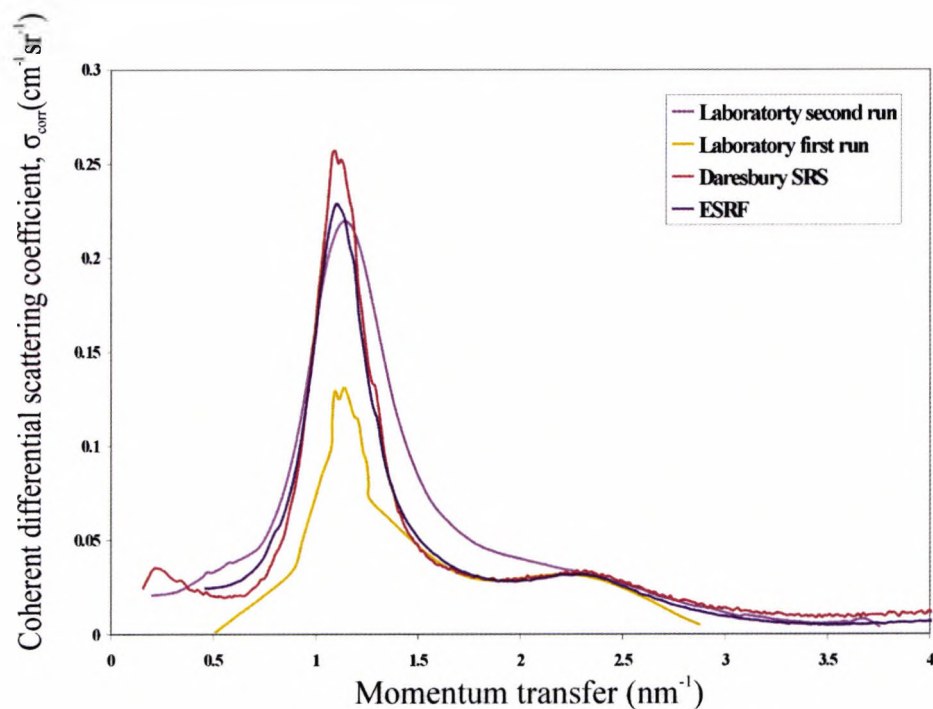


Figure 6.5 A comparison of adipose tissue spectra

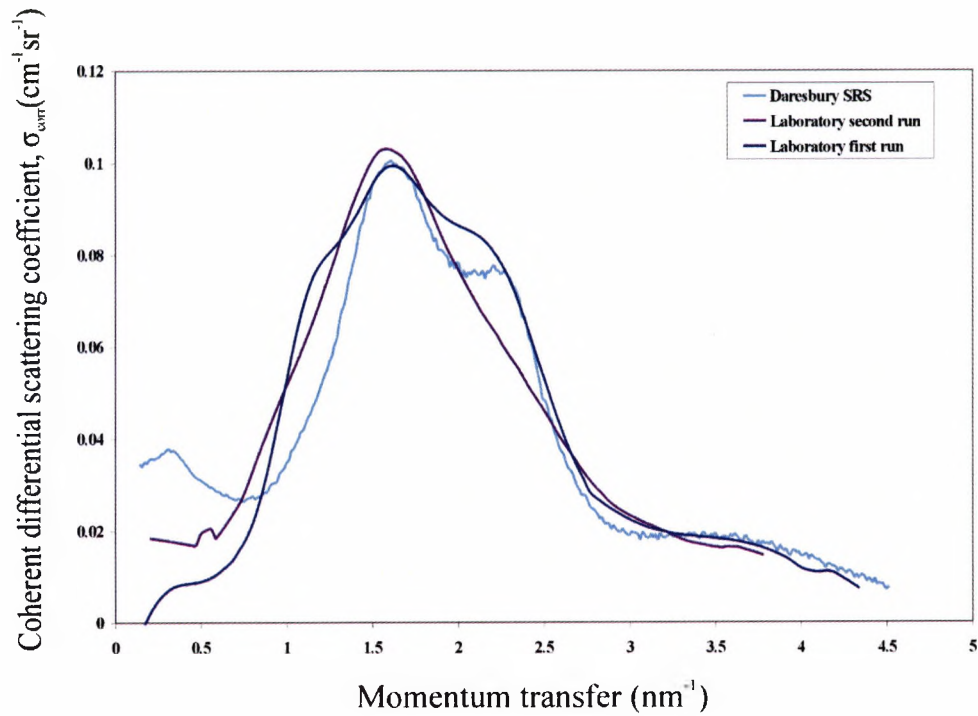


Figure 6.6 A comparison of benign tissue spectra

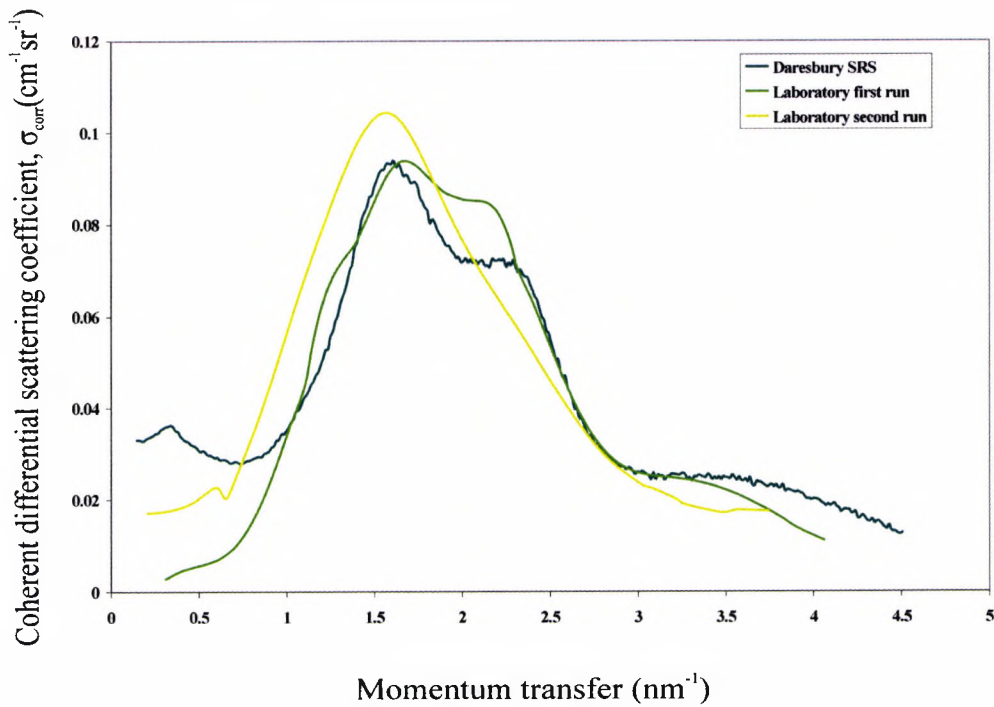


Figure 6.7 A comparison of malignant tissue spectra

6.3. Analysis

6.3.1 Introduction

For data analysis purposes both of the laboratory experiments and the Daresbury experiments are combined into a single data set. It can be seen from the results that the adipose tissue scattering profile is easily distinguishable from the other two tissue types (figure 6.5). This is the well documented pattern that arises from pure fat tissue, and is what is expected with a peak at 1.1nm^{-1} . The spectra from the laboratory first run shows the effects of the x-ray tube profile. This was corrected for during the analysis of the spectra. The other tissue types also demonstrate a familiar scatter profile with a much broader peak than adipose tissue at 1.6nm^{-1} , (figures 6.6 and 6.7) similar to the peak found from water. Adipose tissue has a much sharper peak due to the more ordered structure of the tissue. This has been found by other groups who have investigated fibrous tissue (Kidane *et al* 1999; Poletti *et al* 2002). It is harder to identify any strong differences between the benign and malignant tissue types. All tissues display a peaked distribution, oscillating to a smooth profile at large momentum transfer values. The oscillating pattern is the diffraction effects and the tail is scatter from free atoms, as in the Independent Atomic Model (IAM).

In order to be able to analyse the differences between tissue types a further method of deconvolving the spectra into Gaussian peaks was employed. The model used was determined from firstly fitting the adipose and fibrous peaks which are expected to be present in the data at well defined momentum transfer values. The remaining peaks were fitted empirically with the resulting peaks giving a good fit for the measured spectra. The peak fitting model and technique was described in section 5.3.3.3.

6.3.2 Deconvolution of spectra

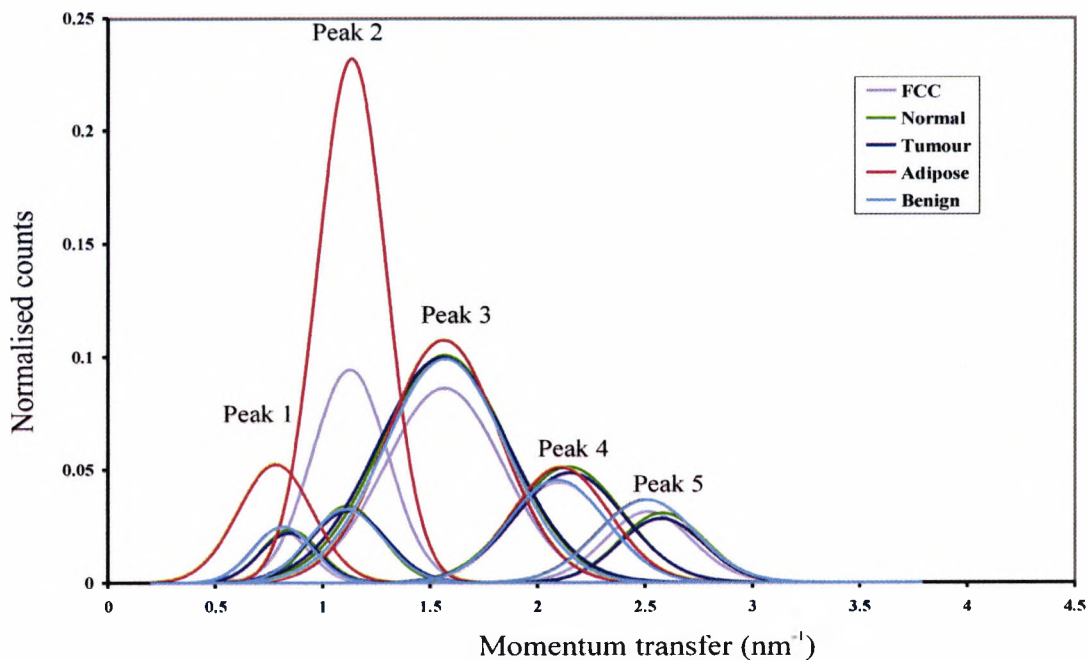


Figure 6.8 The average deconvolved peaks of the scatter profiles

The results from the peak fitting process are shown in figure 6.8. The Gaussian peaks that were found each have four parameters associated with them, the amplitude, centre, Full Width Half Maximum (FWHM) and area. These parameters have been displayed in table 6.1 It can be seen from this table that the first peak is similar for each tissue, except the amplitude is slightly higher for the adipose tissue. Peak 2 shows the biggest difference between the tissues, with the adipose and FCC tissues having a much larger amplitude and area. The FWHM is similar for all tissues. Peaks 3, 4 and 5 are very similar for all the tissues types except adipose which has a smaller area and amplitude for each of these peaks.

| Peak | | Malignant | Adipose | Benign | FCC | Normal |
|------|-------------|---------------|---------------|---------------|---------------|---------------|
| 1 | Amplitude | 0.020 | 0.047 | 0.019 | 0.024 | 0.023 |
| | Centre | 0.85 | 0.79 | 0.83 | 0.78 | 0.85 |
| | FWHM | 0.318 | 0.355 | 0.309 | 0.296 | 0.319 |
| | Area | 0.0069 | 0.0189 | 0.0064 | 0.0077 | 0.0079 |
| 2 | Amplitude | 0.034 | 0.162 | 0.035 | 0.100 | 0.035 |
| | Centre | 1.14 | 1.12 | 1.12 | 1.13 | 1.12 |
| | FWHM | 0.356 | 0.306 | 0.344 | 0.423 | 0.371 |
| | Area | 0.0133 | 0.0560 | 0.0129 | 0.0449 | 0.0137 |
| 3 | Amplitude | 0.094 | 0.067 | 0.098 | 0.089 | 0.101 |
| | Centre | 1.58 | 1.57 | 1.58 | 1.57 | 1.57 |
| | FWHM | 0.682 | 0.608 | 0.657 | 0.637 | 0.699 |
| | Area | 0.0685 | 0.0437 | 0.0683 | 0.0608 | 0.0749 |
| 4 | Amplitude | 0.057 | 0.038 | 0.059 | 0.046 | 0.051 |
| | Centre | 2.15 | 2.10 | 2.14 | 2.10 | 2.14 |
| | FWHM | 0.537 | 0.530 | 0.541 | 0.534 | 0.592 |
| | Area | 0.0321 | 0.0217 | 0.0340 | 0.0260 | 0.0323 |
| 5 | Amplitude | 0.031 | 0.021 | 0.025 | 0.032 | 0.031 |
| | Centre | 2.56 | 2.50 | 2.54 | 2.52 | 2.58 |
| | FWHM | 0.461 | 0.451 | 0.458 | 0.484 | 0.465 |
| | Area | 0.0156 | 0.0115 | 0.0128 | 0.0167 | 0.0152 |

Table 6.1 Parameters of the 5 peaks in the fitting model

6.3.3 Statistical analysis

The aim of these experiments was to examine whether the diffraction profile of different tissue types could be used to distinguish between them. From looking at figure 6.8 it can be seen that the adipose peaks differ from the others but it is not possible to see any differences between the fibrous tissue types. In order to get a better idea of whether any of the parameters in table 6.1 are significantly different a Kruskal-Wallis test has been applied to each parameter in turn. Dunn's post hoc test has then been applied to each combination of tissue types. This produces a P value which must be low for there to be any significance. The results of this analysis have been displayed in table 6.2. In this table any significance produced for a pair of samples has been graded as 1 for quite significant, 2 for significant and 3 for very significant.

Table 6.2 shows that only the adipose and FCC tissues can be distinguished from the others. Peak 2 produced the greatest difference and peak 3 did not produce any.

| | Peak 1 | | Peak 2 | | Peak 3 | | Peak 4 | | Peak 5 | |
|------------------|--------|-----------|--------|-----------|--------|-----------|--------|-----------|--------|-----------|
| | Amp | FWHM Area |
| Tumour v Adipose | 3 | 1 | 3 | 3 | | | 3 | 2 | 3 | 3 |
| Tumour v Benign | | | | | | | | | | |
| Tumour v Normal | | | | | | | | | | 1 |
| Tumour v FCC | | | 3 | 1 | 3 | | | | | |
| Adipose v Benign | 3 | 1 | 3 | 3 | | | 2 | 1 | 2 | 3 |
| Adipose v Normal | | | 3 | 2 | | | 2 | 3 | 3 | 1 |
| Adipose v FCC | | | | 2 | | | | | | |
| Benign v Normal | | | | | | | | | | 2 |
| Benign v FCC | | | 2 | 2 | 2 | | | | | 1 |
| Normal v FCC | | | 1 | 1 | | | | | | 2 |

Table 6.2 Peak analysis results

In table 6.2: 1 – Quite significant (P<0.05) 2 – Significant (P<0.01) 3 – Very significant (P<0.001). All comparisons not showing a number were performed but were found to be not significant (P>0.05).

6.3.4 Analysis of ESRF results

The results from the ESRF synchrotron experiments were analysed in the same way. The statistical analysis did not produce any significant differences because the sample sizes were too small. The results broadly agree with the main set of results, however visually it can be seen that the benign peaks 3 and 4 appear larger than the other fibrous tissue types. This may be a real difference, or it may be a result of the measurement system, as this difference was not evident in the lab. However, if the ADXRD measurements are more accurate this indicates that a difference may be present.

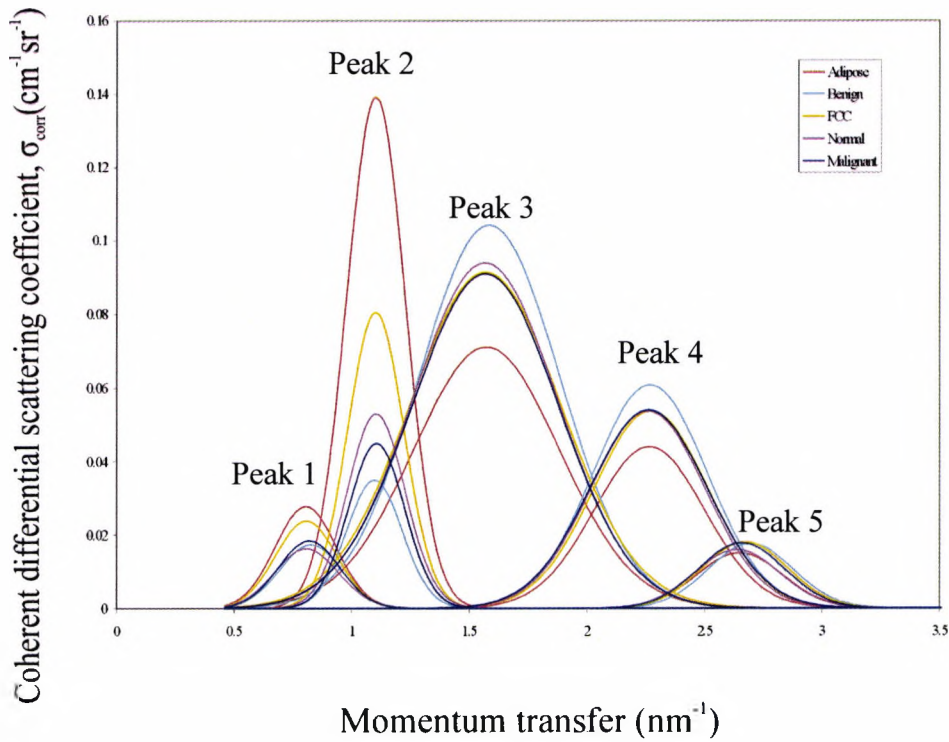


Figure 6.9 The deconvolved peaks from the ESRF spectra

| Peak | | Malignant | Adipose | Benign | FCC | Normal |
|------|-----------|---------------|---------------|---------------|---------------|---------------|
| 1 | Amplitude | 0.018 | 0.027 | 0.018 | 0.024 | 0.017 |
| | Centre | 0.82 | 0.81 | 0.83 | 0.81 | 0.81 |
| | FWHM | 0.303 | 0.274 | 0.298 | 0.303 | 0.307 |
| | Area | 0.0059 | 0.0075 | 0.0057 | 0.0077 | 0.0055 |
| 2 | Amplitude | 0.042 | 0.131 | 0.035 | 0.081 | 0.054 |
| | Centre | 1.10 | 1.10 | 1.09 | 1.10 | 1.09 |
| | FWHM | 0.268 | 0.289 | 0.265 | 0.278 | 0.276 |
| | Area | 0.0125 | 0.0411 | 0.0103 | 0.0242 | 0.0164 |
| 3 | Amplitude | 0.093 | 0.075 | 0.104 | 0.092 | 0.094 |
| | Centre | 1.57 | 1.57 | 1.58 | 1.57 | 1.56 |
| | FWHM | 0.735 | 0.687 | 0.703 | 0.753 | 0.725 |
| | Area | 0.0727 | 0.0574 | 0.0781 | 0.0737 | 0.0728 |
| 4 | Amplitude | 0.055 | 0.045 | 0.061 | 0.054 | 0.054 |
| | Centre | 2.26 | 2.22 | 2.27 | 2.27 | 2.26 |
| | FWHM | 0.589 | 0.544 | 0.570 | 0.566 | 0.573 |
| | Area | 0.0347 | 0.0264 | 0.0370 | 0.0329 | 0.0327 |
| 5 | Amplitude | 0.018 | 0.018 | 0.018 | 0.018 | 0.016 |
| | Centre | 2.66 | 2.62 | 2.70 | 2.67 | 2.64 |
| | FWHM | 0.423 | 0.450 | 0.418 | 0.423 | 0.423 |
| | Area | 0.0080 | 0.0080 | 0.0079 | 0.0082 | 0.0072 |

Table 6.3 The results from the ESRF spectra peak fitting analysis

6.4 Discussion

The results have been compared to those obtained previously by other groups. This is shown in figures 6.10 and 6.11. It can be seen that the results found for adipose tissue compare extremely well to other studies. The fibrous results do not compare as well but still demonstrate a similar pattern. The results from the ESRF measurements showed a slight difference between the benign and other types of tissue, with the benign peaks being slightly higher. This suggests that there may be some more subtle differences but using the three data sets combined together may have masked these differences with system differences. There were not enough results in any single set of measurements to analyse separately. The results are analysed in the next chapter using a multivariate analysis technique. This looks at trends of data as a whole, rather than each parameter on its own and is a better technique for analysing spectral data of this kind.

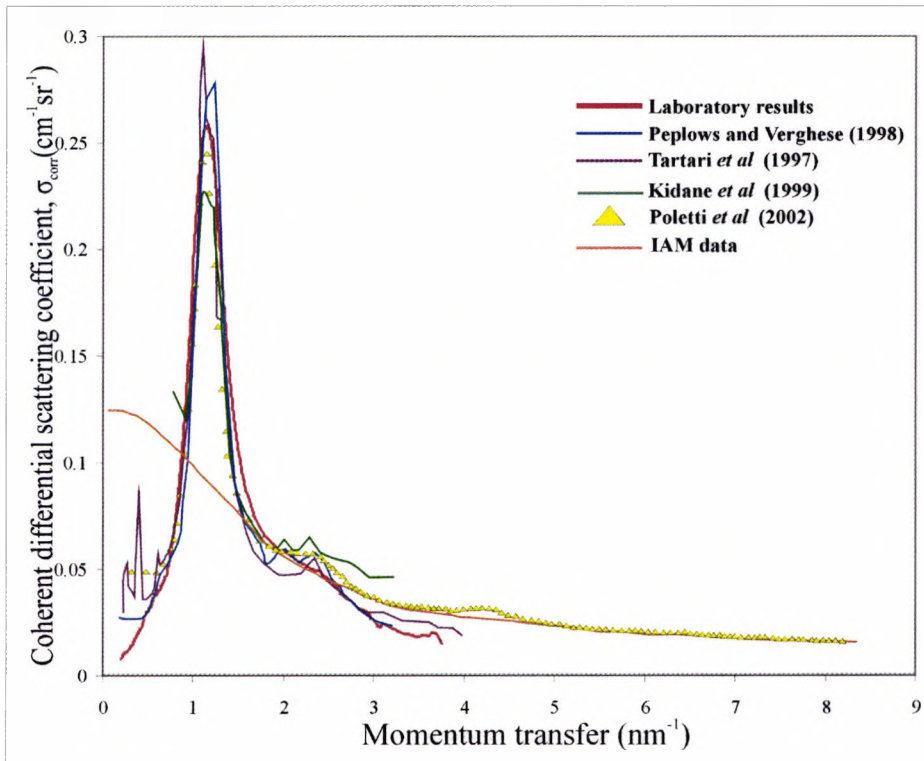


Figure 6.10 A comparison of the results to previous studies for adipose tissue

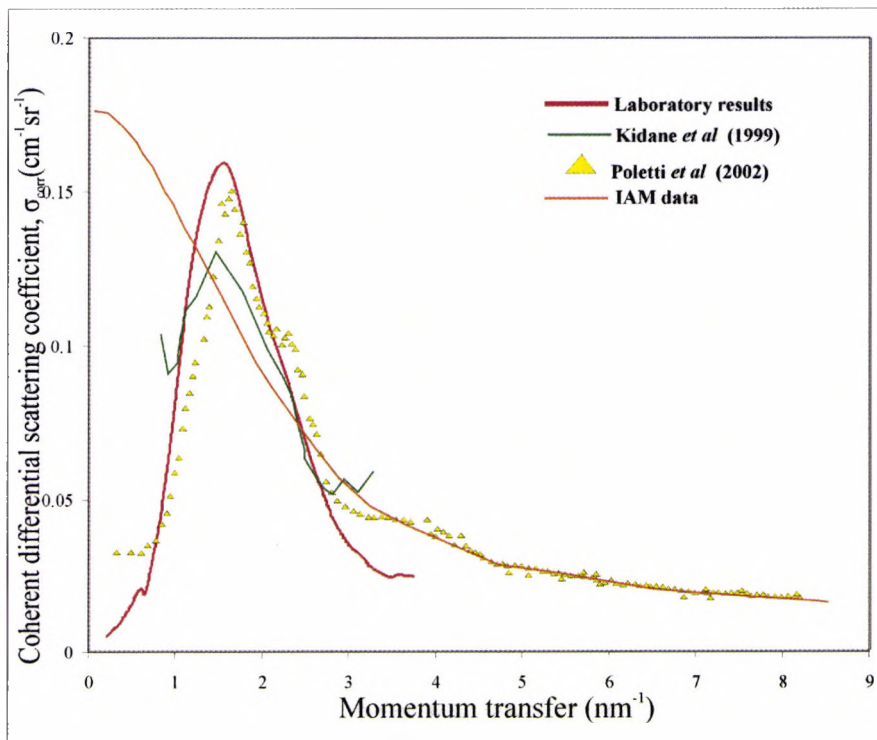


Figure 6.11 A comparison of the results to previous studies for fibrous tissue

6.5 Summary

The results of these measurements were analysed using a method of fitting peaks to the scatter profiles and deconvolving them into a set of 5 peaks. The areas, amplitudes and Full Width at Half Maximum (FWHM) of all the peaks obtained for each tissue type were compared using a Kruskal-Wallis analysis of variance test. Adipose and FCC tissues were easily differentiated from the other tissues. No substantial differences were found between the fibrous tissue types. The profiles obtained from the ESRF were also analysed in the same way, but no conclusive differentiation could be found, due to the small sample size. The results were compared to those found by previous studies and were found to agree well.

Chapter 7 Multivariate data analysis combining electron density and scatter profile results

7.1 Introduction

The results obtained from the Compton and coherent scatter measurements have generated a large data set for each sample, particularly the scatter profile analysis. In the chapters so far each measurement set has been compared using one variable at a time. It is difficult to try and assess whether samples can be classified by looking at the value of variables individually, as these may well be interlinked. In order to fully interpret these results it is useful to be able to view the data set as a whole and this can be done through multivariate data analysis techniques. This is a technique that looks at all variables at one time and their correlation and is a powerful technique for finding hidden relationships within the data.

Multivariate analysis (MVA) is a technique which has proven very useful for the analysis of spectra due to its ability to handle large and complicated sets of data, picking out hidden relationships that are not apparent when looking at individual variables. The technique has been applied to infrared spectroscopy with a range of medical applications, two recent examples being prostate cell differentiation (German *et al.* 2006) and blood glucose monitoring (Maruo *et al.* 2006). This method has also been used for quantitative analysis of EDXRD spectra. Farquharson *et al.* (1997) used MVA on spectra of bone phantoms. This study showed that a multivariate data analysis technique is a powerful technique for diffraction data. MVA has been used for the analysis of breast tissue measurement parameters by Farquharson and Geraki (2004a) who combined XRF and EDXRD results as variables to classify normal and malignant breast tissue samples.

A technique of principal component analysis and soft independent modelling is used to formulate a model with which to classify unknown tissue samples. The aim of this chapter is to see whether Soft Independent Modelling of Class Analogies (SIMCA) can improve on the classification of tissue samples that has been possible when

looking at the electron density data and adipose to fibrous ratios separately. A number of models were used when refining the technique until an optimal model was found.

Descriptions of Principal Component Analysis (PCA) and the Soft Independent Modelling of Class Analogies (SIMCA) technique are given in section 7.2 The methodology used in order to formulate and test the classification models is described in section 7.3 A summary of the models used and an analysis of how effective each one was at tissue discrimination is given in section 7.4.

7.2 Background

7.2.1 Principal component analysis (PCA)

7.2.1.1 Introduction

Principal component analysis is a mathematical transformation of data from a data matrix, described by variables which are related to the measurements used to generate these data, into a matrix in principal component (PC) space. If the original data set has p variables this can then be plotted in PC space with P dimensions. PCA is a method of re-plotting the data onto a new set of orthogonal axes, determined by any correlations within the original data. The principal axis is the line of best fit or least squares fit drawn through the direction of maximum variance. This axis is a trend line which is a linear combination of the original data variables, some of which have a greater influence than others.

The second principal axis is found orthogonal to this which describes the next greatest variation in data. This is repeated as many times as is necessary until an orthogonal set of axes have been constructed which completely describes the variance of the data set. Figure 7.1 illustrates the first two principal components of a data set.

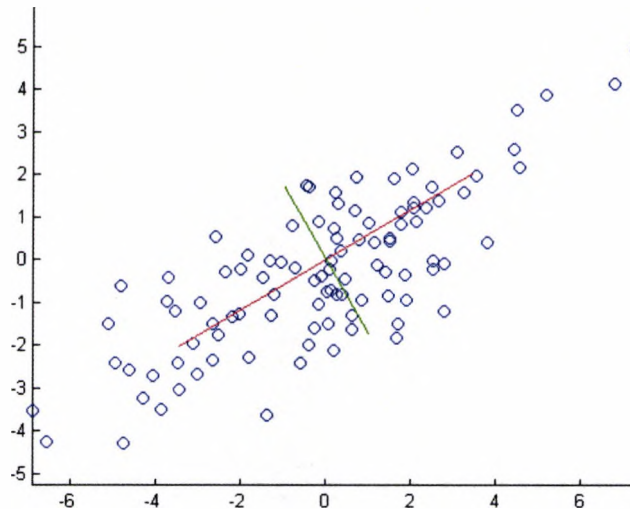


Figure 7.1 The first two Principal Components of a set of data

The origin of the PC is the mean value of each variable. In practice the mean value is subtracted from each variable data point and the centre of the axes is the point at which all variables are equal to zero.

Mathematically the process of describing the data using principal components is simply a rotation of the original data matrix to describe the direction of greatest variance. The data are also translated to the new origin.

7.2.1.2 Score plots

A score plot is used to visualise the data. It is a projection of the data matrix onto the plane formed by each pair of PC axes. The first score plot is the projection of the data onto the PC1 and PC2 axes and illustrates the largest variance patterns in the data. Each pair of axes can be viewed in turn, enabling an idea of the overall layout of the data. The score plot shows the co-ordinate of each data point in PC space.

7.2.1.3 Loadings

A loadings plot shows the influence that each variable has on the principal components. It complements the score plot in adding the information of how the original data corresponds to the PC space and it gives a visual interpretation of why each data point on the score plot is positioned where it is.

7.2.1.4 Residual variance

The residual variance describes how much of the variance in the data is described by each principal component and therefore indicates how many principal components should be used to adequately describe the data. It is useful in avoiding the use of too many principal components in the model, as high principal components are usually relate to noise rather than signal and inclusion of too many PCs may reduce the effectiveness of the model.

7.2.2 Soft Independent Modelling of Class Analogies (SIMCA)

7.2.2.1 Introduction

The use of soft modelling is to study complex systems where it is not practical or possible to vary single parameters at one time but it is more likely that one data set will have multiple dimensions rather than just one. Soft modelling is based on the principal that a class of samples or objects do not have a set of identical results for a number of different measurements but they will have a mean and standard deviation for each parameter. The covariance between these parameters may show up hidden differences between classes which are not apparent when hard modelling single parameters individually. The results can be assessed using a number of available tools.

The SIMCA system places all of the available models and plots them back into a common set of axes. By then plotting each new sample using these common axes the classification model can deduce which class it is closest to. This is illustrated in figure 7.2 which shows a set of common axes with two PCA results combined as classes in this model.

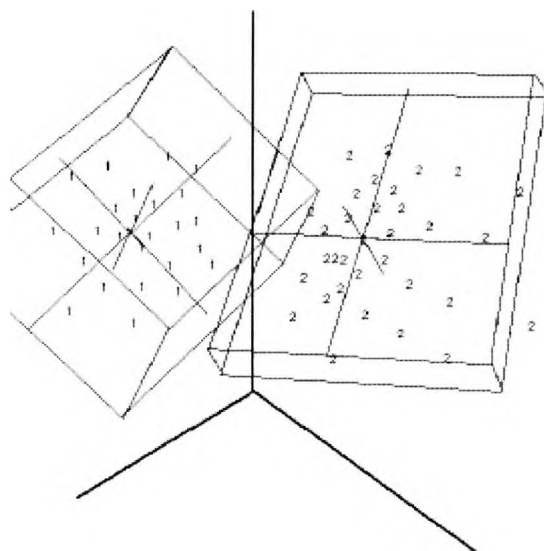


Figure 7.2 An illustration of a set of axes in a SIMCA model with two PCAs as classes

The software used was The Unscrambler, (CAMO ASA) which performs multivariate data analysis and displays the data computation results in a multi-screen format to allow for the examination of an overview of different aspects of the results simultaneously. It has the ability to perform covariance and regression analysis using a number of methods, however the only available functions applicable to this work was the PCA and SIMCA classification facilities and so none of the other techniques are described here.

7.3 Method

In order to be able to assess the classification model a test set of tissues is needed. This is a group of samples that have not been included in the original modelling process. They should have a known classification so that they can be used to establish whether the correct classification has been made. The next step on from this is to blind test samples of unknown classifications. This has not been performed on this data set due to the small number of samples available. Ten samples were chosen at random to be a test set. Due to the small sample numbers available the samples were 1 FCC, 1 normal, 2 adipose and 3 malignant and benign samples.

The data from all the remaining samples were compiled into a data set with 18 dimensions. These were

- The peak amplitude and area for all 5 measured wide angle scattering peaks. The centre position and FWHM were also recorded but were excluded as they were deemed not to carry any useful information.
- The peak area as a percentage of the total number of counts in the WAXS spectrum for each of the five peaks
- The electron density measurement
- The adipose-fibrous ratio
- The factor D found in section 5.3.3.3, which is representative of the percentage of fibrous tissue present in the sample

Principal component analysis was carried out on each tissue class. The set of PCA results were then combined into a model and this was used to interrogate the test set data and to classify the samples into one of the classes. In practice the number of variables included in the model can be altered to yield better results. Some variables will contain noise rather than information as they do not show similarities between one class and differences with another. With this in mind the classification model can be refined and repeated. When the test set is presented to the model the software outputs a classification for each test sample. This may be either a single class, a number of classes, from 2 up to all of the classes or none of the classes. and there are also a number of tools available within the software to assist with interpreting the classification results. These will be described in more detail in the following section. These Unscrambler tools are useful in assessing the quality of each model but inter-comparison between models is not possible in a quantitative manner. For this purpose a scoring method was developed based on how well the samples were correctly classified.

Firstly an initial classification model was formulated with all available data variables. This model was assessed using the evaluation tools described below. A second model was then formed with a reduced number of variables and tested again. The results of this second model were then compared to the first using a scoring system. This model was also studied and evaluated. All of this information was then used to reassess and

improve the variables included in the model. This was repeated a number of times, each time trying to improve the predictive ability of the classification model. In total 9 models were tested until it was deemed that the optimum model had been designed. A description and summary of each model and its classification effectiveness is given in the following section.

7.4 Results and analysis

7.4.1 Principal component analysis

The strength of this type of data analysis is being able to examine a large amount of data in a convenient format. The results of a PCA are displayed in score plots, which are a projection of each pair of axes onto a 2-D plane. These are complemented by a loading plot which provides information as to which aspects of the data are represented by each PC. Therefore for a PCA which contains 4 principal components will have a series of 6 score plots and loading plots which all provide information. In total there are five PCA models (one for each tissue type) which are used in the classification model. Therefore the score and loading plots for the PC1 and PC2 plane only for a single model are displayed and interpreted for illustrative purposes. The remaining PC combination graphs are not included. Figures 7.3a and b show the output after performing a PCA on the set of adipose data variables. The results from the data from the first run of experiments in the laboratory are labelled 'Laboratory 1' and the results from the second set of experiments in the laboratory are labelled 'Laboratory 2'. The results from the ESRF have not been included as they are not independent and would unfairly bias the models.

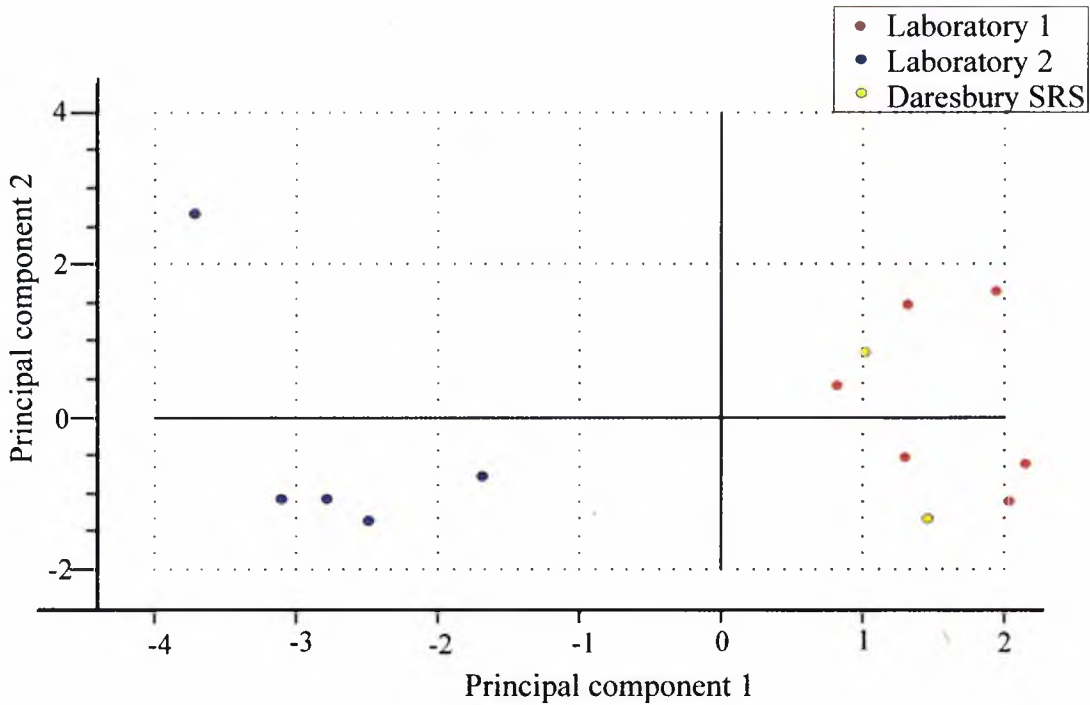


Figure 7.3a The scores plot obtained after performing a PCA

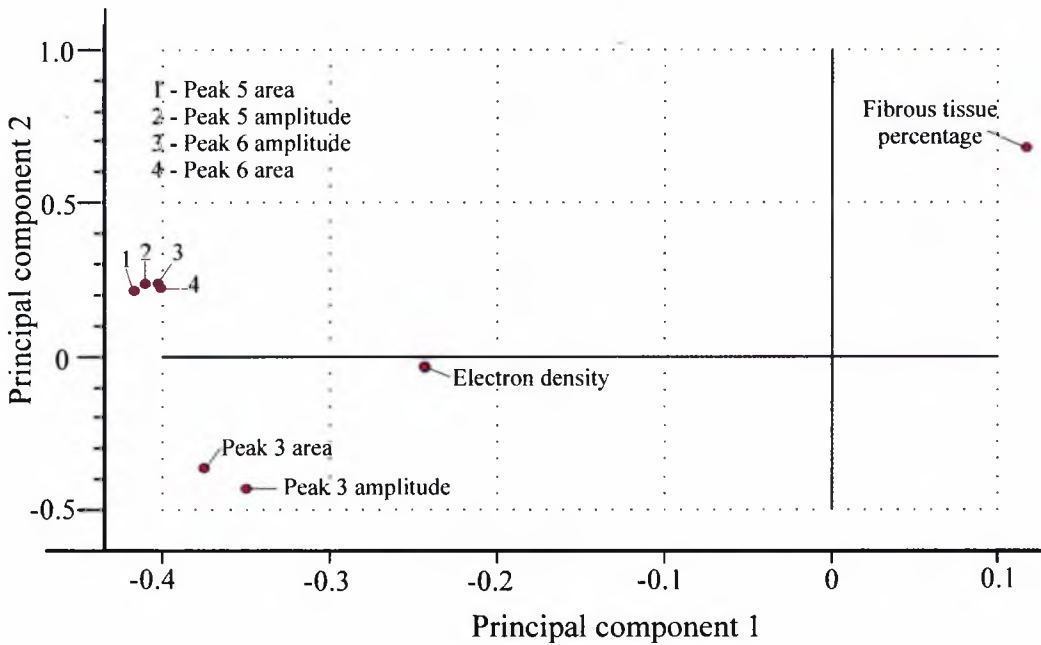


Figure 7.3b The loadings plot obtained after performing a PCA

The figure 7.3a shows the graphical display of the scores plot, showing the principal component (PC) 2 vs PC1 axes. This plot illustrates, through the different colours, the different sample sets taken during different sets of experiments. This is the principal component and so therefore this spread in data must be the largest variance. The

loadings plot in figure 7.3b shows that the spread across all the data is largely due to the electron density but this is not causing the grouping which is seen. The grouping of the different experiments is being caused by the peak area and amplitudes being different for the 'Laboratory 2' data set and the percentage of fibrous tissue influencing the rest of the data. This may be due to the measurement and normalisation of the scatter profiles, as this shows that the data processing has not produced identical data sets. However the PCA model should take this variation into account and so therefore allow for this variance within this class of samples when the overall classification model is formulated.

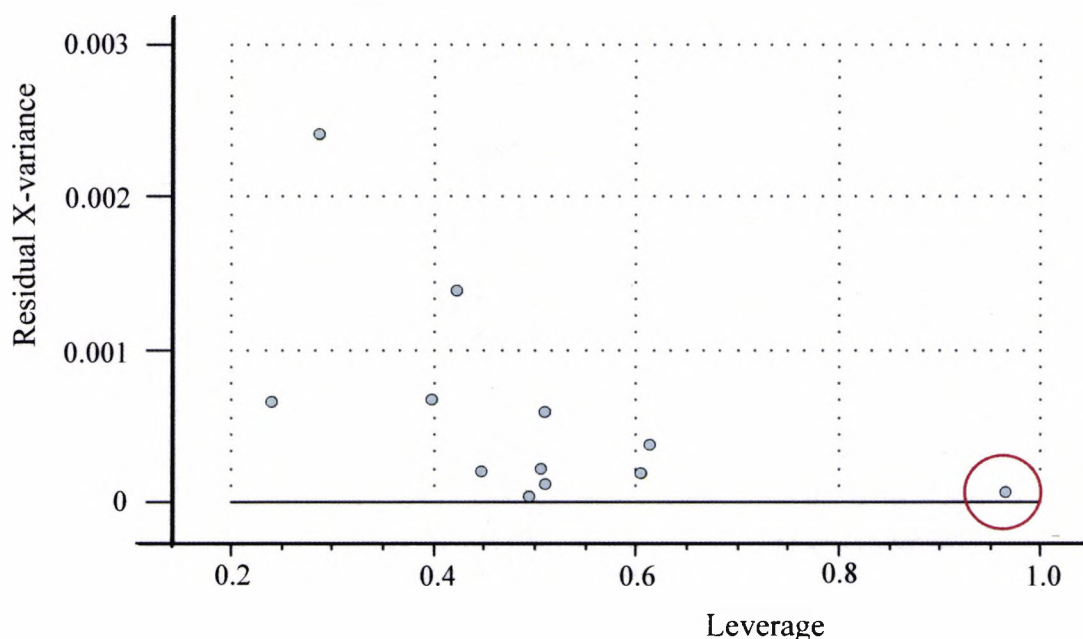


Figure 7.4 The influence plot for the adipose samples

The influence plot shows one sample that has the greatest influence on this PC, which is circled in red in figure 7.4. The samples with the highest leverage value have the greatest influence on where the principal components will lie. Examination of the data for this sample shows that it does have higher peak amplitudes and areas for each peak compared to the other adipose samples. This sample is not excluded from the data set for being an outlier as there are not enough samples to be able to say that this is a true outlier and so therefore it has been left in.

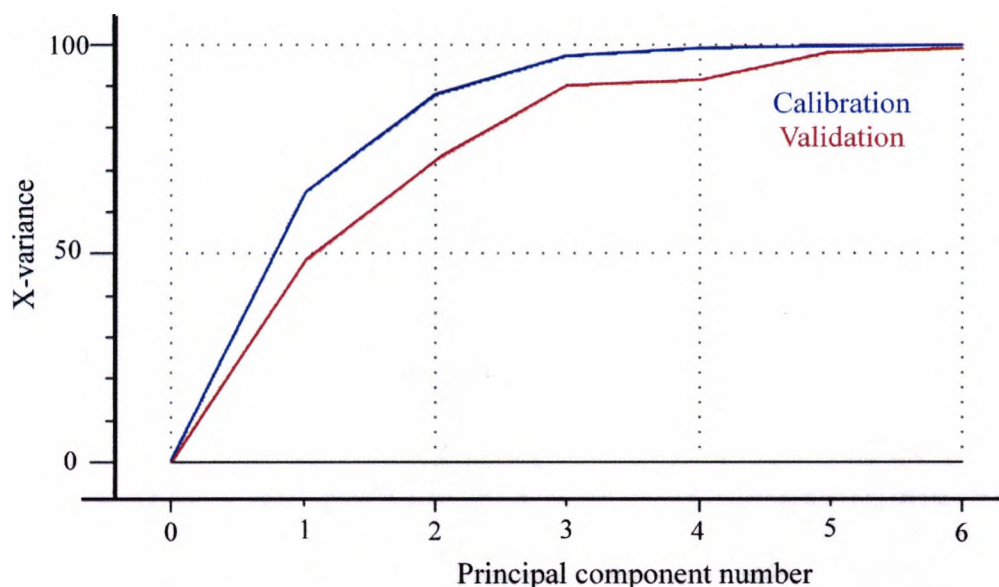


Figure 7.5 The explained variance plot for the adipose samples

The explained variance plot has one curve for the calibration samples and one for the validation samples, which is explained in the next section. The purpose of this plot is to show which principal component explains the variance seen in the data set. In figure 7.5 it can be seen that nearly 90% of the x-variance in the calibration samples is explained by the first two PCs. As previously stated the power of this technique is being able to view all combinations of PC score plots and loadings to get a feel for the data.

7.4.2 Validation

In order to test the validity of the model, or to be able to state how well it describes the data it must be tested on new data, which can then test the performance of the model. A 'test set' of new samples measured under the same conditions can be used for this purpose. If a test set is not practically viable due to the number of sample data available the next best method of validation can be used. This is a technique called cross validation which utilises a self test method. A model is produced using all of the samples except one. This sample is then used to as a test. The procedure is repeated leaving out a different sample each time until all the samples have been tested by these sub-models. This gives a measure of how well the model has performed and a validation curve, as shown in figure 7.5, can be viewed to assess the applicability of each PC to the model. This curve can also be used to detect outliers, which may cause the validation curve to dip.

7.4.3 Soft Modelling

7.4.3.1 Interpretation of classification results

There are several tools available within the software for assessing the classification results. In order to illustrate these, the model that gave the worst classification results (model 1) and the one that gave the best classification results (model 8) will be used as illustrative examples.

Coomans plots

Coomans plots show all the data from two classes plotted as a co-ordinate as distance from each of these two models. The vertical distance up the y-axis shows how far the sample is from the point of the 'FCC' PCA model origin (the point where all variables are the mean value). The distance of each sample along the x-axis shows how far it is from the origin of the 'normal' PCA model. Therefore if the model is good at distinguishing between these two tissue types all of the FCC samples should lie very close to the x-axis, but far away from the y-axis and vice versa for the normal samples.

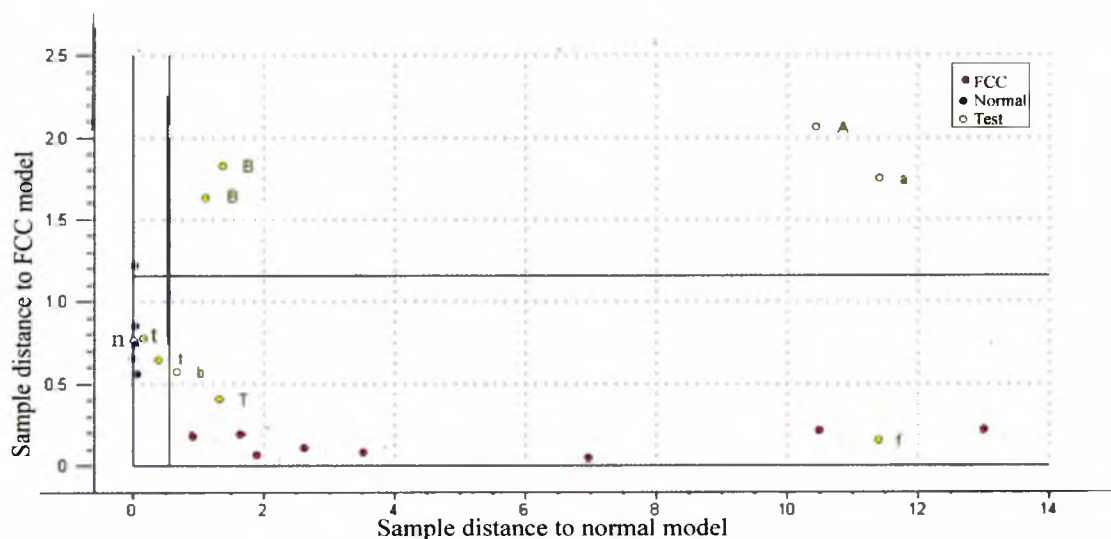


Figure 7.6a A Coomans plot to show the normal tissue compared with the FCC tissue for the worst model.

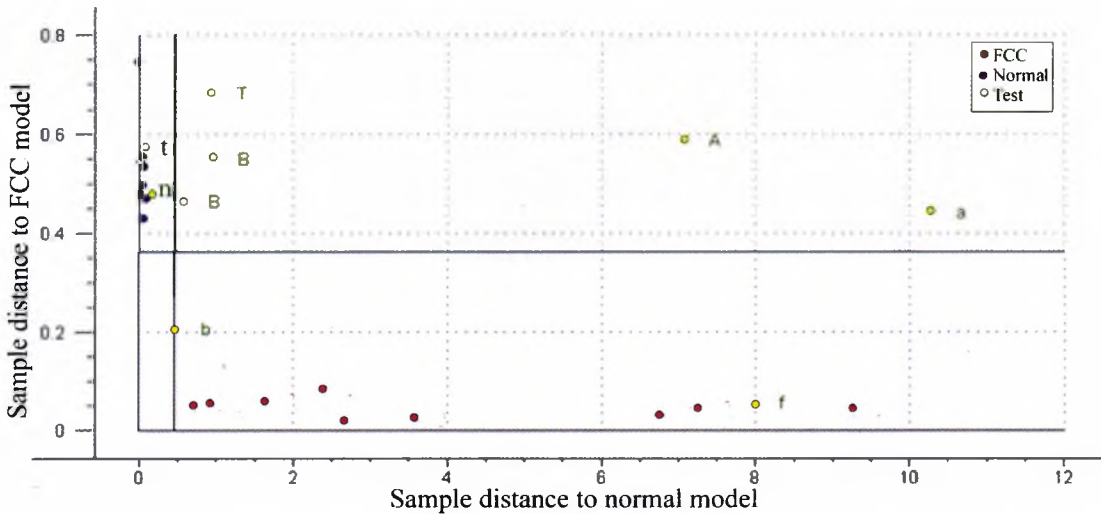


Figure 7.6b A Coomans plot to show the normal tissue compared with the FCC tissue for the best model.

In the Coomans plots shown in figure 7.6a and b the blue points are the normal samples and the red points are the FCC samples. The green points marked with mixed letters are the test samples and the bold lines show the 5% significance levels. It can be seen that the first model using all the sample parameters is not very good at distinguishing between these two tissue types because a large number of the normal samples lie in the area where the two models intersect, implying that they could belong to both models. The test samples which are neither FCC nor normal should lie in the top right hand section of the diagram as they belong to neither model, but in the first situation five out of the ten test samples are incorrectly placed within the FCC or both models. In the second diagram it can be seen that by remodelling with fewer variables the differentiation between these two models has improved. Now no samples are included in both models as the intersecting area is empty. All of the normal and FCC samples are correctly placed and seven out of the ten test samples are in the correct area.

Significance levels

It was stated in the previous section that the horizontal and vertical lines on the Coomans plot denote the 5% significance level. This significance level is the type I error rate, or the percentage of samples that are incorrectly placed outside the model when in fact they do belong to it. If the significance is increased then this increases the number of samples that will fall outside the model, even though they belong to it

but the criteria for belonging to that model are much stricter. This may also decrease the number of samples that are wrongly placed within that model (type II error rate) and it increases the discrimination power of the model as the overlapping area decreases. This is illustrated by figures 7.7a and b. The significance level has been increased from 5% in the top graph to 25% in the bottom graph. It can be seen that in this example that far fewer test samples are incorrectly placed in the adipose model and less of the FCC samples belong to both models. However this is not always the case and increasing the significance level may exclude a large number of true values from the model.

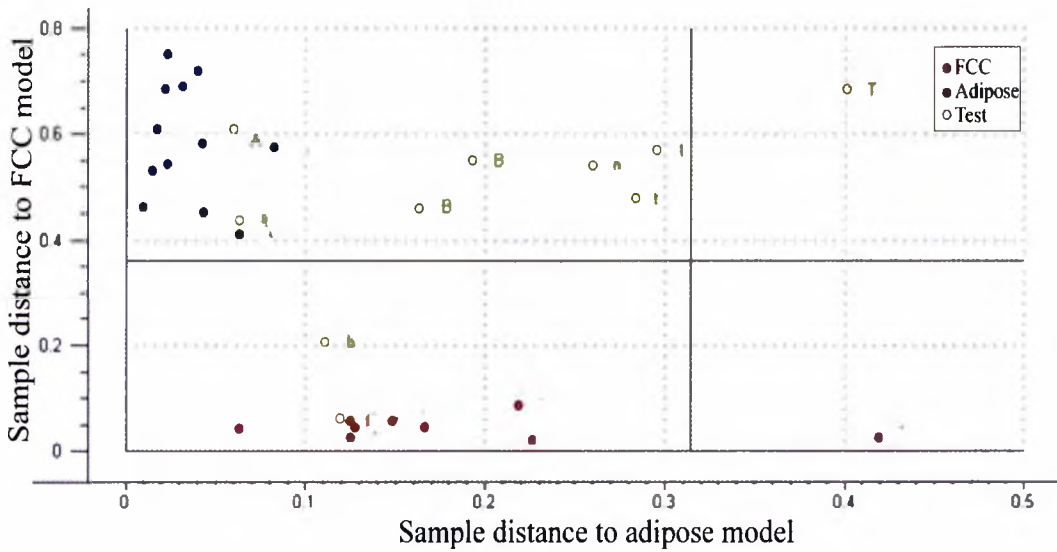


Figure 7.7a A plot with a significance level of 5%

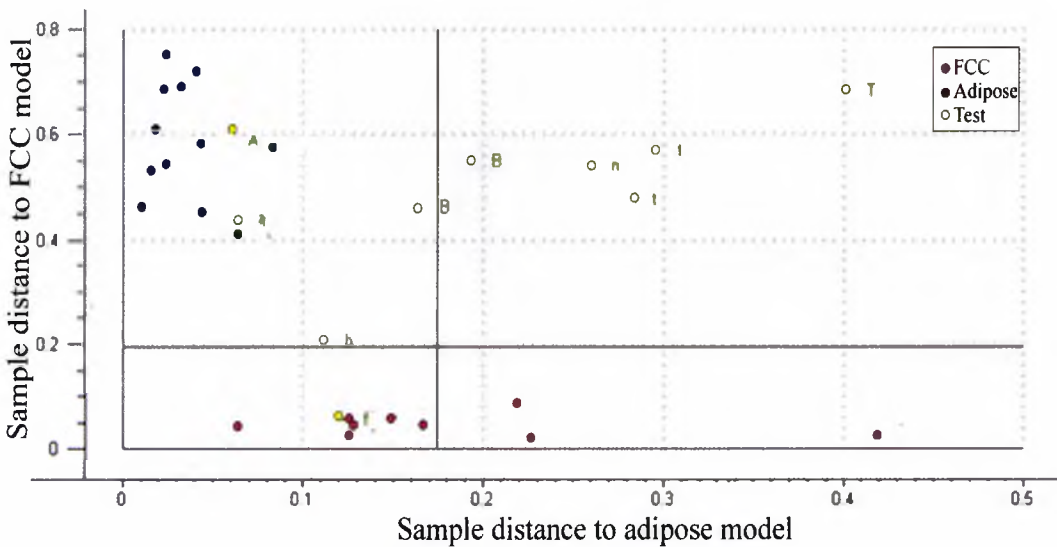


Figure 7.7b A plot with a significance level of 25%

S_i/S_0 vs H_i

These plots show how far away from a specified tissue model the test samples are. The plot has four quadrants and any sample that lies in the bottom left quadrant is considered close enough to the tissue class to be a member within the specified limits of significance. Test samples in the top right quadrant are considered not to be a member of the class in question. Figure 7.8 is a plot comparing the test set with the FCC classification. Figure 7.8a is the worst model. This shows that six samples have been considered to belong to the FCC class. Figure 7.8b is the best model. This shows that the improvement to the model now means that only one test sample, the FCC sample, has been allocated as a member of this class.

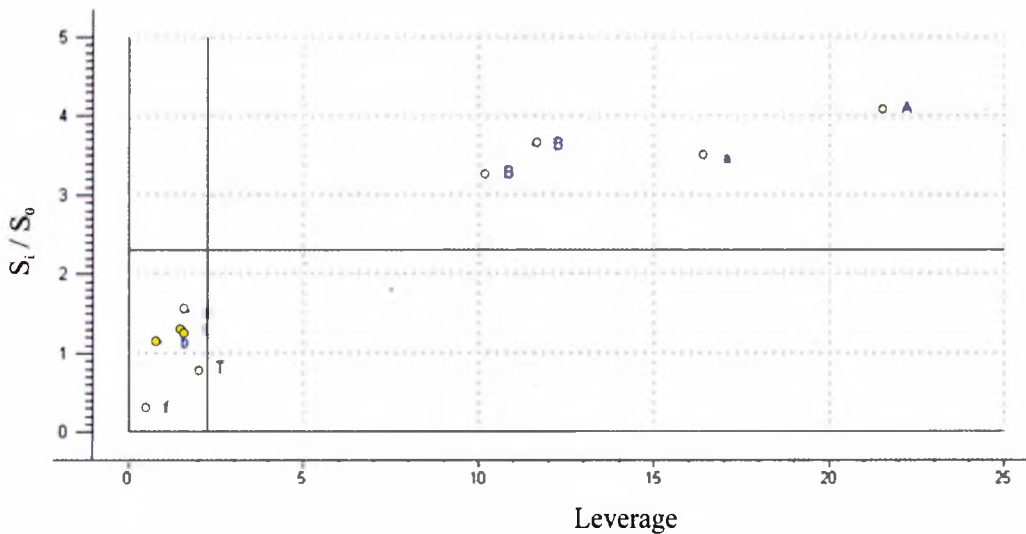


Figure 7.8a A S_i/S_0 vs H_i for the worst model

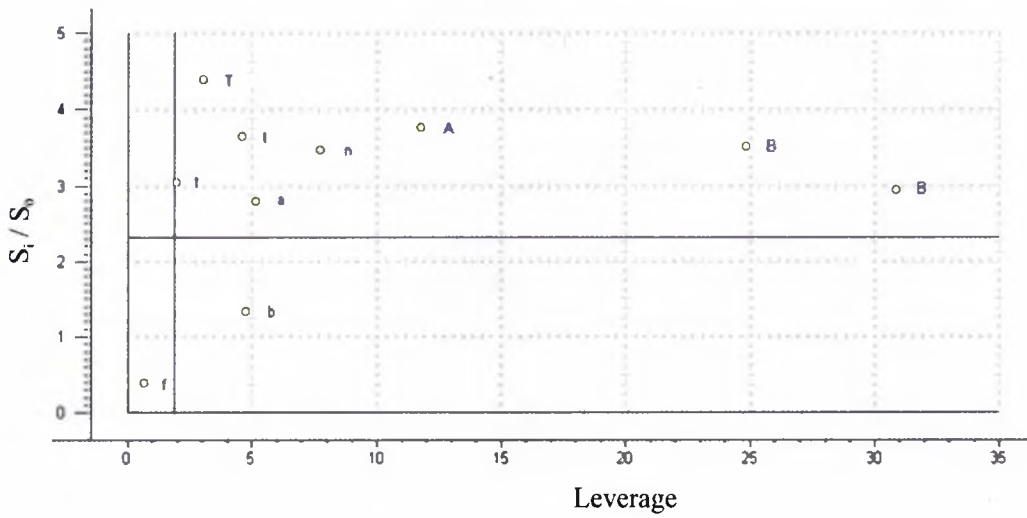


Figure 7.8b A S_i/S_0 vs H_i for the best model

Model distance

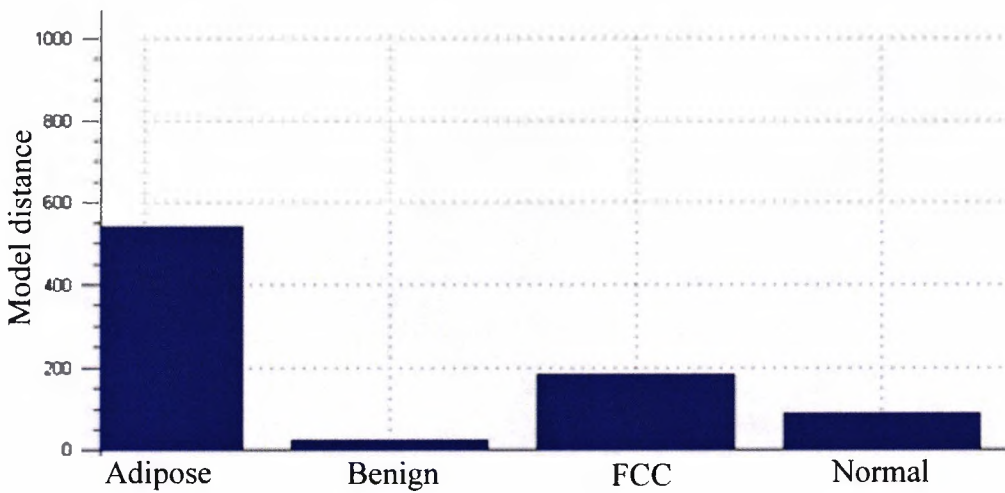


Figure 7.9a A model distance plot for the worst model

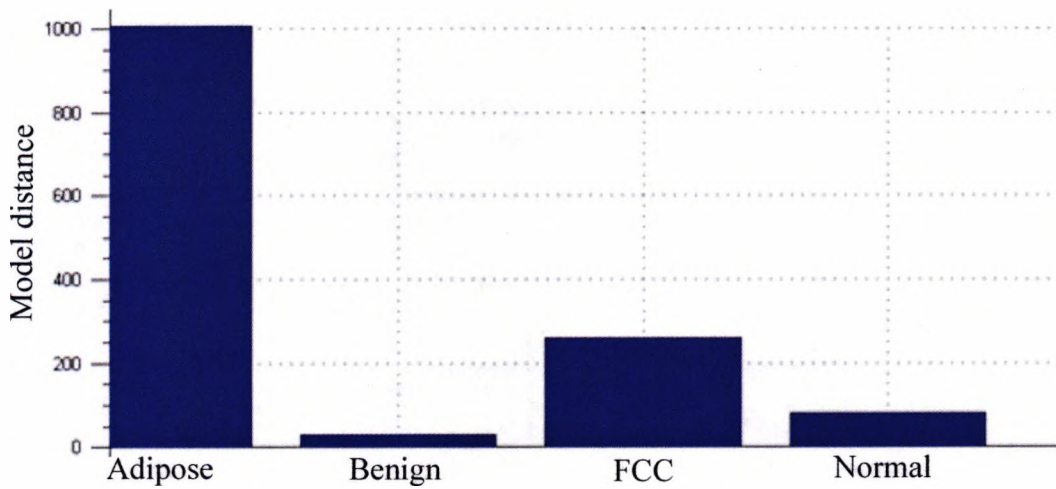


Figure 7.9b A model distance plot for the best model

The model distance shows how far apart the models for each tissue classification are. The further apart they are the greater ability they have to distinguish between samples. Figures 7.9a and b show the model distance from the malignant model for each tissue type. The best model (figure 7.9b) shows the adipose and FCC distance greatly increase with the improved model. The benign model is closest to the malignant tissue model in both cases.

Discrimination Power

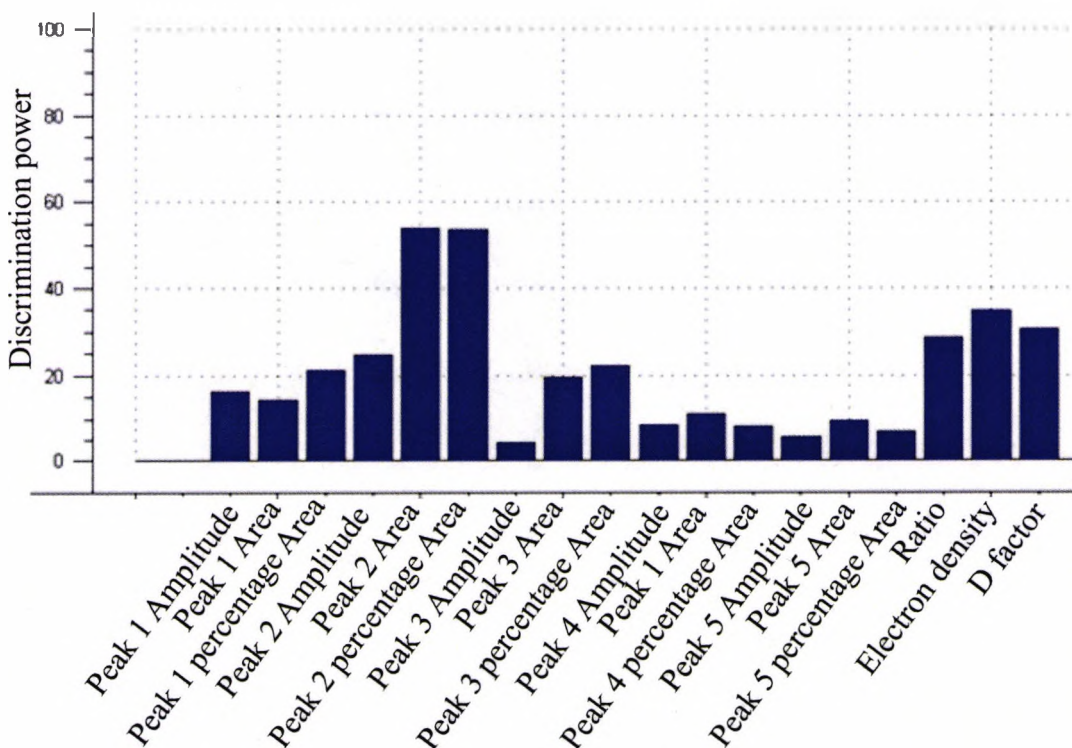


Figure 7.10a A discrimination power plot for the worst model

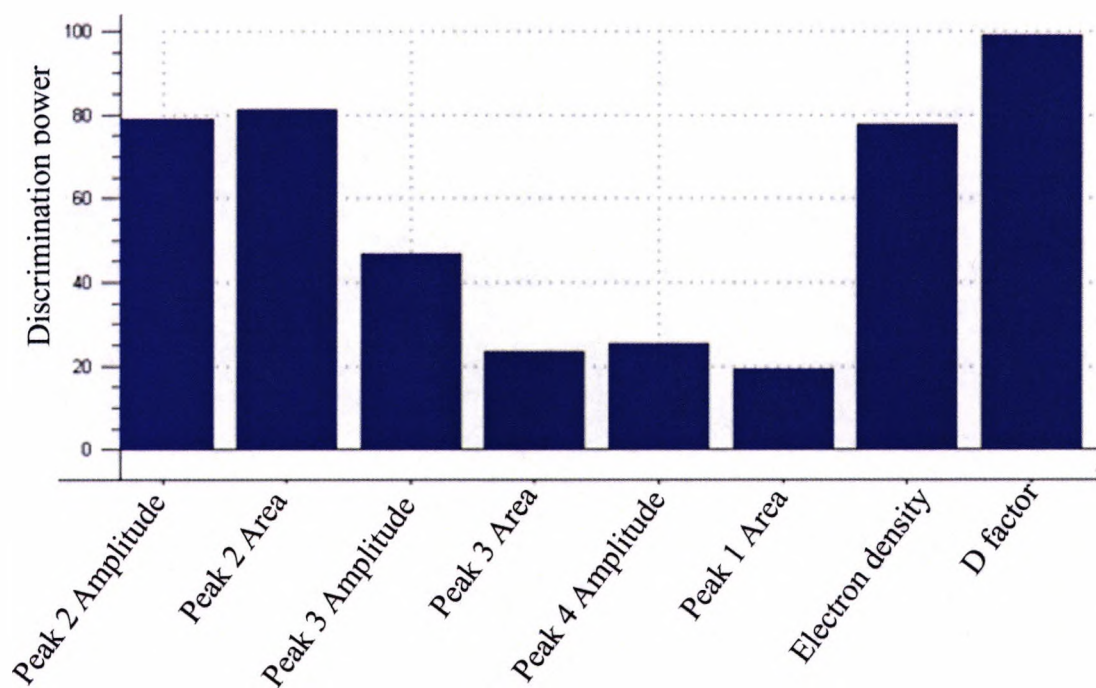


Figure 7.10b A discrimination power plot for the best model

The discrimination power shows how effective each variable is in distinguishing between two classifications. This plot is useful when improving a model as it can indicate when a variable is not providing any useful discrimination and should be excluded. Figure 7.10 a shows the discrimination power for each variable in the model where all variables were included. In this model the best discrimination power was 52. 7.10b shows the same variables when the least effective were excluded. The best discriminating power is now nearly 100.

Modelling power

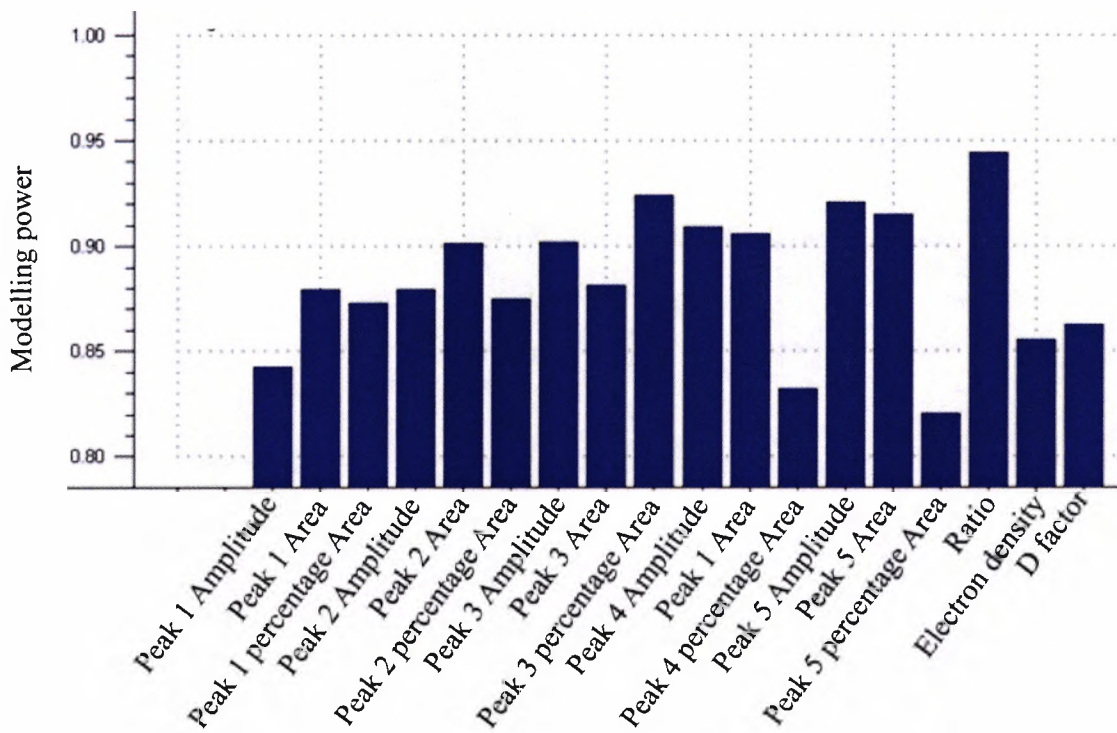


Figure 7.11a A modelling power plot for the worst model

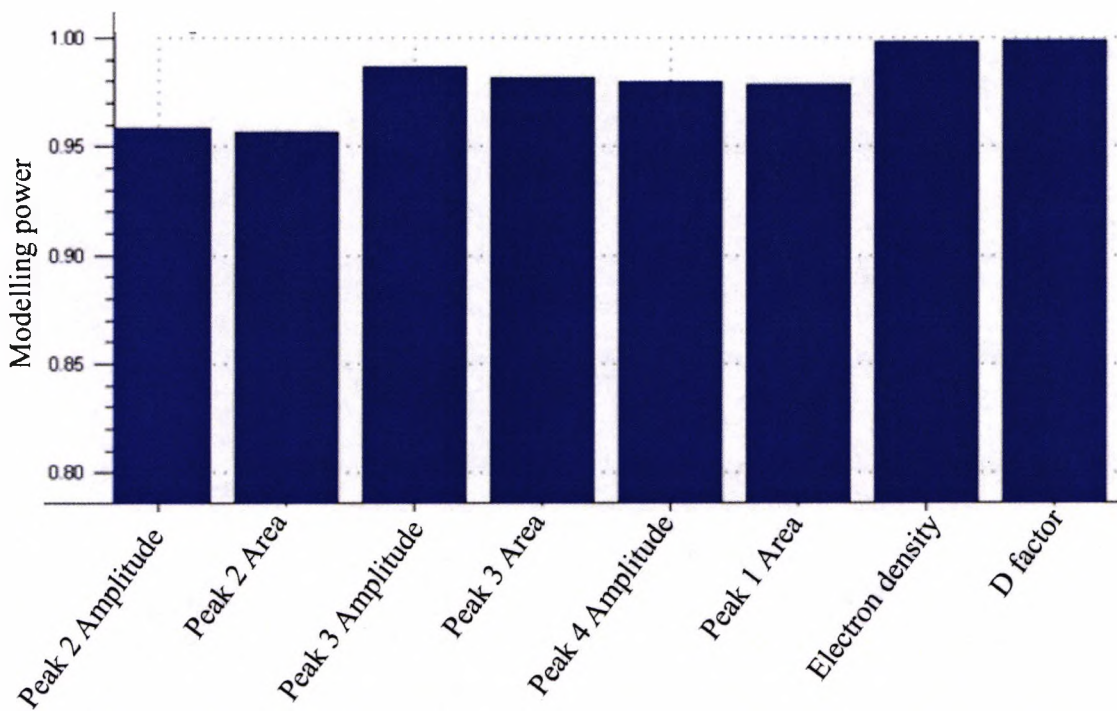


Figure 7.11b A modelling power plot for the best model

This is similar to a loadings plot in that it shows how each individual variable affects a single tissue model. A variable with a modelling power close to 0 has no effect and should be excluded. Again a marked improvement can be seen between the worst model (figure 7.11a) and the best model (figure 7.11b) when some variables had been excluded.

7.4.3.2 Analysis of models

The results from each model have been displayed in terms of how well they classified each test set sample. The first classification model was formulated using all the available variables. From analysis of the score and loading plots from each PCA of each sample group it was concluded that the percentage of counts in each peak was having a large influence on the data, but was grouping the data as this variable is specific to the experimental environment and not to the data class. Therefore this variable was producing an effect that is common to all the data and not to any particular class, and therefore effectively a source of noise. It was also evident that the adipose to fibrous peak ratio and the amount of fibrous tissue present were essentially the same and so only one needed to be included. Subsequent models were used to optimise the remaining data and decide which variables were most effective discriminators. The classification score was calculated based on the accuracy to which the classification model predicted the correct tissue type for the test samples as follows;

Zero points if the correct classification was not assigned

1 point if the correct classification only was assigned

0.5 points if the correct classification and one other was assigned

0.33 points if the correct classification and two others were assigned

0.25 points if the correct classification and three others were assigned

The table below shows which parameters were included in each of the 9 models and how each model compared in terms of its classification score.

| Model | No of variables | Classification score | Variables included |
|-------|-----------------|----------------------|---|
| 1 | 20 | 5.41 | Peaks 1-5 amplitude, area and percentage area; Electron density; Percentage fibrous; Adipose: fibrous peak ratio |
| 2 | 15 | 4.99 | Peaks 2-5 amplitude, area and percentage area; Electron density; Percentage fibrous; Adipose: fibrous peak ratio |
| 3 | 7 | 5.50 | Peak 2 Amplitude; Peak 2 area; Peak 3 amplitude; Peak 3 area; Electron density; Percentage fibrous; Adipose: fibrous peak ratio |
| 4 | 6 | 5.82 | Peak 2 Amplitude; Peak 2 area; Peak 3 amplitude; Peak 3 area; Electron density; Percentage fibrous; |
| 5 | 6 | 5.49 | Peak 2 Amplitude; Peak 2 area; Peak 3 amplitude; Peak 3 area; Electron density; Adipose: fibrous peak ratio |
| 6 | 8 | 4.50 | Peak 2 amplitude, area and percentage area; Peak 3 amplitude, area and percentage area; Electron density; Percentage fibrous; |
| 7 | 11 | 6.45 | Peak 2 amplitude, area and percentage area; Peak 3 amplitude, area and percentage area; Peak 4 amplitude, area and percentage area; Electron density; Percentage fibrous; |
| 8 | 8 | 8.33 | Peak 2 amplitude and area; Peak 3 amplitude and area; Peak 4 amplitude, area; Electron density; Percentage fibrous; |
| 9 | 10 | 6.91 | Peaks 2-5 amplitude and area; Electron density; Percentage fibrous; Adipose: fibrous peak ratio |

Table 7.1 Evaluation of each model

A classification score of 10 would indicate that all of the test samples had been correctly classified by the model. It can be seen from this table that increasing the number of variables included in the model does not necessarily improve the predictive ability of the classification model. The 8th model was the best at sample classification, discriminating 7 out of 10 samples correctly and unambiguously. The software provides a number of tools with which to assess the effectiveness of a classification model in discriminating test samples. The classification tables given in figure 7.12 are for each of the 9 tested models. The red squares show where a correct classification was awarded. The purple squares indicate an incorrect classification, which reduces the effect of the model. These tables were used to calculate the classification effectiveness score given in table 7.1

Chapter 7 Multivariate Data Analysis

| Model 1 | | | | | |
|----------|---------|--------|--------|--------|------|
| Sample | Adipose | Benign | Tumour | Normal | FCC |
| Adipose1 | Red | | | | |
| Adipose2 | Red | | | | |
| Benign1 | | Red | Blue | | |
| Benign2 | | Red | | | |
| Benign3 | Blue | Red | Blue | | Blue |
| Tumour1 | | Blue | Red | | Blue |
| Tumour2 | | Blue | Red | Blue | Blue |
| Tumour3 | | Blue | Red | | Blue |
| normal | | Blue | Blue | Red | Blue |
| FCC | | | | | Red |

| Model 2 | | | | | |
|----------|---------|--------|--------|--------|------|
| Sample | Adipose | Benign | Tumour | Normal | FCC |
| Adipose1 | Red | | | | |
| Adipose2 | Red | | | | |
| Benign1 | Blue | Red | Blue | | |
| Benign2 | Blue | Red | | | |
| Benign3 | Blue | Red | | | Blue |
| Tumour1 | | | Red | | Blue |
| Tumour2 | | Blue | Red | Blue | Blue |
| Tumour3 | | Blue | Red | | Blue |
| normal | | Blue | Blue | Red | Blue |
| FCC | Blue | | | | Red |

| Model 3 | | | | | |
|----------|---------|--------|--------|--------|------|
| Sample | Adipose | Benign | Tumour | Normal | FCC |
| Adipose1 | Red | | | | |
| Adipose2 | Red | | | | |
| Benign1 | Blue | Red | | | |
| Benign2 | Blue | Red | Blue | | Blue |
| Benign3 | | Red | | | |
| Tumour1 | | | Red | | Blue |
| Tumour2 | | Blue | Red | Blue | Blue |
| Tumour3 | | | Red | | Blue |
| normal | | Blue | Blue | Red | |
| FCC | Blue | | | | Red |

| Model 4 | | | | | |
|----------|---------|--------|--------|--------|------|
| Sample | Adipose | Benign | Tumour | Normal | FCC |
| Adipose1 | Red | | | | |
| Adipose2 | Red | | | | |
| Benign1 | | Red | | | |
| Benign2 | Blue | Red | Blue | | |
| Benign3 | Blue | Red | | Blue | |
| Tumour1 | | | Red | | Blue |
| Tumour2 | | | Red | Blue | Blue |
| Tumour3 | | | Red | | Blue |
| normal | | Blue | Blue | Red | |
| FCC | Blue | | | | Red |

| Model 5 | | | | | |
|----------|---------|--------|--------|--------|------|
| Sample | Adipose | Benign | Tumour | Normal | FCC |
| Adipose1 | Red | | | | |
| Adipose2 | Red | | | | |
| Benign1 | Blue | Red | Blue | | |
| Benign2 | Blue | Red | | | |
| Benign3 | | Red | | Blue | |
| Tumour1 | | | Red | | Blue |
| Tumour2 | | | Red | Blue | Blue |
| Tumour3 | | | Red | | Blue |
| normal | | Blue | Blue | Red | |
| FCC | Blue | | | | Red |

| Model 6 | | | | | |
|----------|---------|--------|--------|--------|------|
| Sample | Adipose | Benign | Tumour | Normal | FCC |
| Adipose1 | Red | | | | |
| Adipose2 | Red | | | | |
| Benign1 | Blue | Red | | | |
| Benign2 | Blue | Red | Blue | | Blue |
| Benign3 | Blue | Red | | Blue | Blue |
| Tumour1 | | | Red | | Blue |
| Tumour2 | | Blue | Red | Blue | Blue |
| Tumour3 | | | Red | | Blue |
| normal | | Blue | Blue | Red | |
| FCC | Blue | | | | Red |

| Model 7 | | | | | |
|----------|---------|--------|--------|--------|------|
| Sample | Adipose | Benign | Tumour | Normal | FCC |
| Adipose1 | Red | | | | |
| Adipose2 | Red | | | | |
| Benign1 | | Red | | | |
| Benign2 | | Red | | | |
| Benign3 | Blue | Red | | Blue | |
| Tumour1 | | Blue | Red | | Blue |
| Tumour2 | | Blue | Red | Blue | Blue |
| Tumour3 | | | Red | | Blue |
| normal | | Blue | Blue | Red | |
| FCC | Blue | | | | Red |

| Model 8 | | | | | |
|----------|---------|--------|--------|--------|------|
| Sample | Adipose | Benign | Tumour | Normal | FCC |
| Adipose1 | Red | | | | |
| Adipose2 | Red | | | | |
| Benign1 | | Red | | | |
| Benign2 | | Red | | | |
| Benign3 | | Red | | | |
| Tumour1 | | | Red | | Blue |
| Tumour2 | | | Red | Blue | Blue |
| Tumour3 | | | Red | | Blue |
| normal | | Blue | Blue | Red | |
| FCC | Blue | | | | Red |

| Model 9 | | | | | |
|----------|---------|--------|--------|--------|-----|
| Sample | Adipose | Benign | Tumour | Normal | FCC |
| Adipose1 | | | | | |
| Adipose2 | | | | | |
| Benign1 | | | | | |
| Benign2 | | | | | |
| Benign3 | | | | | |
| Tumour1 | | | | | |
| Tumour2 | | | | | |
| Tumour3 | | | | | |
| normal | | | | | |
| FCC | | | | | |

Figure 7.10 The results for each classification model when analysed using a test set of samples

7.5 Summary

A technique of multivariate analysis has been used to combine the scatter profile spectra and the electron density values into a tissue classification model. The number of parameters used in the model has been refined, by grading the success of each subsequent model.

The multivariate analysis has proven to be extremely effective when discriminating between samples. The classification of 7 out of 10 samples unambiguously by the best model (model 8) is remarkable, given the small sample sizes used to formulate the models. This study shows that this method has potential for building effective tissue classification models. The evaluation tools built in the software allow for an optimised model to be determined in a logical manner. This technique was efficient at detecting differences in the coherent scatter spectra that were not evident when the individual peaks were compared separately.

Chapter 8 Conclusions and further work

8.1 Introduction

There is a great deal of evidence to suggest that the metabolism and physiology of tumour cells differ greatly compared to that of normal and indeed benign cells. This study has been interested in establishing whether these differences produce a measurable variation in the tissue structure and/or composition, and hence the concentration of electrons.

8.2 Electron density measurements

The results overall were found to be similar for adipose, normal and benign tissues and much higher for malignant and FCC tissues. When measuring a change in the electron density it can be seen from equation 3.3 that this may be due to two factors, one is a difference in the composition and one is a difference in the tissue density. Within a benign tumour growth there is often an increase in cell proliferation but the cells themselves are relatively normal. However, in a malignant lesion the structure and metabolism of the tumour cells and host tissue have a different biochemical structure (Gould 1997). This implies that the increase in the electron density of benign tissues compared to adipose may potentially be due to an increase in cell concentration rather than to changes in composition, as seen in malignant tissues. This is consistent with the finding that benign tissues *ex-vivo* have an electron density which is only slightly higher than adipose tissues and malignant tissues display a much larger difference.

The other tissue type that was examined and found to have a high electron density was tissue after fibrocystic change. Although this term encompasses a range of histological changes, the majority are characterised by tissue fibrosis. This is a scarring process whereby the stromal (connective tissue) component of the tissue is increased and collagen accumulates. Although increased mature collagen may be seen in a few other benign disease processes in the breast, the most pronounced increase probably occurs during fibrocystic change. This may account for the finding that this tissue classification had a higher electron density than any other type of tissue, even

malignant tissue. When examining the tissues exhibiting fibrocystic change it is likely that any fluid filled pockets (cysts) will become dispersed during tissue collection and preparation leaving only the dense fibrotic tissue under examination.

As well as a difference in the mean of the samples it was also seen that the distribution of measurements varied. The spread of the 'normal' fibrous tissues and the FCC tissues was much greater than for the other types and appears to have a bimodal distribution. As previously discussed in section 4.2.5 it is difficult to know why this is with a small sample size and may be better explained by examining paired samples, consisting of a normal and a diseased/abnormal tissue from the same patient.

It is difficult to draw any conclusions from the 'normal' fibrous samples for a number of reasons. The first being that the sample size was small, consisting of only 9 samples. As the power calculations showed, a sample size of at least 42 is needed to have good statistical results but any sample size below about 12 is considered to small to analyse properly. The second problem with these samples is the origin of the normal tissues. Some were taken from healthy patients and some were from diseased breasts but at a distance from the tumour site. No detailed histopathology has been carried out on the samples and it is not known if coming from a diseased breast may have an effect on the tissue, even if it is not part of the tumour. This may have given rise to a large spread of results. This needs much more investigation.

The synchrotron measurements taken at the ESRF compared well to the laboratory results and although it was a small sample size it served to be a good test for reproducibility.

For the electron density measurements the null hypothesis, that all tissue types have the same median, has proven to be not true. The tissue types have been distinguished into two groups, one containing the adipose and benign and the other containing FCC and malignant tissues. The only tissue type that cannot be distinguished from any other is the normal tissue, due to its large standard deviation. The tissues cannot be distinctly differentiated from one another at this stage but the work is very promising.

8.3 Scatter profile measurements

The scatter profile measurements were difficult to correct, especially when using an EDXRD method. This was improved with a change in sample holder but the experimental inaccuracies may be larger than any differences in scatter spectra that are present. If fibrous tissues can be differentiated the differences will be small and so a very precise measurement system is needed. The sample size for this measurement is very difficult to determine as there was no real difference in the means of any of the parameters of the fibrous tissue types (normal, malignant and benign).

The comparison between each tissue parameter showed only significant differences between two sample groups, the fibrous tissues and tissues with a substantial fat content (adipose and FCC). Kidane *et al* (1999) performed a substantial analysis of the scatter profiles of adipose, benign, FCC and malignant tissues. They concluded that the measurement of scatter profiles is only sensitive to the relative content of adipose and fibrous components of the tissue. They go on to state that carcinoma tissues have less fat pockets than other tissues and so this technique could be used in tissue differentiation. The present work is in agreement with the conclusion that the measurements made were only sensitive enough to detect differences between adipose and fibrous tissue. However the present study has shown that fibroadenoma and normal fibrous tissues also have a very low fat content. This implies the usefulness of this technique is severely limited unless more precise measurements can be made that may detect more subtle differences.

8.4 Multivariate analysis

The multivariate analysis has been shown to be successful in tissue sample classification. Even with the limited sample numbers used the modelling proved efficient in tissue classification. The technique was able to utilise the scatter profile measurements and identify patterns within the data that were not detectable when looking at each parameter as an individual entity. This combination of measurement parameters is the key to successful tissue differentiation. The model can be improved with large sample numbers for each tissue type.

8.5 Further work

Since completion of this project the Radiation laboratory has been awarded a New and Emerging Technology grant and has attracted considerable private initiative money to continue this project, combined with work carried out by other members of the group. A new experimental set-up has been designed and built from scratch. This consists of a molybdenum target high power x-ray tube, focussing optics and three detectors. The system has been designed such that an ADXRD spectrum and the Compton scatter measurement can be made simultaneously. The system also has a detector placed to collect X-Ray Fluorescence data. A photograph of the new measurement system is given in figure 8.1.

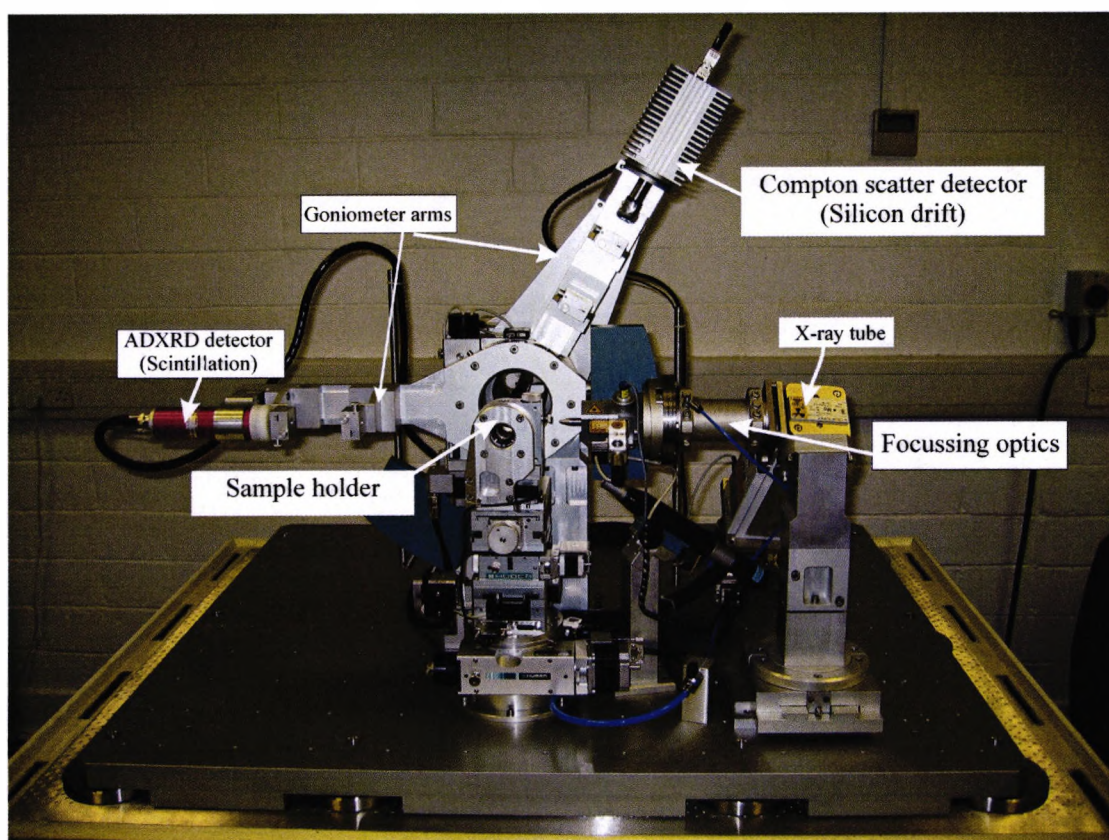


Figure 8.1 The new measurement system at City University

The data collected will be used to construct a multivariate analysis model which will be optimised once a substantial data set has been collected. Each part of the system and experimental design has been carefully considered and chosen to get the best

results from these measurements. The ways in which the present study has been improved are outlined below.

Tissue availability and supply

One of the main problems has been fresh tissue supply and availability. The project has now established collaborations with three NHS trust sites who will be supplying the project with tissues. The tissue bank will also be expanded to include other types of tissue, including liver, kidney and colon tissues. The tissues will also be supplied as matched pairs so that the effect of the normal biological variation between patients may be reduced.

Bulk tissue measurements

The second problem has been the bulk tissue classifications. Up until now the tissue has been supplied with a general classification. The assessment of the tissue has been done on parts of the tissue retained by the histopathologist, with adjacent parts being supplied to the laboratory. This technique has inherent problems in that a block of tissue can contain a large mixture of adipose and fibrous tissue as well as malignant and non-malignant areas. Although a diagnosis of a particular disease has been given the irradiated area may contain different types of tissue. The new system being put into place will take this into account by using a system where the tissue will be sent to a histopathologist once the scattering measurements have been performed.

Synchrotron availability

The energy dispersive measurements were the most inaccurate and were the hardest to correct. The problem so far with performing ADXRD measurements has been the need for access to a synchrotron. The new system will have the ability to perform angular dispersive measurements with a scintillation counter mounted on a goniometer arm, in an identical manner to the synchrotron measurements. The other advantages offered by the synchrotron are high count rates and a monochromatic source. The x-ray tube has been equipped with focussing optics. This is an arrangement of two parabolic x-ray mirrors that monochromate the beam by only reflecting the K-lines of the molybdenum tube output (17.4keV). They are focussed into a parallel beam so that no output from the tube is lost and the flux on the sample

may be increased by more than a factor of 1000, and is also highly monochromatic, compared to a normal tube output.

Sample holders

The sample holders that have been designed are cylindrical with thin walls made from plastic which is 100 μm thick. This will allow for simple data corrections without any loss of flux due to the attenuation of the sample holder. The plastic is strong enough to maintain rigidity and so will be an improvement on the holders with a mylar film window that tended to bulge at the windowed areas.

Sample degradation

The entire set-up is housed within a refrigerated unit, maintained at $+3^{\circ}\text{C}$. The tissues will be maintained at this temperature for the duration of the experiment. This is to prevent excessive tissue degradation occurring during the measurement process. Once the measurement has been successfully completed and checked the tissue section will be placed directly into a container of 10% formalin solution. The samples fixed in formalin will be returned to the histopathologist for reporting. The samples will only go through a single freeze cycle, as repeated refreezing of the sample degrades the cell structure and integrity.

Length of measurement

A motor will be in place to rotate the sample automatically throughout the entire measurement. This will be an improvement on the current system of rotating the system manually at regular intervals during the measurement. This will reduce the measurement times. As previously discussed the tube output will be massively increased which will also reduce measurement times.

Attenuation and density measurement

The attenuation coefficient was difficult to accurately measure. The new experiments will be performed with much smaller samples so that the whole sample will be irradiated. This does away with the need for an attenuation correction. The density of the samples will also be directly measured. This will greatly improve on the current technique which did not measure the tissue density.

Calibration

The calibration technique can be improved by measuring a far greater number of calibration solutions. These measurements will be repeated at regular intervals to test the reproducibility of the system.

8.6 Summary

The aim of this study was to determine whether broad classifications of breast tissue can be differentiated between using x-ray scattering properties. In order to assess whether this was possible the objectives outlined in section 1.1 were fulfilled as follows:

- Chapter 2 described how the experimental set-up was designed, built. Section 3.3.1 outlined how the system was optimised to measure Compton scattered radiation to within an acceptable experimental error. Section 5.3.3 showed how the laboratory set-up was optimised for the collection of coherent scatter profiles in the laboratory.
- Section 3.4 described the method used to calibrate the system for accurate electron density quantification.
- The preparation of the biological samples and the design of the sample holders were outlined in section 2.4.
- The results of the electron density measurements were presented and analysed in sections 4.2.1 and 4.2.2 and statistical methods were applied in section 4.2.3 to assess the validity of the study findings.

The overall objective of this planned work is the development of a device that will be used in the operating theatre to enable surgeons to identify diseased tissue at the margins of excision. It may also be possible to use the technique as an aid to histopathologists. The continuation and success of this work could result in an increase in the efficiency of cancer diagnosis and surgical procedures.

This pilot study has aided the design and optimisation of a new measurement system installed at City University and to develop novel data analysis techniques capable of differentiating between breast tissue types.

Appendix 1

Visual basic program

The following appendix outlines the visual basic program that was written for the data collection in the laboratory. Figure 4.10 shows the control terminal which was designed for this purpose.

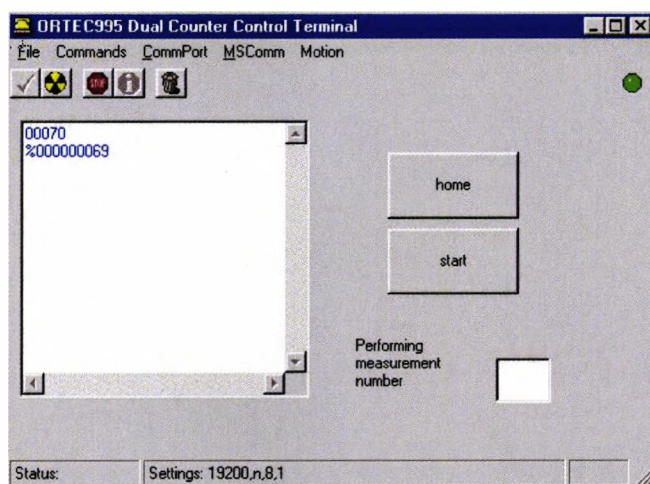


Figure A.1 The terminal for control of the electronics

The following list explains the options available to the user via the menu bar at the top of the screen:

- **File:** This offers the option of opening a LOG file, which then automatically stores any displayed data.
- **CommPort:** This enables the user to open or close the communications port, which is linked to the NIM electronics. When the port is open the button on the front panel is green and when the port is closed it is red. This menu option also allows a measurement time to be input. If no measurement time is specified the count has to be stopped manually, using the 'STOP' button.
- **MSComm:** This allows the port settings to be changed.
- **Motion:** The samples were mounted on a rotating platform and rotated during data collection to eliminate any effects due to the inhomogeneity of the sample. The visual basic program controls the rotation of the platform automatically. The number of rotations desired per sample (m) can be input

and the motor then rotates the sample by $(360/m)$ degrees between each measurement.

- **Commands:** The counter can be controlled via a number of buttons or menu options. The following flow diagram illustrates the process that is carried out once the start button has been pressed.

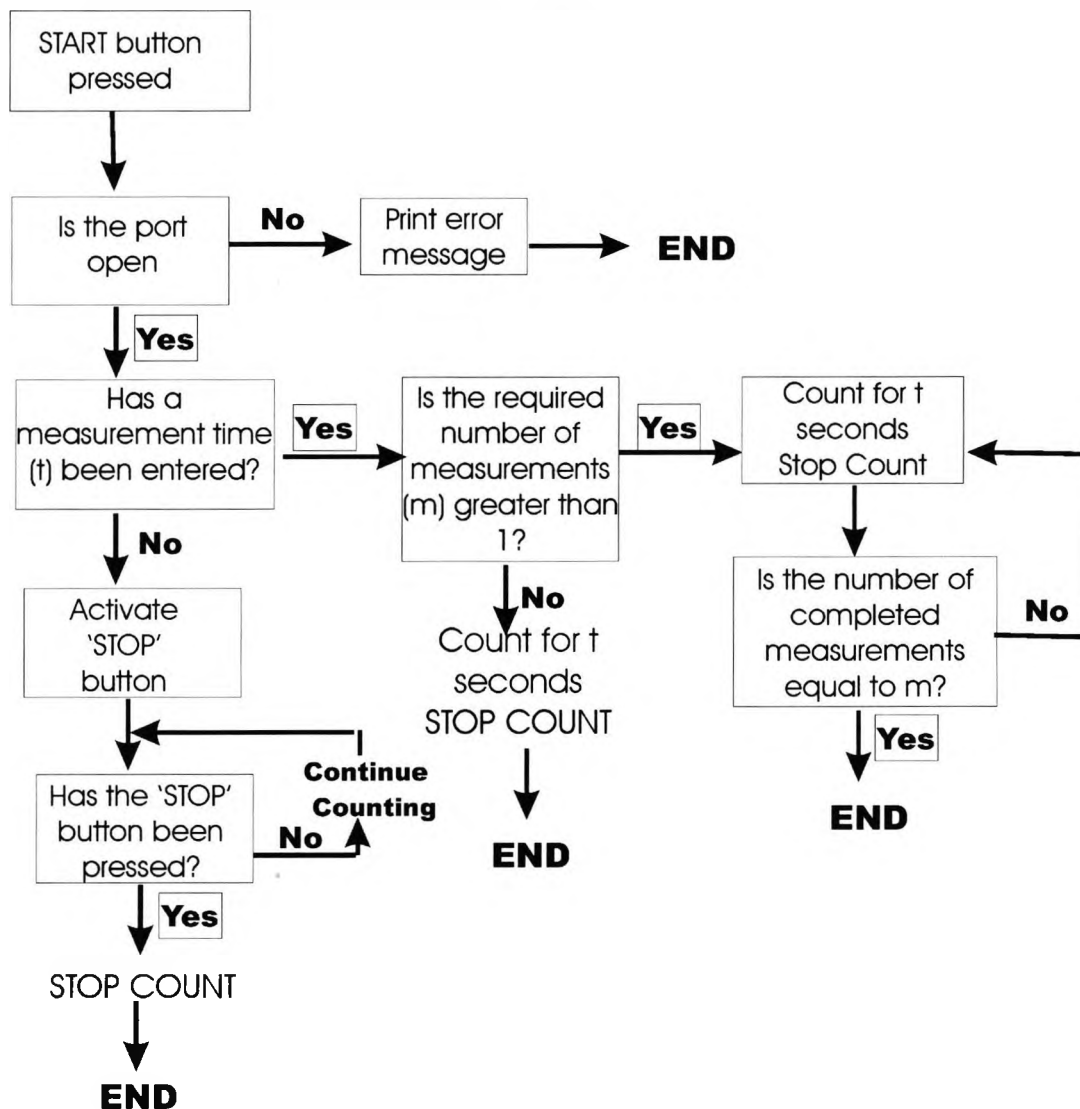


Figure A.2 A flow chart of the measurement program

Once the measurement is complete the user can press the 'Display Counts' button. This shows the collected counts in a window on the control panel and also writes the data to the LOG file, if one has been opened. The 'Clear All' button returns the counters to zero. The 'Home' button rotates the sample back to a pre-set zero position.

Appendix 2

Sample Composition Tables

Appendices

| Sample | Environment | Electron density | Physical density | Oxygen | Carbon | Hydrogen | Nitrogen | Sodium | Sulphur | Chlorine | Phosphorus |
|---------|-------------|------------------|------------------|--------|--------|----------|----------|--------|---------|----------|------------|
| A3(0)2 | Laboratory | 3.212E+23 | 0.961 | 0.243 | 0.627 | 0.113 | 0.013 | 0.001 | 0.001 | 0.001 | 0.001 |
| A3(0)1 | Laboratory | 3.222E+23 | 0.964 | 0.229 | 0.638 | 0.113 | 0.016 | 0.001 | 0.001 | 0.001 | 0.001 |
| A28(0)1 | Laboratory | 3.288E+23 | 0.986 | 0.345 | 0.516 | 0.111 | 0.023 | 0.001 | 0.001 | 0.001 | 0.001 |
| A35(0)1 | Laboratory | 3.174E+23 | 0.948 | 0.209 | 0.664 | 0.114 | 0.009 | 0.001 | 0.001 | 0.001 | 0.001 |
| A33(0)2 | Laboratory | 3.319E+23 | 0.997 | 0.435 | 0.429 | 0.110 | 0.021 | 0.001 | 0.001 | 0.001 | 0.001 |
| A33(0)1 | Laboratory | 3.272E+23 | 0.981 | 0.353 | 0.513 | 0.111 | 0.018 | 0.001 | 0.001 | 0.001 | 0.001 |
| A28(0)2 | Laboratory | 3.265E+23 | 0.979 | 0.346 | 0.521 | 0.112 | 0.018 | 0.001 | 0.001 | 0.001 | 0.001 |
| a02 | Laboratory | 3.371E+23 | 1.014 | 0.527 | 0.339 | 0.108 | 0.023 | 0.001 | 0.001 | 0.001 | 0.001 |
| a08 | Laboratory | 3.334E+23 | 1.002 | 0.441 | 0.419 | 0.110 | 0.026 | 0.001 | 0.001 | 0.001 | 0.001 |
| a10 | Laboratory | 3.241E+23 | 0.971 | 0.344 | 0.527 | 0.112 | 0.013 | 0.001 | 0.001 | 0.001 | 0.001 |
| a14 | Laboratory | 3.361E+23 | 1.011 | 0.506 | 0.358 | 0.108 | 0.023 | 0.001 | 0.001 | 0.001 | 0.001 |
| a15 | Laboratory | 3.171E+23 | 0.947 | 0.074 | 0.793 | 0.115 | 0.013 | 0.001 | 0.001 | 0.001 | 0.001 |
| a17 | Laboratory | 3.323E+23 | 0.998 | 0.461 | 0.407 | 0.109 | 0.019 | 0.001 | 0.001 | 0.001 | 0.001 |
| t11 | Laboratory | 3.472E+23 | 1.048 | 0.650 | 0.203 | 0.105 | 0.037 | 0.001 | 0.002 | 0.001 | 0.001 |
| t14 | Laboratory | 3.494E+23 | 1.056 | 0.680 | 0.173 | 0.105 | 0.038 | 0.001 | 0.002 | 0.001 | 0.001 |
| t20 | Laboratory | 3.251E+23 | 0.974 | 0.268 | 0.594 | 0.112 | 0.020 | 0.001 | 0.002 | 0.001 | 0.001 |
| t53 | Laboratory | 3.639E+23 | 1.105 | 0.815 | 0.036 | 0.100 | 0.044 | 0.001 | 0.002 | 0.001 | 0.001 |
| t59 | Laboratory | 3.537E+23 | 1.071 | 0.730 | 0.122 | 0.103 | 0.040 | 0.001 | 0.002 | 0.001 | 0.001 |
| tum02 | Laboratory | 3.292E+23 | 0.988 | 0.350 | 0.510 | 0.111 | 0.024 | 0.001 | 0.002 | 0.001 | 0.001 |
| tum03 | Laboratory | 3.581E+23 | 1.085 | 0.771 | 0.080 | 0.102 | 0.042 | 0.001 | 0.002 | 0.001 | 0.001 |
| tum04 | Laboratory | 3.510E+23 | 1.061 | 0.698 | 0.154 | 0.104 | 0.039 | 0.001 | 0.002 | 0.001 | 0.001 |
| tum05 | Laboratory | 3.324E+23 | 0.998 | 0.413 | 0.445 | 0.110 | 0.026 | 0.001 | 0.002 | 0.001 | 0.001 |
| T7(1)2 | Laboratory | 3.427E+23 | 1.033 | 0.587 | 0.267 | 0.107 | 0.034 | 0.001 | 0.002 | 0.001 | 0.001 |
| T18(1)2 | Laboratory | 3.582E+23 | 1.086 | 0.774 | 0.078 | 0.102 | 0.042 | 0.001 | 0.002 | 0.001 | 0.001 |
| T9(0)2 | Laboratory | 3.586E+23 | 1.087 | 0.785 | 0.067 | 0.101 | 0.041 | 0.001 | 0.002 | 0.001 | 0.001 |
| T20(0)2 | Laboratory | 3.561E+23 | 1.079 | 0.755 | 0.097 | 0.102 | 0.041 | 0.001 | 0.002 | 0.001 | 0.001 |
| T59(0)1 | Laboratory | 3.520E+23 | 1.065 | 0.710 | 0.142 | 0.104 | 0.039 | 0.001 | 0.002 | 0.001 | 0.001 |
| T59(1)1 | Laboratory | 3.533E+23 | 1.069 | 0.726 | 0.126 | 0.103 | 0.039 | 0.001 | 0.002 | 0.001 | 0.001 |
| T7(0)1 | Laboratory | 3.605E+23 | 1.094 | 0.794 | 0.058 | 0.101 | 0.043 | 0.001 | 0.002 | 0.001 | 0.001 |
| T18(0)1 | Laboratory | 3.597E+23 | 1.091 | 0.788 | 0.064 | 0.101 | 0.042 | 0.001 | 0.002 | 0.001 | 0.001 |
| T20(0)1 | Laboratory | 3.475E+23 | 1.049 | 0.656 | 0.197 | 0.105 | 0.036 | 0.001 | 0.002 | 0.001 | 0.001 |
| ben01 | Laboratory | 3.335E+23 | 1.002 | 0.432 | 0.425 | 0.110 | 0.028 | 0.001 | 0.002 | 0.001 | 0.001 |
| ben02 | Laboratory | 3.485E+23 | 1.053 | 0.669 | 0.184 | 0.105 | 0.037 | 0.001 | 0.002 | 0.001 | 0.001 |
| ben03 | Laboratory | 3.394E+23 | 1.022 | 0.536 | 0.319 | 0.108 | 0.032 | 0.001 | 0.002 | 0.001 | 0.001 |
| ben04 | Laboratory | 3.464E+23 | 1.046 | 0.642 | 0.212 | 0.105 | 0.036 | 0.001 | 0.002 | 0.001 | 0.001 |
| ben05 | Laboratory | 3.214E+23 | 0.962 | 0.176 | 0.689 | 0.113 | 0.017 | 0.001 | 0.002 | 0.001 | 0.001 |
| ben06 | Laboratory | 3.366E+23 | 1.012 | 0.488 | 0.368 | 0.109 | 0.030 | 0.001 | 0.002 | 0.001 | 0.001 |
| ben07 | Laboratory | 3.012E+23 | 0.895 | -0.383 | 1.274 | 0.120 | -0.006 | 0.001 | 0.002 | 0.001 | 0.001 |
| ben08 | Laboratory | 3.284E+23 | 0.985 | 0.330 | 0.530 | 0.111 | 0.024 | 0.001 | 0.002 | 0.001 | 0.001 |
| ben09 | Laboratory | 3.278E+23 | 0.983 | 0.318 | 0.542 | 0.112 | 0.023 | 0.001 | 0.002 | 0.001 | 0.001 |

Appendices

| Sample | Environment | Electron density | Physical density | Oxygen | Carbon | Hydrogen | Nitrogen | Sodium | Sulphur | Chlorine | Phosphorus |
|----------|-------------|------------------|------------------|--------|--------|----------|----------|--------|---------|----------|------------|
| ben10 | Laboratory | 3.270E+23 | 0.980 | 0.300 | 0.561 | 0.112 | 0.023 | 0.001 | 0.002 | 0.001 | 0.001 |
| B114(0)1 | Laboratory | 3.280E+23 | 0.984 | 0.322 | 0.539 | 0.112 | 0.023 | 0.001 | 0.002 | 0.001 | 0.001 |
| B114(2)1 | Laboratory | 3.350E+23 | 1.007 | 0.460 | 0.396 | 0.109 | 0.029 | 0.001 | 0.002 | 0.001 | 0.001 |
| B110(0)1 | Laboratory | 3.283E+23 | 0.984 | 0.326 | 0.534 | 0.112 | 0.024 | 0.001 | 0.002 | 0.001 | 0.001 |
| B110(1)1 | Laboratory | 3.359E+23 | 1.010 | 0.477 | 0.380 | 0.109 | 0.030 | 0.001 | 0.002 | 0.001 | 0.001 |
| B115(1)1 | Laboratory | 3.308E+23 | 0.993 | 0.378 | 0.480 | 0.111 | 0.026 | 0.001 | 0.002 | 0.001 | 0.001 |
| B115(2)1 | Laboratory | 3.275E+23 | 0.982 | 0.309 | 0.551 | 0.112 | 0.023 | 0.001 | 0.002 | 0.001 | 0.001 |
| B112(0)1 | Laboratory | 3.361E+23 | 1.011 | 0.480 | 0.376 | 0.109 | 0.030 | 0.001 | 0.002 | 0.001 | 0.001 |
| B112(2)1 | Laboratory | 3.249E+23 | 0.973 | 0.255 | 0.607 | 0.113 | 0.020 | 0.001 | 0.002 | 0.001 | 0.001 |
| B113(0)1 | Laboratory | 3.325E+23 | 0.999 | 0.415 | 0.444 | 0.110 | 0.027 | 0.001 | 0.002 | 0.001 | 0.001 |
| B113(1)1 | Laboratory | 3.284E+23 | 0.985 | 0.338 | 0.523 | 0.111 | 0.023 | 0.001 | 0.002 | 0.001 | 0.001 |
| FCC01 | Laboratory | 3.253E+23 | 0.975 | 0.287 | 0.577 | 0.112 | 0.019 | 0.001 | 0.002 | 0.001 | 0.001 |
| FCC02 | Laboratory | 3.639E+23 | 1.105 | 0.831 | 0.021 | 0.100 | 0.044 | 0.001 | 0.002 | 0.001 | 0.001 |
| FCC03 | Laboratory | 2.792E+23 | 0.823 | -1.058 | 1.984 | 0.127 | -0.038 | 0.001 | 0.002 | 0.001 | 0.001 |
| FCC04 | Laboratory | 3.604E+23 | 1.093 | 0.797 | 0.056 | 0.101 | 0.042 | 0.001 | 0.002 | 0.001 | 0.001 |
| FCC05 | Laboratory | 3.670E+23 | 1.116 | 0.845 | 0.007 | 0.099 | 0.045 | 0.001 | 0.002 | 0.001 | 0.001 |
| FCC06 | Laboratory | 3.259E+23 | 0.977 | 0.345 | 0.522 | 0.112 | 0.016 | 0.001 | 0.002 | 0.001 | 0.001 |
| FCC07 | Laboratory | 3.559E+23 | 1.078 | 0.751 | 0.100 | 0.102 | 0.041 | 0.001 | 0.002 | 0.001 | 0.001 |
| FCC08 | Laboratory | 3.097E+23 | 0.923 | 0.031 | 0.845 | 0.117 | 0.002 | 0.001 | 0.002 | 0.001 | 0.001 |
| FCC09 | Laboratory | 3.159E+23 | 0.943 | 0.206 | 0.667 | 0.115 | 0.007 | 0.001 | 0.002 | 0.001 | 0.001 |
| FCC10 | Laboratory | 3.680E+23 | 1.119 | 0.852 | 0.000 | 0.098 | 0.045 | 0.001 | 0.002 | 0.001 | 0.001 |
| Norm03 | Laboratory | 3.225E+23 | 0.965 | 0.201 | 0.662 | 0.113 | 0.018 | 0.001 | 0.002 | 0.001 | 0.001 |
| Norm04 | Laboratory | 3.540E+23 | 1.072 | 0.732 | 0.120 | 0.103 | 0.040 | 0.001 | 0.002 | 0.001 | 0.001 |
| Norm05 | Laboratory | 3.339E+23 | 1.003 | 0.440 | 0.417 | 0.110 | 0.028 | 0.001 | 0.002 | 0.001 | 0.001 |
| Norm06 | Laboratory | 3.485E+23 | 1.053 | 0.669 | 0.185 | 0.105 | 0.037 | 0.001 | 0.002 | 0.001 | 0.001 |
| Norm07 | Laboratory | 3.521E+23 | 1.065 | 0.711 | 0.141 | 0.104 | 0.040 | 0.001 | 0.002 | 0.001 | 0.001 |
| Norm08 | Laboratory | 3.181E+23 | 0.951 | 0.103 | 0.765 | 0.115 | 0.014 | 0.001 | 0.002 | 0.001 | 0.001 |
| Norm09 | Laboratory | 3.240E+23 | 0.970 | 0.240 | 0.622 | 0.113 | 0.019 | 0.001 | 0.002 | 0.001 | 0.001 |
| Norm10 | Laboratory | 3.321E+23 | 0.997 | 0.404 | 0.454 | 0.110 | 0.027 | 0.001 | 0.002 | 0.001 | 0.001 |
| A28(0)1 | Laboratory | 3.288E+23 | 0.986 | 0.342 | 0.518 | 0.111 | 0.024 | 0.001 | 0.002 | 0.001 | 0.001 |
| A35(0)1 | Laboratory | 3.174E+23 | 0.948 | 0.136 | 0.733 | 0.115 | 0.011 | 0.001 | 0.002 | 0.001 | 0.001 |
| A33(0)2 | Laboratory | 3.319E+23 | 0.997 | 0.459 | 0.409 | 0.109 | 0.018 | 0.001 | 0.002 | 0.001 | 0.001 |
| T7(1)2 | Laboratory | 3.427E+23 | 1.033 | 0.587 | 0.267 | 0.107 | 0.034 | 0.001 | 0.002 | 0.001 | 0.001 |
| T18(1)2 | Laboratory | 3.582E+23 | 1.086 | 0.773 | 0.079 | 0.102 | 0.042 | 0.001 | 0.002 | 0.001 | 0.001 |
| T20(0)2 | Laboratory | 3.561E+23 | 1.079 | 0.754 | 0.098 | 0.102 | 0.041 | 0.001 | 0.002 | 0.001 | 0.001 |
| T59(0)1 | Laboratory | 3.520E+23 | 1.065 | 0.710 | 0.142 | 0.104 | 0.039 | 0.001 | 0.002 | 0.001 | 0.001 |
| B114(0)1 | Laboratory | 3.280E+23 | 0.984 | 0.323 | 0.538 | 0.112 | 0.023 | 0.001 | 0.002 | 0.001 | 0.001 |
| B110(0)1 | Laboratory | 3.283E+23 | 0.984 | 0.327 | 0.533 | 0.112 | 0.024 | 0.001 | 0.002 | 0.001 | 0.001 |
| B115(1)1 | Laboratory | 3.308E+23 | 0.993 | 0.380 | 0.478 | 0.111 | 0.026 | 0.001 | 0.002 | 0.001 | 0.001 |
| B113(0)1 | Laboratory | 3.325E+23 | 0.999 | 0.414 | 0.444 | 0.110 | 0.027 | 0.001 | 0.002 | 0.001 | 0.001 |

| Sample | Environment | Electron density | Physical density | Oxygen | Carbon | Hydrogen | Nitrogen | Sodium | Sulphur | Chlorine | Phosphorus |
|----------|---------------|------------------|------------------|--------|--------|----------|----------|--------|---------|----------|------------|
| A28(0)1 | Daresbury SRS | 3.288E+23 | 0.99 | 0.342 | 0.518 | 0.111 | 0.024 | 0.001 | 0.002 | 0.001 | 0.001 |
| A35(0)1 | Daresbury SRS | 3.174E+23 | 0.95 | 0.136 | 0.733 | 0.115 | 0.011 | 0.001 | 0.002 | 0.001 | 0.001 |
| A33(0)2 | Daresbury SRS | 3.319E+23 | 1.00 | 0.449 | 0.417 | 0.110 | 0.020 | 0.001 | 0.002 | 0.001 | 0.001 |
| T7(1)2 | Daresbury SRS | 3.427E+23 | 1.03 | 0.587 | 0.267 | 0.107 | 0.034 | 0.001 | 0.002 | 0.001 | 0.001 |
| T18(1)2 | Daresbury SRS | 3.582E+23 | 1.09 | 0.773 | 0.079 | 0.102 | 0.042 | 0.001 | 0.002 | 0.001 | 0.001 |
| T20(0)2 | Daresbury SRS | 3.561E+23 | 1.08 | 0.754 | 0.098 | 0.102 | 0.041 | 0.001 | 0.002 | 0.001 | 0.001 |
| T59(0)1 | Daresbury SRS | 3.520E+23 | 1.06 | 0.710 | 0.142 | 0.104 | 0.039 | 0.001 | 0.002 | 0.001 | 0.001 |
| B114(0)1 | Daresbury SRS | 3.280E+23 | 0.98 | 0.323 | 0.538 | 0.112 | 0.023 | 0.001 | 0.002 | 0.001 | 0.001 |
| B110(0)1 | Daresbury SRS | 3.283E+23 | 0.98 | 0.327 | 0.533 | 0.112 | 0.024 | 0.001 | 0.002 | 0.001 | 0.001 |
| B115(1)1 | Daresbury SRS | 3.308E+23 | 0.99 | 0.380 | 0.478 | 0.111 | 0.026 | 0.001 | 0.002 | 0.001 | 0.001 |
| B113(0)1 | Daresbury SRS | 3.325E+23 | 1.00 | 0.414 | 0.444 | 0.110 | 0.027 | 0.001 | 0.002 | 0.001 | 0.001 |
| a2 | ESRF | 3.110E+23 | 0.93 | 0.188 | 0.691 | 0.116 | 0.001 | 0.001 | 0.001 | 0.001 | 0.001 |
| a06(1) | ESRF | 3.298E+23 | 0.99 | 0.369 | 0.492 | 0.111 | 0.024 | 0.001 | 0.001 | 0.001 | 0.001 |
| a06(2) | ESRF | 3.307E+23 | 0.99 | 0.440 | 0.429 | 0.110 | 0.018 | 0.001 | 0.001 | 0.001 | 0.001 |
| a06(3) | ESRF | 3.480E+23 | 1.05 | 0.662 | 0.192 | 0.105 | 0.037 | 0.001 | 0.001 | 0.001 | 0.001 |
| a08 | ESRF | 3.222E+23 | 0.96 | 0.214 | 0.652 | 0.113 | 0.017 | 0.001 | 0.001 | 0.001 | 0.001 |
| a10 | ESRF | 3.137E+23 | 0.94 | 0.221 | 0.656 | 0.115 | 0.003 | 0.001 | 0.001 | 0.001 | 0.001 |
| a14 | ESRF | 3.286E+23 | 0.99 | 0.402 | 0.466 | 0.111 | 0.017 | 0.001 | 0.001 | 0.001 | 0.001 |
| a15 | ESRF | 3.148E+23 | 0.94 | 0.012 | 0.858 | 0.116 | 0.010 | 0.001 | 0.001 | 0.001 | 0.001 |
| a17 | ESRF | 3.115E+23 | 0.93 | 0.194 | 0.684 | 0.116 | 0.002 | 0.001 | 0.001 | 0.001 | 0.001 |
| t11 | ESRF | 3.504E+23 | 1.06 | 0.692 | 0.161 | 0.104 | 0.039 | 0.001 | 0.001 | 0.001 | 0.001 |
| t14 | ESRF | 3.524E+23 | 1.07 | 0.714 | 0.139 | 0.104 | 0.040 | 0.001 | 0.001 | 0.001 | 0.001 |
| t20 | ESRF | 3.506E+23 | 1.06 | 0.694 | 0.159 | 0.104 | 0.038 | 0.001 | 0.001 | 0.001 | 0.001 |
| t53 | ESRF | 3.620E+23 | 1.10 | 0.802 | 0.050 | 0.100 | 0.043 | 0.001 | 0.001 | 0.001 | 0.001 |
| t59 | ESRF | 3.677E+23 | 1.12 | 0.835 | 0.018 | 0.098 | 0.044 | 0.001 | 0.001 | 0.001 | 0.001 |
| tum01 | ESRF | 3.595E+23 | 1.09 | 0.808 | 0.046 | 0.101 | 0.041 | 0.001 | 0.002 | 0.001 | 0.001 |
| tum02 | ESRF | 3.517E+23 | 1.06 | 0.708 | 0.144 | 0.104 | 0.039 | 0.001 | 0.002 | 0.001 | 0.001 |
| tum03 | ESRF | 3.659E+23 | 1.11 | 0.827 | 0.025 | 0.099 | 0.044 | 0.001 | 0.002 | 0.001 | 0.001 |
| tum04 | ESRF | 3.583E+23 | 1.09 | 0.773 | 0.078 | 0.102 | 0.042 | 0.001 | 0.002 | 0.001 | 0.001 |
| tum05 | ESRF | 3.476E+23 | 1.05 | 0.657 | 0.196 | 0.105 | 0.037 | 0.001 | 0.002 | 0.001 | 0.001 |
| ben01 | ESRF | 3.202E+23 | 0.96 | 0.283 | 0.590 | 0.113 | 0.010 | 0.001 | 0.002 | 0.001 | 0.001 |
| ben02 | ESRF | 3.322E+23 | 1.00 | 0.405 | 0.453 | 0.110 | 0.027 | 0.001 | 0.002 | 0.001 | 0.001 |
| ben03 | ESRF | 3.359E+23 | 1.01 | 0.475 | 0.382 | 0.109 | 0.030 | 0.001 | 0.002 | 0.001 | 0.001 |
| ben04 | ESRF | 3.206E+23 | 0.96 | 0.154 | 0.714 | 0.114 | 0.016 | 0.001 | 0.002 | 0.001 | 0.001 |
| ben05 | ESRF | 3.309E+23 | 0.99 | 0.379 | 0.480 | 0.111 | 0.026 | 0.001 | 0.002 | 0.001 | 0.001 |
| ben07 | ESRF | 3.169E+23 | 0.95 | 0.061 | 0.810 | 0.115 | 0.013 | 0.001 | 0.002 | 0.001 | 0.001 |
| ben08 | ESRF | 3.335E+23 | 1.00 | 0.432 | 0.425 | 0.110 | 0.028 | 0.001 | 0.002 | 0.001 | 0.001 |
| ben09 | ESRF | 3.265E+23 | 0.98 | 0.289 | 0.573 | 0.112 | 0.022 | 0.001 | 0.002 | 0.001 | 0.001 |
| ben10 | ESRF | 3.437E+23 | 1.04 | 0.601 | 0.252 | 0.106 | 0.035 | 0.001 | 0.002 | 0.001 | 0.001 |
| FCC01 | ESRF | 3.635E+23 | 1.10 | 0.817 | 0.035 | 0.100 | 0.044 | 0.001 | 0.002 | 0.001 | 0.001 |

| Sample | Environment | Electron density | Physical density | Oxygen | Carbon | Hydrogen | Nitrogen | Sodium | Sulphur | Chlorine | Phosphorus |
|--------|-------------|------------------|------------------|--------|--------|----------|----------|--------|---------|----------|------------|
| FCC02 | ESRF | 3.600E+23 | 1.09 | 0.789 | 0.063 | 0.101 | 0.042 | 0.001 | 0.002 | 0.001 | 0.001 |
| FCC03 | ESRF | 3.499E+23 | 1.06 | 0.685 | 0.167 | 0.104 | 0.038 | 0.001 | 0.002 | 0.001 | 0.001 |
| FCC04 | ESRF | 3.642E+23 | 1.11 | 0.819 | 0.033 | 0.100 | 0.044 | 0.001 | 0.002 | 0.001 | 0.001 |
| FCC05 | ESRF | 3.639E+23 | 1.11 | 0.823 | 0.028 | 0.100 | 0.044 | 0.001 | 0.002 | 0.001 | 0.001 |
| FCC06 | ESRF | 2.890E+23 | 0.85 | -0.398 | 1.299 | 0.124 | -0.020 | 0.001 | 0.002 | 0.001 | 0.001 |
| FCC07 | ESRF | 3.643E+23 | 1.11 | 0.819 | 0.034 | 0.100 | 0.044 | 0.001 | 0.002 | 0.001 | 0.001 |
| FCC08 | ESRF | 3.368E+23 | 1.01 | 0.510 | 0.353 | 0.108 | 0.026 | 0.001 | 0.002 | 0.001 | 0.001 |
| FCC09 | ESRF | 3.050E+23 | 0.91 | 0.042 | 0.839 | 0.117 | -0.003 | 0.001 | 0.002 | 0.001 | 0.001 |
| FCC10 | ESRF | 3.575E+23 | 1.08 | 0.767 | 0.084 | 0.102 | 0.042 | 0.001 | 0.002 | 0.001 | 0.001 |
| Norm01 | ESRF | 3.242E+23 | 0.97 | 0.286 | 0.580 | 0.112 | 0.017 | 0.001 | 0.002 | 0.001 | 0.001 |
| Norm02 | ESRF | 3.262E+23 | 0.98 | 0.322 | 0.542 | 0.112 | 0.019 | 0.001 | 0.002 | 0.001 | 0.001 |
| Norm04 | ESRF | 3.303E+23 | 0.99 | 0.370 | 0.489 | 0.111 | 0.025 | 0.001 | 0.002 | 0.001 | 0.001 |
| Norm05 | ESRF | 3.357E+23 | 1.01 | 0.473 | 0.384 | 0.109 | 0.029 | 0.001 | 0.002 | 0.001 | 0.001 |
| Norm06 | ESRF | 3.380E+23 | 1.02 | 0.515 | 0.342 | 0.108 | 0.030 | 0.001 | 0.002 | 0.001 | 0.001 |
| Norm07 | ESRF | 3.584E+23 | 1.09 | 0.774 | 0.078 | 0.102 | 0.042 | 0.001 | 0.002 | 0.001 | 0.001 |
| Norm08 | ESRF | 3.135E+23 | 0.94 | 0.000 | 0.870 | 0.116 | 0.009 | 0.001 | 0.002 | 0.001 | 0.001 |
| Norm09 | ESRF | 3.126E+23 | 0.93 | 0.000 | 0.870 | 0.117 | 0.008 | 0.001 | 0.002 | 0.001 | 0.001 |
| Norm10 | ESRF | 3.251E+23 | 0.97 | 0.256 | 0.605 | 0.113 | 0.021 | 0.001 | 0.002 | 0.001 | 0.001 |

Appendix 3

Publications

The work undertaken for this thesis has been included in the following publications:

1. Ryan E and Farquharson M J 2004 Angular dispersive X-ray scattering from breast tissue using synchrotron radiation *Radiation Physics and Chemistry* **71** 971-972
2. Ryan, E., Farquharson, M. J., and Geraki, K. 2004 Measurement and analysis of coherent scatter profiles for adipose, benign and malignant breast tissue differentiation. Proceedings from the European Conference on X-Ray Spectrometry, Sardinia Conference Proceedings
3. Ryan E A, Farquharson M J, and Flinton D M 2005 The use of Compton scattering to differentiate between classifications of normal and diseased breast tissue *Physics in Medicine and Biology* **50** 3337-3348

References

- Al-Bahri J S and Spyrou N M 1998 Electron density of normal and pathological breast tissues using a Compton scattering technique *Applied Radiation and Isotopes* **49** 1677-1684
- Allday A 2004 Detection capabilities of energy dispersive x-ray diffraction with respect to in-vitro trabecular bone mineral loss *PhD Thesis* City University, London
- Arcturus Bioscience 2006 [online] Available at: <http://www.arctur.com> [Accessed April 2006]
- AstraZenica Oncology 2006 [online] Available at: <http://www.breastcancersource.com> [Accessed April 2006]
- Attix F 1986 *Introduction to radiological physics and radiation dosimetry* (New York: Wiley and Sons)
- Avtandilov G, Dembo A, Komardin O, Lazarev P, Paukshto M, Shkolnik L, and Zayratiyants O 2000 Human tissue analysis by small-angle X-ray scattering *Journal of Applied Crystallography* **33** 511-514
- Baum M, Saunders C, and Meredith S 1994 *Breast Cancer* (Oxford: Oxford University Press)
- Berger, M. and Hubbell, J. 1998 XCOM. Photon Cross sections on a personal computer Version 2.1 Gaithersburg: National Institute of Standards and Technology.
- Bravin A 2003 Exploiting the x-ray refraction contrast with an analyser: the state of the art *Journal of Physics D-Applied Physics* **36** A24-A29
- Brock C S, Meikle S R, and Price P 1997 Does fluorine-18 fluorodeoxyglucose metabolic imaging of tumours benefit oncology? *European Journal of Nuclear Medicine* **24** 691-705
- Brown S D, Bouchenoire L, Bowyer D, Kervin J, Laundry D, Longfield M J, Mannix D, Paul D F, Stunault A, Thompson P, Cooper M J, Lucas C A, and Stirling W G 2001 The XMaS beamline at ESRF: instrumental developments and high resolution diffraction studies *Journal of Synchrotron Radiation* **8** 1172-1181

References

- Castro C R F, Barroso R C, de Oliveira L F, and Lopes R T 2005 Coherent scattering X-ray imaging at the Brazilian National Synchrotron Laboratory: Preliminary breast images *Nuclear Instruments & Methods in Physics Research Section A-Accelerators Spectrometers Detectors and Associated Equipment* **548** 116-122
- Chapman D, Thomlinson W, Johnston R E, Washburn D, Pisano E, Gmur N, Zhong Z, Menk R, Arfelli F, and Sayers D 1997 Diffraction enhanced x-ray imaging *Physics in Medicine and Biology* **42** 2015-2025
- Cheung K C, Fayz K, Laundry D, Lewis R, Dobson B, and Hall C 2003 First test pictures from X-ray diffraction enhanced imaging camera for high contrast medical imaging at SRS *Nuclear Instruments & Methods in Physics Research Section A-Accelerators Spectrometers Detectors and Associated Equipment* **513** 32-35
- Clarke R L and Vandyk G 1973 New Method for Measurement of Bone Mineral Content Using Both Transmitted and Scattered Beams of Gamma-Rays *Physics in Medicine and Biology* **18** 532-539
- Department of Health. 2003. NHS Breast Screening Programme Annual Review. Report
- Duke P R and Hanson J A 1984 Compton Scatter Densitometry with Polychromatic Sources *Medical Physics* **11** 624-632
- European Synchrotron Radiation Facility 2004 [online] Available at: <http://www.esrf.fr> [Accessed January 2004]
- Ellis R L 1999 Differentiation of benign versus malignant breast disease *Radiology* **210** 878-879
- Evans S H, Bradley D A, Dance D R, Bateman J E, and Jones C H 1991 Measurement of Small-Angle Photon Scattering for Some Breast Tissues and Tissue Substitute Materials *Physics in Medicine and Biology* **36** 7-18
- Evans 1955 *The atomic nucleus* (McGraw-Hill, New York)
- Farquharson M J and Geraki K 2004 The use of combined trace element XRF and EDXRD data as a histopathology tool using a multivariate analysis approach in characterizing breast tissue *X-Ray Spectrometry* **33** 240-245
- Farquharson M J, Luggar R D, and Speller R D 1997 Multivariate calibration for quantitative analysis of EDXRD spectra from a bone phantom *Applied Radiation and Isotopes* **48** 1075-1082
- Fentiman I 1990 *Detection and Treatment of Breast Cancer* (London: Martin Dunitz)

References

- Fernandez M, Keyrilainen J, Serimaa R, Torkkeli M, Karjalainen-Lindsberg M L, Leidenius M, von Smitten K, Tenhunen M, Fiedler S, Bravin A, Weiss T M, and Suortti P 2005 Human breast cancer in vitro: matching histo-pathology with small-angle x-ray scattering and diffraction enhanced x-ray imaging *Physics in Medicine and Biology* **50** 2991-3006
- Fernandez M, Keyrilainen J, Serimaa R, Torkkeli M, Karjalainen-Lindsberg M L, Tenhunen M, Thomlinson W, Urban V, and Suortti P 2002 Small-angle x-ray scattering studies of human breast tissue samples *Physics in Medicine and Biology* **47** 577-592
- Foster R S and Costanza M C 1984 Breast Self-Examination Practices and Breast-Cancer Survival *Cancer* **53** 999-1005
- Galkin B M, Feig S A, Patchefsky A S, Rue J W, Gamblin W J, Gomez D G, and Marchant L M 1977 Ultrastructure and Microanalysis of "Benign" and "Malignant" Breast Calcifications *Radiology* **124** 245-249
- Geraki K, Farquharson M J, and Bradley D A 2004 X-ray fluorescence and energy dispersive x-ray diffraction for the quantification of elemental concentrations in breast tissue *Physics in Medicine and Biology* **49** 99-110
- Geraki K 2003 Differentiating normal and diseased breast tissue using X-ray fluorescence and energy dispersive x-ray diffraction *PhD Thesis* City University, London
- German M J, Hammiche A, Ragavan N, Tobin M J, Cooper L J, Matanhelia S S, Hindley A C, Nicholson C M, Fullwood N J, Pollock H M, and Martin F L 2006 Infrared spectroscopy with multivariate analysis potentially facilitates the segregation of different types of prostate cell *Biophysical Journal* **90** 3783-3795
- Gould B 1997 *Pathophysiology for the Health Professions* (Pennsylvania: WB Saunders)
- Griffiths JA, Speller RD, Royle GJ, Horrocks JA, Olivo A, Pani S, Longo R, Dreossi SH, Spencer SH, Robbins MS, Clifford DP and Hanby AM 2004a X-Ray Diffraction CT of Excised Breast Tissue Sections: First Results from Ellettra *IEEE Nuclear Science Symposium and Medical Imaging Conference Proceedings, Portland, USA*
- Griffiths JA, Speller RD, Royle GJ, Horrocks JA, Olivo A, Pani S, Longo R, Spencer SH, Robbins MS, Clifford DP and Hanby AM 2004b Diffraction Enhanced Breast Imaging: assessment of realistic system requirements to improve the diagnostic capabilities of mammography *IEEE Nuclear Science Symposium and Medical Imaging Conference Proceedings, Portland, USA*

References

- Hubbell J, Viegale Wm J, Briggs E A, Brown R T, Cromer D T, and Howerton R J 1975 Atomic Form Factors, Incoherent Scattering Functions and Photon Scattering Cross Sections *Journal of Physical and Chemical Reference Data* **4** 471-616
- Huddleston A L and Sackler J P 1985 The Determination of Electron-Density by the Dual-Energy Compton Scatter Method *Medical Physics* **12** 13-19
- Hirayama H, 2000 Lecture notes on Photon Interactions and Cross Sections *Internal . KEK, High Energy Accelerator Research Organization*
- ICRU. Photon, electron, proton and neutron interaction data for body tissues. 49. 1992. Report
- Johns P C and Yaffe M J 1983 Coherent Scatter in Diagnostic-Radiology *Medical Physics* **10** 40-50
- Kidane G, Speller R D, Royle G J, and Hanby A M 1999 X-ray scatter signatures for normal and neoplastic breast tissues *Physics in Medicine and Biology* **44** 1791-1802
- Kiss M Z, Sayers D E, Zhong Z, Parham C, and Pisano E D 2004 Improved image contrast of calcifications in breast tissue specimens using diffraction enhanced imaging *Physics in Medicine and Biology* **49** 3427-3439
- Kosanetzky J, Knoerr B, Harding G, and Neitzel U 1987 X-Ray-Diffraction Measurements of Some Plastic Materials and Body-Tissues *Medical Physics* **14** 526-532
- Kotre C J and Birch I P 1999 Phase contrast enhancement of x-ray mammography: a design study *Physics in Medicine and Biology* **44** 2853-2866
- Lakhani S 2003 The diagnosis and management of pre-invasive breast disease – current challenges, future hopes. *Breast cancer research* **5** 248-249
- Lewis R A, Hall C J, Hufton A P, Arfelli F, Evans A J, and Evans S H 2001 X-ray diffraction-enhanced imaging (DEI) *Radiology* **221** 165
- Lewis R A, Rogers K D, Hall C J, Towns-Andrews E, Slawson S, Evans A, Pinder S E, Ellis I O, Boggis C R M, Hufton A P, and Dance D R 2000 Breast cancer diagnosis using scattered X-rays *Journal of Synchrotron Radiation* **7** 348-352

References

- Maruo K, Oota T, Tsurugi M, Nakagawa T, Arimoto H, Tamura M, Ozaki Y, and Yamada Y 2006 New methodology to obtain a calibration model for non-invasive near-infrared blood glucose monitoring *Applied Spectroscopy* **60** 441-449
- Narten A H and Levy H A 1971 Liquid Water: Molecular Correlation Functions from X-Ray Diffraction *Journal of Chemical Physics* **55** 2263-2269
- Olkkonen H and Karjalainen P 1975 A Tm-170 gamma scattering technique for the determination of absolute bone density *British Journal of Radiology* **48** 594-597
- Peplow D E and Verghese K 1998 Measured molecular coherent scattering form factors of animal tissues, plastics and human breast tissue *Physics in Medicine and Biology* **43** 2431-2452
- Poletti M E, Goncalves O D, and Mazzaro I 2002 X-ray scattering from human breast tissues and breast- equivalent materials *Physics in Medicine and Biology* **47** 47-63
- Robinson I A, Mckee G, Nicholson A, Darcy J, Jackson P A, Cook M G, and Kissin M W 1994 Prognostic Value of Cytological Grading of Fine-Needle Aspirates from Breast Carcinomas *Lancet* **343** 947-949
- Round A R, Wilkinson S J, Hall C J, Rogers K D, Glatter O, Wess T, and Ellis I O 2005 A preliminary study of breast cancer diagnosis using laboratory based small angle x-ray scattering *Physics in Medicine and Biology* **50** 4159-4168
- Speller R D, Royle G J, and Horrocks J A 1989 Instrumentation and Techniques in Bone-Density Measurement *Journal of Physics E-Scientific Instruments* **22** 202-214
- Stomper P C, Dsouza D J, DiNitto P A, and Arredondo M A 1996 Analysis of parenchymal density on mammograms in 1353 women 25-79 years old *American Journal of Roentgenology* **167** 1261-1265
- Tartari A, Casnati E, Bonifazzi C, and Baraldi C 1997 Molecular differential cross sections for x-ray coherent scattering in fat and polymethyl methacrylate *Physics in Medicine and Biology* **42** 2551-2560
- Trott P 1996 *Breast cytopathology: A diagnostic atlas* (London: Chapman Hall Medical)
- Vaupel P, Kallinowski F, and Okunieff P 1989 Blood-Flow, Oxygen and Nutrient Supply, and Metabolic Microenvironment of Human-Tumors - A Review *Cancer Research* **49** 6449-6465

References

- Veigele W.J., Tracy P.T., and Henry E.M., (1966) Coherent and incoherent Atomic form factors *Am.J. Phys.* **34**, 1116.
- Waller I; Hartree DR 1929 On the intensity of total scattering of X-rays *Proceeding of the Royal Society A-* **124 (793)**: 119-142
- Warberg O 1930 *The metabolism of tumours* (London: Constable)
- Webber C E and Coates G 1982 A Clinical-System for the In vivo Measurement of Lung Density *Medical Physics* **9** 473-477
- Webber C E and Kennet T J 1976 Bone Density Measured by Photon Scattering. I. A System for Clinical Use *Physics in Medicine and Biology* **21** 760-769
- Weber S, Storm F K, Stitt J, and Mahvi D M 1997 The role of frozen section analysis of margins during breast conservation surgery *Cancer Journal from Scientific American* **3** 273-277
- Wilkins S W, Gureyev T E, Gao D, Pogany A, and Stevenson A W 1996 Phase-contrast imaging using polychromatic hard X-rays *Nature* **384** 335-338
- Wilkinson S J, Rogers K D, Hall C J, Lewis R A, Round A, Pinder S E, Boggis C, and Hufton A 2004 Small angle diffraction imaging for disease diagnosis *Nuclear Instruments & Methods in Physics Research Section A-Accelerators Spectrometers Detectors and Associated Equipment* **548** 135-139
- Zakhour H and Wells C 1999 *Diagnostic cytopathology of the breast* (London: Churchill Livingstone)
- Zonderland H M, Michiels J J, and Tenkate F J W 1991 Mammographic and Sonographic Demonstration of Extramedullary Hematopoiesis of the Breast - Case-Report *Clinical Radiology* **44** 64-65